FORMATION OF SOLAR PROMINENCES AND ERUPTION OF SOLAR MAGNETIC ARCADE SYSTEMS

A

THESIS

Presented to the Faculty

of the University of Alaska Fairbanks

in Partial Fulfillment of the Requirements

for the Degree of

DOCTOR OF PHILOSOPHY

By

Gwang-Son Choe, B.S., M.S.

Fairbanks, Alaska

August 1995

FORMATION OF SOLAR PROMINENCES AND ERUPTION OF SOLAR MAGNETIC ARCADE SYSTEMS

By

Gwang-Son Choe

RECOMMENDED:

Syun-Ichi Akasofu

Juan G. Roederer

Daniel W. Swift

Brenton J. Watkins

Lou-Chuang Lee, Chairman, Advisory Committee

John L. Morack, Head, Physics Department

APPROVED:

Paul B. Reichardt, Dean, College of Natural Sciences

Joseph R. Kan, Dean of the Graduate School

August 7, 1995

Date

ABSTRACT

Formation and eruption of solar prominences, coronal mass ejections (CMEs) and solar flares are the most magnificent phenomena among solar activities. Observations show that there is an interrelationship among these events and that their manifestation is conditioned by certain common photospheric signatures. One of them is the increase in magnetic shear. In this thesis, the evolution of the solar atmosphere is studied by numerical simulations with photospheric motions as boundary conditions.

Firstly, mechanisms of prominence formation are investigated. It is found that prominences can be formed by the development of a thermal instability (1) in a rapidly expanding magnetic arcade, (2) in a magnetic island created by magnetic reconnection or (3) in the current sheet between two bipolar arcades.

Secondly, the quasi-static evolution of a magnetic arcade subject to footpoint shearing is studied under the ideal MHD condition. Three distinct evolutionary phases are found, in the last of which a current layer develops and grows indefinitely with the increasing shear. Force-free field solutions are also constructed and compared with dynamic solutions.

Finally, resistive evolutions of magnetic arcades are investigated imposing resistivity on the pre-sheared magnetic fields. It is found that there is a critical amount of shear, over which magnetic reconnection can take place to create a magnetic island. The effects of different values and spatial patterns of resistivity are studied. With a localized resistivity, most of principal features in solar eruptive processes are reproduced. A comparative study is made between the numerical results and observations.

TABLE OF CONTENTS

LIST OF FIGURES

LIST OF TABLES

ACKNOWLEDGMENTS

It is a real pleasure for me to recall and extend my sincere thanks to those who rendered me help and care so that I have finally completed this thesis.

First of all, I am greatly indebted to Professor Lou-Chuang Lee, my advisor and mentor. He has not only inspired me with his own way of physical thinking, but also allowed me so much freedom to find my own direction and pursue it to its completion. He often placed on me more trust than I deserved, yet now I cannot but confess that it was a great encouragement to me. I extend my deepest appreciation to him.

I wish to express my thanks to Professor J. R. Kan for admitting me to UAF and introducing me into the solar flare problem. My gratitude should go to Professor Syun-Ichi Akasofu, who has continuously showed interest in the progress of my study and encouraged me. The kind and deep attention to my work paid by Professor Daniel Swift is also greatly appreciated. Professor Juan Roederer carefully read the draft and helped me to improve it, for which I pay appreciation to him. Professor Brenton Watkins rendered me help throughout my graduate study and cleared whatever problems I was confronted with, for which I am deeply obliged to him. My thanks are extended to Professor Jürgen Kienle for kindly correcting the manuscript. I am also grateful to the former members of my advisory committee, Dr. Davis Sentman and Dr. Joseph Hawkins for the helpful guidance.

As a lone solar researcher at the Geophysical Institute, I was fortunate to have an opportunity to visit the High Altitude Observatory/NCAR. In particular, I am grateful to Dr. Boon Chye Low for his warm hospitality, friendly guidance and enlightening conversations. I also wish to express my sincere thanks to Dr. Antonius Otto at GI/UAF for fruitful discussions which inspired me with insights into diverse problems in MHD. Dr. Yu-Qing Lou at the University of

Chicago also deserves my appreciation, for I acquired much knowledge of solar physics from enjoyable conversations with him.

My gratitude should be deservedly extended to Professor Hong Sik Yun at the Seoul National University, who taught me astrophysics and as a solar physicist himself has given me constant encouragement. In this place, I also confess my obligation to Professor Willy Deinzer and Professor Manfred Siebert at the Universität Göttingen, from whom I first learned magnetohydrodynamics.

I must take this opportunity to thank all of my friends and colleagues at the Geophysical Institute for lending me helping hands whenever I needed them. Among them, special thanks are due to Dr. Fei Cao, Dr. Dave Covey and Mr. Don Rice. Other names are too numerous to list them all, but my gratitude will rest upon them.

Finally, I give thanks from the bottom of my heart to my wife Jinhee for being with me anytime anywhere.

The work done in this thesis was supported by DOE grant DE-FG06-91ER 13530 and NASA SPTP grant NAG5-1504 to the University of Alaska. Supercomputing resources were provided by the Arctic Region Supercomputing Center and the San Diego Supercomputer Center.

CHAPTER 1

Introduction

The solar atmosphere consists of three layers: the photosphere, the chromosphere and the corona. The photosphere is the region where most of the solar radiation is emitted. Its thickness is about 500 km and the temperature decreases upwards from 6000 K at the bottom to 4000 K at the top (e.g., Zirin, 1988; Priest, 1982). The particles are mainly neutrals there and the number density is about $10^{17}\,\mathrm{cm}^{-3}$. The chromosphere is more transparent and extends to about 2000 km in height. The temperature increases slowly from 4000 K at the bottom to several tens of thousand K about 500 km below the coronal base and then rises rapidly to the coronal temperature of 2×10^6 K. This layer between the chromosphere and the corona is called the transition region. The corona is expanding outwards to the interstellar space in the form of solar wind. The temperature starts to decreases in the outer corona and becomes about 10^5 K at 1 AU. The ionization rate increases from the bottom of the chromosphere upwards and most hydrogen atoms are ionized in the upper chromosphere. The particle number density decreases to $10^9\,\mathrm{cm}^{-3}$ in the transition region and to $5 \times 10^8\,\mathrm{cm}^{-3}$ in the corona. The solar atmosphere is permeated with magnetic fields, which are believed to be generated below the photosphere by a dynamo process and emerge above the solar surface by magnetic buoyancy (e.g., Parker, 1979). In the photosphere, magnetic fields manifest themselves as small magnetic elements as if they were islands in the ocean. These small scale elements are often organized into large scale patterns such as sunspots, plages, network fields and so forth. In these concentrated magnetic fields, the field strength is usually over 1 kG. Outside these regions, the average field strength is of the order of 1 G. In the photosphere, the plasma β, the ratio of plasma pressure to magnetic pressure, is usually greater than unity except for the inside of sunspots or network fields, and the

motion and shaping of magnetic fields are governed by plasma motions. Going up to a higher altitude, magnetic fields tend to spread out and permeate the space somewhat more uniformly than in the photosphere. On the other hand, the plasma pressure drops rapidly with increasing altitude due to a small scale height ($\sim 300\,\mathrm{km}$ at the photosphere). Since the exponential drop of pressure is faster than the lateral dispersion of magnetic fields, the plasma β is already near or below unity in the chromosphere. In the upper solar atmosphere, the magnetic field governs the plasma motion. However, the motive of coronal field motions comes from field footpoints which are moved by photospheric or subphotospheric plasma flows. It is thus natural to look into the photosphere for a cause of a coronal event. Since the thickness of the photosphere and chromosphere is very small compared to the coronal length scale, it is justifiable to treat any motions in the lower atmosphere as boundary conditions and establish a model containing the corona only. Formation of solar prominences and solar eruptive processes such as flares and coronal mass ejections are among the most fascinating phenomena in the Sun. It is all the more intriguing that these apparently different phenomena have similar precursors observed in the photosphere. In this thesis, we have investigated the prominence formation and solar eruptive processes adopting the aforementioned modelling of the solar corona.

In this chapter, a brief review is given on observations and theories regarding these phenomena. As there already exist a number of excellent review papers (Hirayama, 1985; Martin, 1990, Priest, 1981; 1989; Forbes, 1990b; Forbes, 1992; Démoulin, 1991; Hundhausen, 1988; 1995; Browning, 1988; Hood, 1991) and monographs (Tandberg-Hanssen, 1974; Priest, 1982; Zirin, 1988) in this field, it may be taken as a matter of course to consult these literatures. Thus we do not claim originality of the contents of this introductory chapter. In Section 1.1, the observation of solar prominences is reviewed along with the support models. Regarding solar eruptive processes, observations are briefly summarized in Section 1.2 and an overview on the theories is given in Section 1.3. In Section 1.4, the organization of this thesis is outlined.

1.1 Prominence Observations and Support Models

1.1.1 Definition and Generals

Solar Prominences are defined as any cloud of material visible in H_α above the solar surface (Zirin, 1988). Since H_α is excited when the hydrogen gas is in the temperature range of 6000 to 11000 K, the prominence material is about 100 times cooler than the surrounding coronal plasma ($\sim 10^6$ K), and for pressure balance, the density of prominence material (10^{10}–10^{11} electrons per cm^3) is about 100 times higher than that of the coronal plasma.

The classification of prominences is quite diverse. Mostly prominences are classified either into quiet region prominences and active region prominences according to the locations (Hirayama, 1985) or into quiescent prominences and active prominences according to their lifetime (Zirin, 1988). The classification by Zirin (1988) is listed in Table 1.1.

TABLE 1.1 Classification of Prominences

Class 1.	Quiescent prominences
	a) prominences in quiet regions (QRF)
	b) prominences in or near active regions (ARF)
	c) ascending prominences (they were once long-lived)
Class 2.	Active prominences
	a) loop prominences
	b) coronal rains
	c) surges: collimated ejected material
	d) sprays: uncollimated ejecta

The term "prominence" is often referred to prominences in Class 1 and only these prominences are called "filaments." Also the term "quiescent prominence" is often used as a synonym to "quiet region filament." Quiet region prominences (QRF) persist normally for several solar rotations and have a length of 60,000 to 600,000 km, a height of 10,000 to 100,000 km and a thickness of 4,000 to 15,000 km (Priest, 1989). An active region prominence (ARF) sometimes develops into a quiet region prominence (QRF) as the active region smears out and it is of a smaller size than a QRF. The temperature of ARFs is much the same as that of QRFs, but their density is larger and their height is lower. An ARF eruption is usually accompanied by a sizable flare, while a QRF eruption may produce a big coronal mass ejection (CME).

Quiescent prominences are observed to be composed of small scale fine structures, whose time scale is quite short (4–5 minutes) compared to the long lifetime of the global structure of quiescent prominences. The length of these thread-like fine structures is about 5,000 km and the width is 200 to 400 km (Bruzek, 1981).

According to Hirayama (1985), the range of temperature in quiescent prominences is 5000–8000 K and the average value is about 7000 K. The electron number density and the ionization degree in the prominences are yielded quite differently depending on the methods used. While the measured electron densities fall in the range of 10^9–$10^{12}\,\mathrm{cm}^{-3}$, the deduced ionization degree ($n_{\mathrm{HII}}/n_{\mathrm{HI}}$) varies from 0.05 to 3 according to the authors (Schmieder, 1989). These disagreements in the electron density and the ionization degree yield widely different (about three orders of magnitude) values of plasma β and have serious effects on theories of prominence formation.

1.1.2 Magnetic Fields

The magnetic field in a prominence is measured by the Zeeman effect or the Hanle effect. Hirayama (1985) suggested an average magnetic field strength of 8 G for QRFs. For ARFs the preferred magnetic field strength is 20 G. The direction of magnetic field penetrating the prominence plane determines whether it belongs to normal polarity (NP) prominences or inverse polarity prominences (IP). In NP prominences, the magnetic field component perpendicular to the prominence axis is parallel to the possible potential field above the magnetic neutral line and in IP prominences, it is antiparallel. Observations by Leroy *et al.* (1984) show that three quarters of the cases (tall ones with weak fields) are of IP type, while one quarter (low-lying ones with stronger fields) are of NP type. But these figures should not be taken as real proportions because coronagraph observations miss prominences lower than 10000 km. It should also be noted that low prominences are much more numerous than high prominences.

There is a trend of increasing magnetic field with altitude. Leroy *et al.* (1983) derived average gradient of 0.5×10^{-4} G km^{-1}. However, Athay *et al.* (1983) did not find any increase from the detailed inspection of HAO-Sac Peak data.

The magnetic field vector in quiescent prominences is very close to the horizontal plane. According to Athay *et al.* (1983) the average field vector departs by less than 10° from the horizontal. The "V"-shaped dip structure, which is essential for the support of the prominence, has not yet been resolved.

The magnetic field in prominences makes small angle with the prominence axis. Kim *et al.* (1988) derived most probable angle of 25° between the field vector and the prominence axis.

1.1.3 Velocity Fields

The non-thermal random velocity, often called turbulent velocity, is measured from the widths of weak metallic lines and shows a tendency of increasing towards the periphery of the prominence. In the inner part of prominences this velocity is 3–8 $\mathrm{km\,s^{-1}}$ whereas in the outer part it takes values of 10–20 $\mathrm{km\,s^{-1}}$ (Engvold, 1978).

Systematic steady flows are also observed in and near prominences. The sign of the vertical motion in prominences was in the past a controversial subject. Downflows were observed at the limb (Engvold, 1976) whereas upflows were detected in prominences on the disk (Malherbe *et al.*, 1983). The existence of a mean upflow is now generally accepted with an amplitude of 0.5 $\mathrm{km\,s^{-1}}$ in H_α and of 5 $\mathrm{km\,s^{-1}}$ in CIV. The reported downflows at the limb seem to be not a bulk motion but a fluctuation in the ionization degree of material. Around prominences, the same ascending behavior is seen in the transition region with a velocity of 1.6 $\mathrm{km\,s^{-1}}$ (Hirayama, 1985). On the other hand, strong downflows ($< 10\,\mathrm{km\,s^{-1}}$) are observed at the ends or footpoints of prominences. Up and down motions of $\pm 6\,\mathrm{km\,s^{-1}}$ are also observed near footpoints.

Analysis of mass motions from center to limb observations shows the existence of horizontal flows in and around the prominence. The direction of the velocity is parallel to the magnetic field line and the measured values are from 5 $\mathrm{km\,s^{-1}}$ to 20 $\mathrm{km\,s^{-1}}$ (Malherbe *et al.*, 1983; Athay *et al.*, 1985).

A new type of interesting motion was reported by Ligget and Zirin (1984); material seems to go up in a semi-circular trajectory and come down again along a semi-circular trajectory with velocities of 15–75 $\mathrm{km\,s^{-1}}$.

All these flow patterns suggest a circulation of matter in and around the prominences and the modelling of the prominence should accommodate these dynamic interactions between prominences and their environment.

1.1.4 Prominence Environment

Figure 1.1 shows a schematic picture of the structure in the prominence environment. The prominence appears as a thin, vertical slab of plasma suspended in the corona and has one or more arch-like structures that rise out of the chromosphere and then descend back down. Each arch-like structure constitutes a section, whose chromospheric terminations are referred to as legs.

Quiescent prominences are usually located at the base of coronal helmet streamers. The central part of the helmet surrounding the prominence is less bright than the rest of the structure. This darker and less dense volume is called a coronal cavity. The helmet streamers are often associated with a prominence but not always. The streamers encapsule at least two arch systems. The streamers are detected out to distances from the Sun's limb of more than one solar radius. A typical diameter for a helmet is 3×10^5 km.

Coronal cavities are dark long strips along neutral lines where only a fractional length of 0.2–0.5 contains prominences. An average coronal cavity has a length of $2 \times 10^5 - 3 \times 10^6$ km, a width of $\sim 6 \times 10^4$ km and a height of $\gtrsim 5 \times 10^4$ km. The cavities are darker than surroundings due to a lower electron density ($1.5–3 \times 10^8$ cm^{-3}) (Serio *et al.*, 1978). The temperature in the coronal cavity is found to be almost the same as the surrounding corona (Bessey and Liebenberg, 1984). The structure of the cavity is roughly unchanged, but the brightness is enhanced when the prominence has temporarily disappeared. It has long been speculated that the prominence is formed by condensation of material in the cavity. Saito and Tandberg-Hanssen (1973), however,

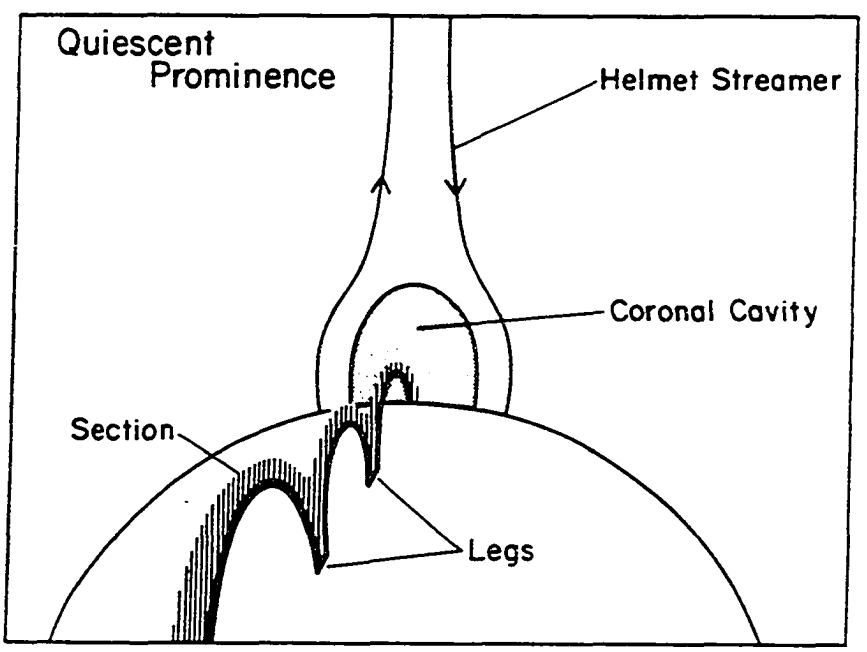

Figure 1.1 Principal features of a typical prominence-corona helmet configuration. (Forbes, 1990b).

found that the formation of a typical quiescent prominence requires much more material than is available in the cavity before depletion. But considering that the total mass of a prominence is still uncertain and the prominence material is concentrated in small scale fine structures, the origin of prominence material is still controversial.

1.1.5 Observed Conditions for Prominence Formation

Martin (1990) discussed conditions observable in the optical wavelengths, which are considered to be essential clues to the formation of the magnetic field structure of prominences. Here we list them briefly.

(1) Prominences are always observed above the polarity inversion lines.

(2) There exists a coronal arcade lying over the prominence.

(3) Transverse magnetic fields observed in the neighborhood of the polarity inversion line are almost parallel to this line.

(4) Chromospheric fibrils are aligned parallel to the polarity inversion line.

(5) There are flows of small patches of opposite polarity magnetic flux towards the polarity inversion line.

(6) Encountering patches of opposite polarity magnetic flux disappear in the polarity inversion line as if they cancel each other.

In short, these conditions indicate two facts. First, the magnetic fields are highly sheared near the polarity inversion line. Second, there are possibly emerging or submerging magnetic fluxes at the polarity inversion line. This flux transport, if any, is probably caused by magnetic reconnection at, above or below the polarity inversion line.

1.1.6 Support Models

A prototype model of NP prominences is constructed by Kippenhahn and Schlüter (1957). This model assumes the configuration shown in Figure 1.2a, but describes the field and plasma only in the neighborhood of the prominence. In this model, the magnetic tension provides an upward force to balance the gravity and support the prominence, whereas the magnetic pressure increases with the horizontal distance from the prominence and provides a transverse force to compress the plasma and balance the plasma pressure gradient. More generalized Kippenhahn-Schlüter-type configurations can be found in Low (1981).

Following the discovery that most quiescent prominences have inverse polarity, Kuperus and Raadu (1974) proposed the inverse polarity configuration shown in Figure 1.2b. In the original model, the magnetic field generated by the current flowing through the prominence does not penetrate into the photosphere and the induced current on the solar surface pushes up the current filament. The surrounding line-tied field as well as the gravity keeps the prominence from rising.

For more realistic static models of prominences, readers are referred to the review of static support models by Anzer (1989). As far as a single bipolar arcade is concerned, the Kippenhahn-Schlüter type prominence is of normal polarity and the Kuperus-Raadu type prominence is of inverse polarity. In more complex field geometry, this equating generally does not hold as will be seen in Chapter 2.

1.2 Observations of Solar Flares and Coronal Mass Ejections

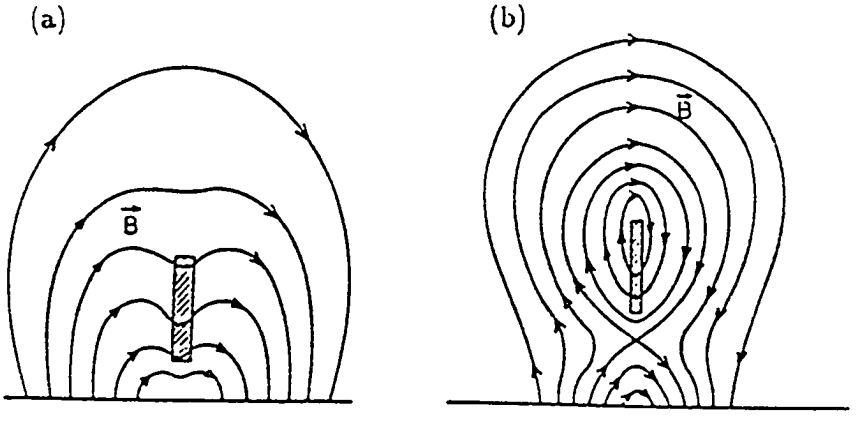

Figure 1.2 Sketch of the possible field topologies in prominences (Anzer, 1989). (a) Kippenhahn-Schlüter type. (b) Kuperus-Raadu type.

1.2.1 Solar Flares

Historically, brilliant flashes of light (H_α or white light) in the solar atmosphere are named "solar flares." More generally, solar flares are intense, abrupt release of energy occurring usually in the vicinity of an active region. A large flare can release over 10^{32} erg of energy in an hour or so. Flares spring up in active regions where the magnetic field is stressed by flux emergence or sunspot motion. There is a rapid increase in intensity in different wavelengths of emission followed by a slow decrease. Over the initial stages the intensities increase on a timescale of seconds to minutes whereas the decay phase may occur on a slower timescale of hours to a day. Figure 1.3 shows various phases in a typical flare.

In the preflare phase, about 10 minutes before the flare onset, enhanced thermal emissions from the coronal plasma are detected mostly in the soft X-ray ($h\nu < 10\,\mathrm{keV}$ or $0.1\,\mathrm{nm} < \lambda < 2\,\mathrm{nm}$). During the flash phase, which lasts typically a few minutes, the intensity and area of the emission rapidly increase in value. Then, in the main phase, the intensity slowly declines over about an hour or sometimes as much as a day. Large flares also exhibit an impulsive phase, lasting 10–100 seconds, during which hard X-ray ($\lambda < 0.1\,\mathrm{nm}$) and microwave bursts are observed. These bursts are caused by highly accelerated electrons.

Flares can be classified in many different ways, but here we present a simple classification into "two-ribbon flares" and "simple-loop flares." All major flare events are two-ribbon flares, which are on a much larger scale than simple loop flares and usually take place near a solar prominence. They are characterized by two bright H_α ribbons moving apart with hot X-ray plasma frequently seen joining the ribbons. Most mediocre flares and subflares are simple-loop flares, in which a single magnetic loop or flux tube brightens in X-rays and remains unchanged in shape and position throughout the event. Typical large flare features include (i) high temperatures ($> 10^7$ K), (ii) large amount of energy released (10^{32} erg), (iii) two-ribbons and post-flare loops,

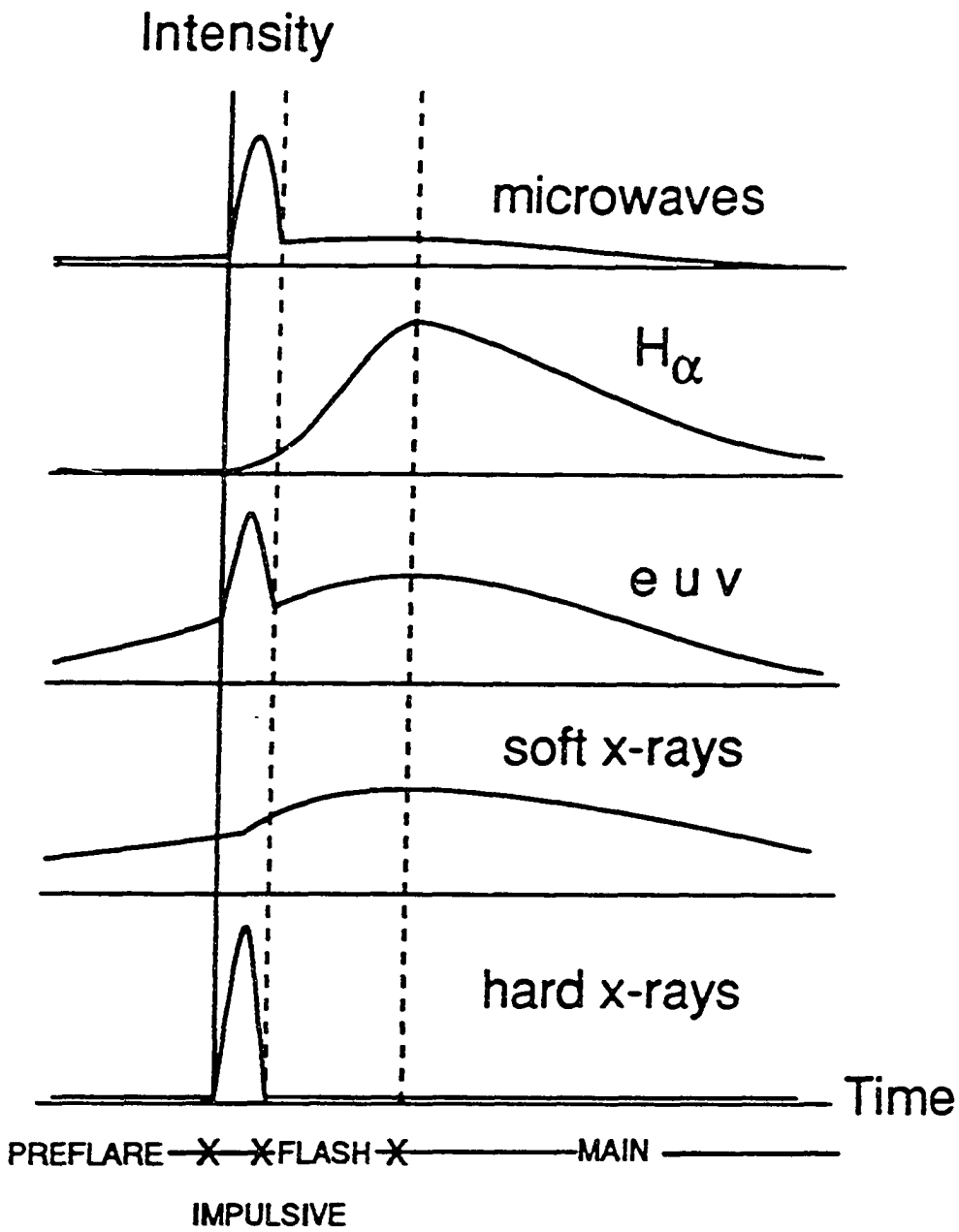

Figure 1.3 A schematic profile of the flare intensity in several wavelengths as function of time during a solar flare (Priest, 1982).

(iv) prominence eruption and CME starting before the flare onset, and (v) fast particles indicating acceleration due to an electric field.

1.2.2 Coronal Mass Ejections (CMEs)

Coronal mass ejections are seen as bright features that move outward through the solar corona at speeds from 10 to $\sim 2000\,\mathrm{km\,s^{-1}}$ (Hundhausen, 1995). A typical large CME expels more than 10^{16} g of plasma at a speed of $\sim 1000\,\mathrm{km\,s^{-1}}$ against the solar gravitational field and the energy required in this process is $\gtrsim 10^{32}$ erg.

Now we briefly describe the typical sequence of CMEs following SMM observations by Hundhausen (1995). Readers are also referred to Figure 1.4. CMEs involve the eruption of coronal plasma from a region where magnetic fields are initially closed, namely, within a helmet. A prominence is usually located above the polarity inversion line within the helmet. For several days before the actual mass ejection, the helmet streamer slowly rises and swells outward. The prominence is seen to begin erupting a couple of hours before the cavity is seen to move out in the outer corona. This time gap is due to the different observation windows for two events. The fast-moving cavity distorts the helmet into a bright frontal loop. The brightened prominence moves outward within the cavity, more slowly than the cavity top. As it moves out, the prominence takes a more complex shape like a broken frayed rope. After the loop and the prominence have moved out of the coronagraph field, the corona looks like rays or a fan. This indicates an almost open magnetic field configuration within the observation field.

In early days, it was thought that prominence eruptions drive coronal mass ejections (e.g., Hu, 1983a; 1983b). However, there are two empirical arguments against this concept. First, many CMEs are observed without prominence eruption. Second, the prominence top always moves slower than the cavity top or the frontal loop. There was also a view that the explosive

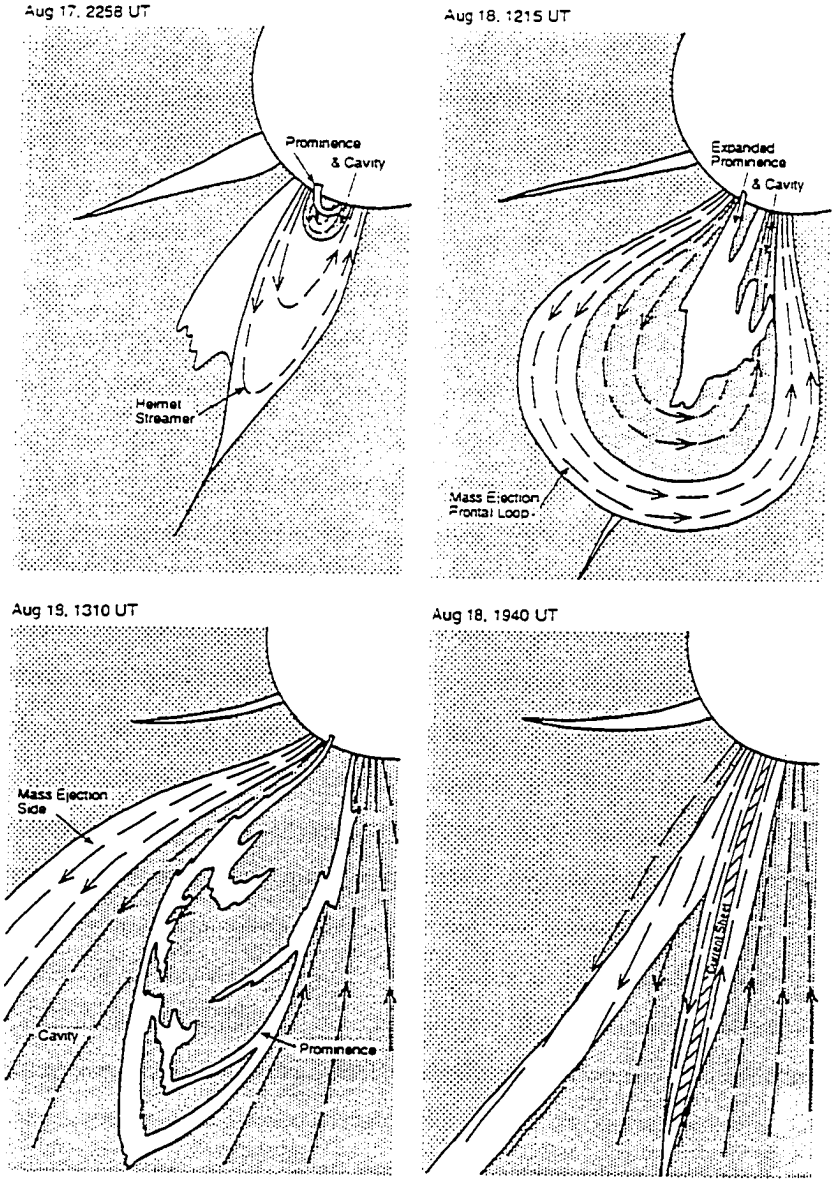

Figure 1.4 A sketch of the sequence of a typical CME (Hundhausen, 1995). Plausible field directions are shown by arrows.

heating of the lower corona by solar flares drive mass ejections (e.g., Dryer, 1982). However, soft X-ray flares always lag behind the mass ejections. Even hard X-ray flares are timed to occur 10 to 20 minutes before the CME launch time estimated with the assumption of constant acceleration. However, if the CME acceleration is done almost instantaneous, the CME launch time coincides with the hard X-ray flare onset. In any case, CMEs are unlikely to be driven by solar flares.

1.3 Overview of Theories on Solar Eruptive Processes

1.3.1 Magnetic Reconnection in General

It was Giovanelli (1947) who first attempted to explain solar flares in terms of energy release by magnetic reconnection. Giovanelli's idea was further developed and mathematical formulations were provided by Sweet (1958), Parker (1963), Petschek (1964) and other authors. The Sweet-Parker model considers the neighborhood of the diffusion region, and the reconnection rate, which is the upstream Alfvén Mach number, is scaled as $M_i \sim R_{mi}^{1/2}$, where the subscript i means the closeness to the diffusion region and R_{mi} is the magnetic Reynolds number in the scale of the diffusion region. In the Petschek model, on the other hand, the diffusion region is considered to have a negligible size and attention is paid to the global field and flow patterns. Here, conversion of magnetic energy into kinetic energy is made by two pairs of slow shocks attached to the diffusion region. The Petschek reconnection rate is proportional to $1/(\log R_{me})$ where R_{me} is the Magnetic Reynolds number in global scale. The Petschek rate can thus be kept high even for a large R_{me}, which provides theoretical grounds for a sudden energy release by reconnection in space plasmas where R_{me} is generally huge ($\sim 10^{12}$). In this section, our main interest does not lie in the reconnection processes, but in the global dynamics which causes a

solar eruptive process whether it involves magnetic reconnection or not. For further physics of magnetic reconnection, readers are referred to Vasyliunas (1975) and Priest and Forbes (1987; 1992b).

1.3.2 Simple-Loop Flares

In compact simple-loop flares, the loop structures are not totally destroyed in the course of the flaring process. There are some theoretical models, which can be applied to this type of flares. Historically, Sweet (1958) envisioned the merging of two bipolar regions with the formation of a current sheet in between. Gold and Hoyle (1960) modeled the merging of two magnetic flux tubes, which have parallel toroidal currents. This type of merging is recently observed by Yohkoh SXT. Among models of simple-loop flares, the emerging-flux model has been most highlighted. This model is based on observations that there is a strong correlation between solar flares and the emergence of new flux into the chromosphere (e.g., Rust, 1972). An analytical model was subsequently developed by Heyvaerts *et al.* (1977). In this model, a new flux tube rises and collides with existing fields, creating a current sheet. During the impulsive phase, the reconnection is a driven process, but relaxes to a steady state during the main phase. Recently, solar coronal X-ray jets are discovered by Shibata *et al.* (1992) using the Yohkoh SXT data. A series of numerical simulations by Yokoyama (1995) and Yokoyama and Shibata (1994) explain X-ray jets as reconnection outflows in the emerging flux picture. In all the above models, free energy has been stored in magnetic field configurations containing current sheets and is suddenly released by magnetic reconnection acting like a valve. There are another type of models, in which plasma motions in or below the photosphere generate currents like an MHD generator and the conjugate region connected by field lines acts as a load, where flare phenomena are manifested (e.g., Kan *et al.*, 1983). In these "dynamo theories" of

solar flares, not a sheared state but a sudden shearing motion can create flares. There are a few observational facts supporting this scenario. Hagyard *et al.* (1986) reported a case in an active region, where major flaring took place while the compression and twisting of the magnetic fields were occurring, rather than after the maximum deformation had been reached. Wang *et al.* (1994) also found that soft X-ray intensity peaks in some X-class flares are synchronously timed with a sudden increase in magnetic shear. Although the "store-release paradigm" has prevailed in flare theories to date, the "dynamo-load paradigm" can be prospective depending on further accumulation of observations.

1.3.3 Large Scale Eruption Models

A large scale solar eruptive process usually involve a CME, prominence eruption and a flare. As seen in the previous section, such a process starts with distension of the overlying arcade (the "helmet"), which leads to current layer formation, and ends with flare phenomena. This picture was first proposed by Kopp and Pneuman (1976) without providing underlying mechanisms. The studies on large scale solar eruptions can be classified into three categories, which we will briefly discuss below.

Arcade Reconnection Models

In this group of models, the ideal MHD evolution leads to distension of the arcade and formation of a current layer and then magnetic reconnection causes main eruption and complete ejection of a part of the flux system, i.e., a plasmoid. It was Mikić *et al.* (1988) who first demonstrated magnetic reconnection and plasmoid ejection in a multiple arcade system, which has been continuously sheared. Biskamp and Welter (1989), however, reported that there is no magnetic reconnection in a single isolated arcade. Imposing converging motions as well as shearing motions, Inhester *et al.* (1992) found that magnetic reconnection can take place in a

single arcade. In a spherical geometry, Mikić and Linker (1994) showed that a major eruption can take place by magnetic reconnection in a single arcade sheared slowly. In all these models, magnetic free energy tapped by reconnection provides kinetic energy required for plasmoid ejection.

Field Opening Models

In this group of models, the magnetic field opens up at least partially in ideal MHD condition to create a current sheet of infinite length, which is a potential location of magnetic reconnection. All the models in this category deal with force-free magnetic fields. Once, there was an idea that the open field energy can be lower than the energy of a closed sheared field. The force-free field constructed numerically by Barnes and Sturrock (1972) was asserted to be the case, but it later turned out to be a numerical artifact due to too small a size of their computational domain (Yang *et al.*, 1986). Aly (1984) conjectured that the open field energy be the upper bound of the energy of force-free fields and argued that the above scenario is energetically impossible. Later, physical proofs were provided to this conjecture by Aly (1991) and Sturrock (1991). On the other hand, Low (1986) proposed that a partially open configuration may be achieved in a 2-D spherical geometry or in 3-D. Wolfson and Low (1992) showed that partially sheared force-free fields can have higher energy than the partially open field. Although this study implicitly demonstrated the possibility of partial opening of magnetic fields, it is doubtful whether closed force-free states having more energy than the partially open field can be accessed in free space. Direct demonstrations of partial opening of force-free fields are provided by Mikić and Linker (1994) using a zero-beta code and by Roumeliotis *et al.* (1994) using a magnetofrictional method. In a finite β plasma, however, no field opening has been found (Mikić and Linker, 1994). Furthermore, the field opening process is not an energy-releasing process. Therefore, these models cannot be naively applied to the solar eruptive processes.

Flux Rope Catastrophe Models

The basic idea of these models was born when Kuperus and Raadu (1974) proposed their prominence support model. A flux rope detached from the photosphere induces a surface current of the sign opposite to its own current on the photosphere, which is considered as a rigid conductor. The two currents repel each other and the flux rope would be pushed to infinity if there were no gravity or surrounding line-tied field. Suppose that the flux rope is in equilibrium within a line-tied field and if the current of the flux rope is somehow increased or the flux of the ambient field is decreased, the flux rope may suddenly lose equilibrium and rise. The ideal MHD condition usually prevents the flux rope from rising indefinitely and the flux rope will find a new equilibrium at a higher altitude with a current sheet extending from its bottom to the photosphere. This model was developed by Van Tend and Kuperus (1978) with a line current and further elaborated by Forbes (1990a) and Forbes and Isenberg (1991) including the finite size of the current-flowing cross-section. The catastrophe can only explain the sudden distension of magnetic fields and formation of a current sheet. The total ejection of the flux rope will be effected only when magnetic reconnection takes place. Thus the model proposed by Forbes (1991) is so to speak a catastrophe-reconnection hybrid model. Regarding to this model, it should be mentioned that flux cancellations are often observed before the flare onset (Livi *et al.*, 1989). If the flux cancellation results from subphotospheric reconnection, it does not only decrease the normal magnetic field, but also adds flux to the flux rope to increase the current flowing through the flux rope. The flux cancellation may thus be regarded as a cause of a catastrophe.

1.4 Outline of the Thesis

In this thesis, evolution of the coronal magnetic field and plasma is investigated using MHD simulation and the magnetofrictional method. Horizontal flows on the photospheric level are considered as boundary conditions.

In Chapter 2, the dynamic formation of solar prominences is studied. To investigate the thermodynamic process, the radiative cooling, a phenomenological form of the coronal heating and field-aligned heat conduction are included in our numerical model. Three different combinations of the footpoint motions and the initial field configurations are considered: (1) a footpoint shearing motion imposed on a single magnetic arcade, (2) a shearing motion and a converging motion consecutively applied to a single magnetic arcade, and (3) parallel and antiparallel shearing motions imposed between two bipolar regions. Each case has yielded a prominence with a different field geometry.

Chapter 3 deals with quasi-static evolution of a magnetic arcade subject to a shearing motion. Firstly, an MHD simulation is performed in a low β isothermal plasma. Secondly, static equilibria are constructed using the magnetofrictional method. The purpose of this study is to find out whether a weak equilibrium exists for a finite shear and to find the asymptotic behaviour of the arcade evolution as the shear increases indefinitely.

In Chapter 4, nonzero resistivity is applied to sheared magnetic arcades. A threshold shear for magnetic reconnection is sought and the effect of resistivity is investigated in view of the current sheet development. Different characteristics of the arcade evolution are investigated for different values and patterns of resistivity.

Chapter 5 summarizes the principal results of this thesis and contains discussions. Appendix A presents a description of the numerical algorithm employed in Chapter 2.

CHAPTER 2

Formation of Solar Prominences

2.1 Introduction

Solar prominences consist of cool (5000–8000 K) and dense ($\sim 10^{11}\,\mathrm{cm}^{-3}$) material embedded in the hot (10^6 K) and tenuous ($\sim 10^9\,\mathrm{cm}^{-3}$) solar corona. The location of prominences above the magnetic neutral lines (Babcock and Babcock, 1955), on either side of which the radial component of magnetic fields is oppositely directed, indicates that the dense plasma is supported by magnetic fields. Prominences can be grouped into two categories according to the direction of the magnetic field component perpendicular to the prominence plane and that of the plausible potential field deduced from the photospheric magnetic polarities across the neutral line. In the normal polarity (hereafter called NP) prominences, the two field directions are parallel, while in the inverse polarity (hereafter called IP) prominences, the two field directions are antiparallel. The ratio of the population of the two types observed by coronagraphs is about 3 (IP) to 1 (NP) (Leroy, 1989). However, NP prominences are located lower than IPs so that the former are more difficult to detect than the latter. According to studies on the prominence heights, low-lying prominences are more abundant than high prominences (Billings and Kober, 1957).

There have been good reviews on the observations of solar prominences (e.g., Martin, 1973, 1990; Hirayama, 1985; Priest, 1989). Here we briefly summarize the observations relevant to the formation of prominences. The magnetic field vector in prominences is highly aligned along the prominence axis with an angle of about 25° (Leroy, 1989). The photospheric fields also tend to align along the magnetic neutral line before a prominence is formed, and this magnetic

shear is considered as one of the necessary conditions for prominence formation (Martin, 1990). Sometimes shearing mass motions are also observed during prominence formation in two different patterns. In one type, the velocity vectors are oppositely directed across the neutral line, while in the other the velocity vectors are parallel on both sides of the neutral line but increase in magnitude towards the neutral line (Rompolt and Bogdan, 1986). Another remarkable feature associated with prominence formation is the flux cancellation, in which two flux elements of opposite polarities come close to each other and disappear in the magnetogram. The observation of flux cancellation indicates the existence of converging flows towards the neutral line and magnetic reconnection either above or below the neutral line. In addition, arcades of closed field lines are observed to lie over prominences and a dark cavity with a low electron density is often observed between the prominence and the overlying arcade (Waldmeier, 1970). It was naturally speculated that cavities are consequences of the depletion caused by condensation of material into the prominence (Engvold, 1989). Saito and Tandberg-Hanssen (1973), however, found that the plasma mass in a cavity before depletion is not sufficient to supply the mass of the prominence. The presence of the overlying arcades may suggest that prominences are formed above neutral lines within a single bipolar arcade. However, a survey of quiescent prominences by Tang (1987) revealed that more prominences are formed between bipolar regions than inside a bipolar region.

Investigations of prominence formation are usually performed in two directions. The first direction is related to the cooling and condensation of plasma, which is attributed to thermal instability. In the coronal plasma, the loss of energy per volume by radiation is proportional to the density squared and a function of temperature, which increases with decreasing temperature in some temperature range (e.g., Cox and Tucker, 1969). In a perturbed plasma, which is dense or cool enough to overcome adiabatic and nonadiabatic heat flows, the perturbation can grow until a new equilibrium is reached where the radiative loss decreases with decreasing temperature. The

condensation by this thermal instability has been studied analytically (Field, 1965; Chiuderi and Van Hoven, 1979; Van Hoven and Mok, 1984; Steinolfson and Van Hoven, 1984; Van Hoven *et al.*, 1986; An, 1985; 1986) and numerically (Hildner, 1974; Sparks *et al.*, 1990). The second direction of prominence studies is related to dynamic mechanisms, which can perturb plasma strongly enough for the onset of a thermal instability. By a numerical simulation, Forbes and Malherbe (1991) found that a loop prominence, which appears after a flare, can be formed by fast shocks generated by reconnection jets. Wu *et al.* (1990) performed a numerical simulation of the formation of a quiescent prominence by injecting high density material ballistically from the lower atmosphere. This assumption, however, can hardly be regarded as a general condition for prominence formation. Recently Choe and Lee (1992) showed that a photospheric footpoint shear in a magnetic arcade can create a coronal condition where a prominence can be formed.

In this chapter, we present results of numerical simulations on the prominence formation, where only the observationally established photospheric conditions are imposed as boundary conditions. Case 2A (Section 2.3) deals with the prominence formation by a shearing motion, Case 2B (Section 2.4) is concerning the formation of an IP prominence by a shearing and converging motion, and Case 2C (Section 2.5) treats the prominence formation between two bipolar regions. Mechanisms of prominence formation under various photospheric motions and field geometries are discussed.

2.2 Description of Modelling

In our simulation, a Cartesian geometry is adopted ignoring the curvature of the solar surface (see Figure 2.1). Since the prominence-field configurations look more or less alike along the magnetic neutral line, all the variables are assumed to be invariant in this direction (the z-coordinate axis) although the z-components of vector quantities are taken into account. The

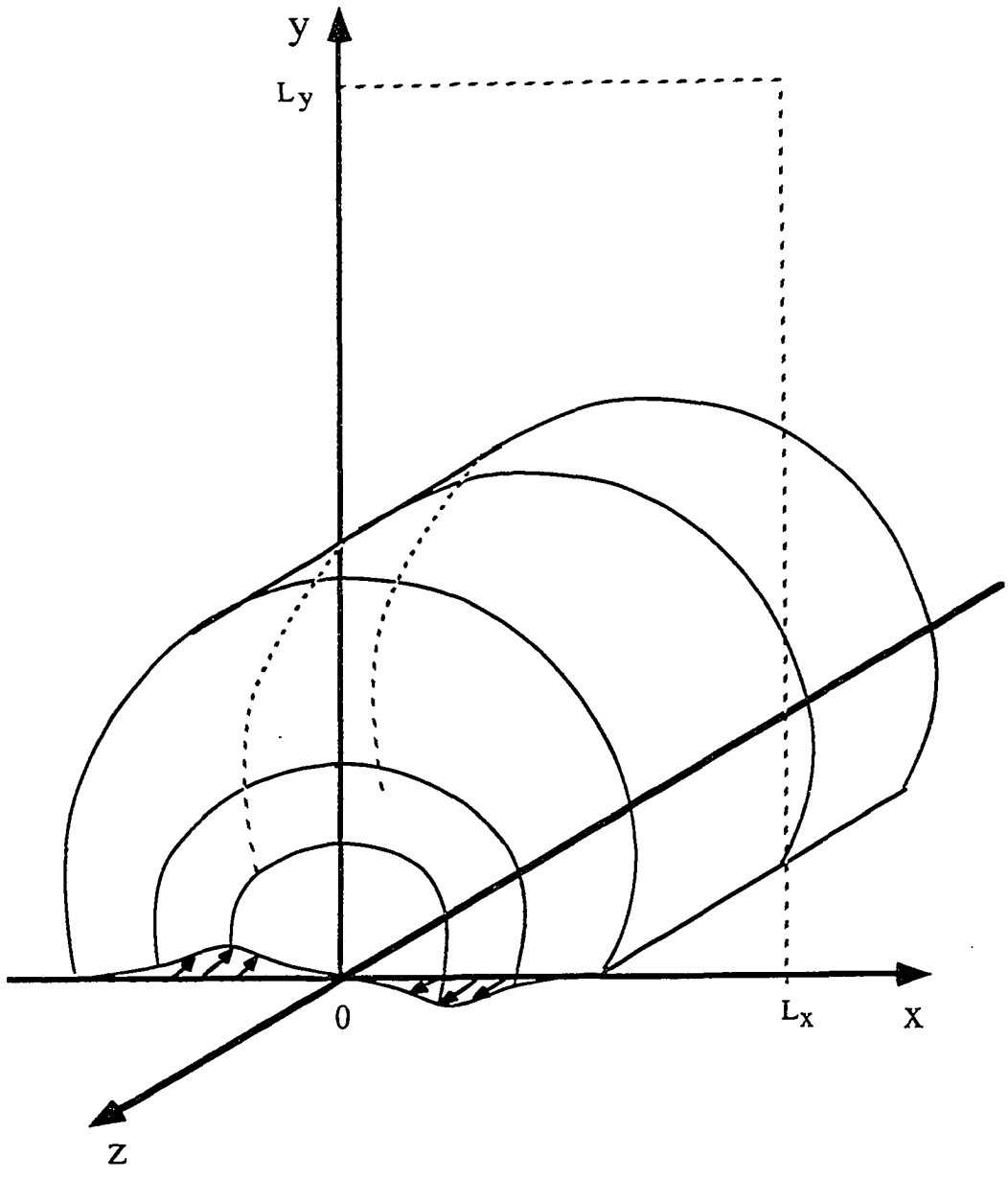

Figure 2.1 Sketch of the coordinate system and field geometry in the numerical modelling. The field lines and boundary motions shown are specifically regarding Case 2A. The y-axis is the vertical axis and the z-axis runs along the magnetic neutral line. The computational domain is a rectangular area whose dimension is $L_x \times L_y$.

vertical coordinate is designated by y, and the horizontal coordinate perpendicular to the neutral line by x. Assuming the symmetry of the initial condition and perturbations across the y axis, our computation is performed only in one quadrant of the x-y plane.

The governing equations for the simulation are a full set of magnetohydrodynamic (MHD) equations including gravity, radiative cooling, thermal conduction and heating as follows:

$$\frac{\partial \rho}{\partial t} + \nabla \cdot (\rho \mathbf{v}) = 0 \tag{2.1}$$

$$\rho(\frac{\partial \mathbf{v}}{\partial t} + \mathbf{v} \cdot \nabla \mathbf{v}) = -\nabla p + \mathbf{J} \times \mathbf{B} + \rho \mathbf{g} + \nabla \cdot (\rho \nu \nabla \mathbf{v}) \tag{2.2}$$

$$\begin{aligned} &\frac{\partial \psi}{\partial t} + \mathbf{v} \cdot \nabla \psi = \eta \nabla^2 \psi, \\ &B_x = -\frac{\partial \psi}{\partial y}, \qquad B_y = \frac{\partial \psi}{\partial x} \end{aligned} \tag{2.3}$$

$$\frac{\partial B_z}{\partial t} = \frac{\partial}{\partial x}(v_z B_x - v_x B_z) + \frac{\partial}{\partial y}(v_z B_y - v_y B_z) + \nabla \cdot (\eta \nabla B_z) \tag{2.4}$$

$$\begin{aligned} \frac{\partial T}{\partial t} = &- \mathbf{v} \cdot \nabla T - (\gamma - 1) T \nabla \cdot \mathbf{v} \\ &+ (\gamma - 1)\frac{T}{p}(\nabla \cdot \kappa_{\parallel} \nabla_{\parallel} T + \eta J^2 + H - C) \end{aligned} \tag{2.5}$$

$$\mathbf{J} = \nabla \times \mathbf{B} \tag{2.6}$$

$$p = \rho R T \tag{2.7}$$

where all quantities are expressed in a nondimensionalized form by a proper normalization. The reference values of the physical quantities are tabulated in Table 2.1. The mass density ρ is referenced to the initial density ρ_0^0 at the base, the temperature T to the initial uniform temperature T_0, the pressure p to $p_0^0 = \rho_0^0 k_B T/m$, where k_B is the Boltzmann constant and m is the mean particle mass set to one half of the proton mass. The constant γ is the ratio of specific heats taken to be $5/3$. The magnetic field $\mathbf{B}$ is normalized by $B_0 = (4\pi p_0^0)^{1/2}$ in CGS units and the velocity $\mathbf{v}$ by $v_0 = \gamma^{-1/2} c_s$, where $c_s = (\gamma p_0^0/\rho_0^0)^{1/2}$ is the sound speed. Note that B_0 and v_0 correspond to the magnetic field strength and the Alfvén speed for the plasma

with $\beta = 2$, where β is the ratio of plasma pressure to magnetic pressure. The position vector x is normalized by the density (pressure) scale height at the bottom $L_0 = (k_B T_0)/(mg_0)$, the time t by $t_0 = L_0/v_0$, and the energy density by $p_0^0 = {B_0}^2/4\pi$. The gravity $\mathrm{g} = -g\hat{y}$ is a function of y given by

$$g(y) = \frac{4\pi G M_\odot}{(R_\odot + y)^2} = g_0 \frac{{R_\odot}^2}{(R_\odot + y)^2} \tag{2.8}$$

where G is the gravitational constant, $M_\odot$ the solar mass, $R_\odot$ the solar radius and $g_0 = 2.74 \times 10^4\,\mathrm{cm\,s^{-2}}$ is the surface gravity which is equal to the unit acceleration $a_0 = v_0/t_0$. The resistivity η and the kinematic viscosity ν are also normalized in units of $L_0 v_0$ and the normalized η is the inverse of the Lundquist number for the plasma whose Alfvén speed is v_0.

TABLE 2.1 Normalization Units and Symbols in Chapter 2

Quantity	Symbol	Unit	Value in CGS
Length	x	$L_0 = (k_B T_0)/(mg_0)$	6.0×10^9
Density	ρ	ρ_0^0	8.4×10^{-15}
Number Density	n	n_0^0	5.0×10^9
Temperature	T	T_0	10^6
Pressure	p	p_0^0	1.4
Magnetic Field	B	$B_0 = (4\pi p_0^0)^{1/2}$	4.2
Velocity	v	$v_0 = (p_0^0/\rho_0^0)^{1/2}$	1.3×10^7
Time	t	$t_0 = L_0/v_0$	4.7×10^2
Acceleration	a	$a_0 = v_0/t_0$	2.74×10^4

The inclusion of η and ν is solely for the purpose of numerical smoothing. The adopted values are $\eta \approx 10^{-4}$ and $\nu \approx 10^{-3}$, while in the solar corona the classical values (Spitzer, 1962)

are $\eta \approx 10^{-13}$ and $\nu \approx 10^{-4}$ after the same normalization. Although the resistivity used in Equations (2.3) and (2.4) does not generate such a large Joule heating that can affect the global energetics we use the classical value in the energy equation (Equation (2.5)) because a high current is seen to develop at the prominence site after condensation.

The heat conduction is considered only along the field lines because the perpendicular conductivity is more than ten orders of magnitude smaller than the parallel conductivity whose value is taken from Spitzer (1962) as

$$\kappa_{\parallel} = k_0 T^{5/2} = 9 \times 10^{-7} T^{5/2} \,\mathrm{erg\,s^{-1}\,cm^{-1}\,K^{-1}}, \tag{2.9}$$

where all quantities are in CGS units. For the optically thin atmosphere, the radiative cooling term C in Equation (2.5) is of the form

$$C = n_e n_H Q(T) = n^2 Q(T), \tag{2.10}$$

where n_e is the electron number density and $Q(T)$ the cooling function (Cox and Tucker, 1969; Tucker and Koren, 1971; McWhirter *et al.*, 1975; Raymond and Smith, 1977). An analytical fitting of $Q(T)$ to a piecewise continuous function $Q(T) = \chi_i T^{\alpha_i}$ has been attempted by Hildner (1974) and Rosner *et al.* (1978). The two functions are tabulated respectively in Tables 2.2 and 2.3 and plotted together in Figure 2.2. There are two major differences in the two functions, which can affect the numerical results. First, the difference $Q(10^5\ \mathrm{K}) - Q(10^6\ \mathrm{K})$ is larger in Hildner's function than in Rosner *et al.*'s. The cooling time scale is thus shorter with the former than with the latter. Secondly, the exponent α at $T = 10^6$ K is -1 by Hildner while 0 by Rosner *et al.*. Thus, the cooling term with the latter function is sensitive only to the density perturbation until the temperature reaches the value where the exponent α changes. We have tested both functions and found that the difference in cooling time scales is enhanced (reduced) in cases dominated by the temperature (density) perturbation.

TABLE 2.2 Radiation Loss Function by Hildner (1974)

T (K)	$\alpha(T)$	$\chi(T)$ [erg sec^{-1} cm^3]
$T < 1.5 \times 10^4$	+7.4	4.92×10^{-54}
$1.5 \times 10^4 < T < 8 \times 10^4$	+1.8	1.2×10^{-30}
$8 \times 10^4 < T < 3 \times 10^5$	0	8.0×10^{-22}
$3 \times 10^5 < T < 8 \times 10^5$	−2.5	3.94×10^{-8}
$8 \times 10^5 < T$	−1.0	5.51×10^{-17}

TABLE 2.3 Radiation Loss Function by Rosner *et al.* (1978)

T (K)	$\alpha(T)$	$\chi(T)$ [erg sec^{-1} cm^3]
$10^{4.3} < T < 10^{4.6}$	0	$10^{-21.85}$
$10^{4.6} < T < 10^{4.9}$	+2	10^{-31}
$10^{4.9} < T < 10^{5.4}$	0	$10^{-21.2}$
$10^{5.4} < T < 10^{5.75}$	−2	$10^{-10.4}$
$10^{5.75} < T < 10^{6.3}$	0	$10^{-21.94}$
$10^{6.3} < T < 10^{10.7}$	−2/3	$10^{-17.73}$

For the coronal heating term H, we assume that

$$H = nh(y), \tag{2.11}$$

where $h(y)$ is a time-independent function. The initial thermal equilibrium is achieved by setting $C = H$ initially, whereby we obtain

$$h(y) = n_0(y)\chi_0 {T_0}^{\alpha_0}. \tag{2.12}$$

In this study, the solar corona is assumed to consist of fully ionized hydrogen gas and be initially isothermal with a temperature of 10^6 K and in hydrostatic equilibrium. This temperature

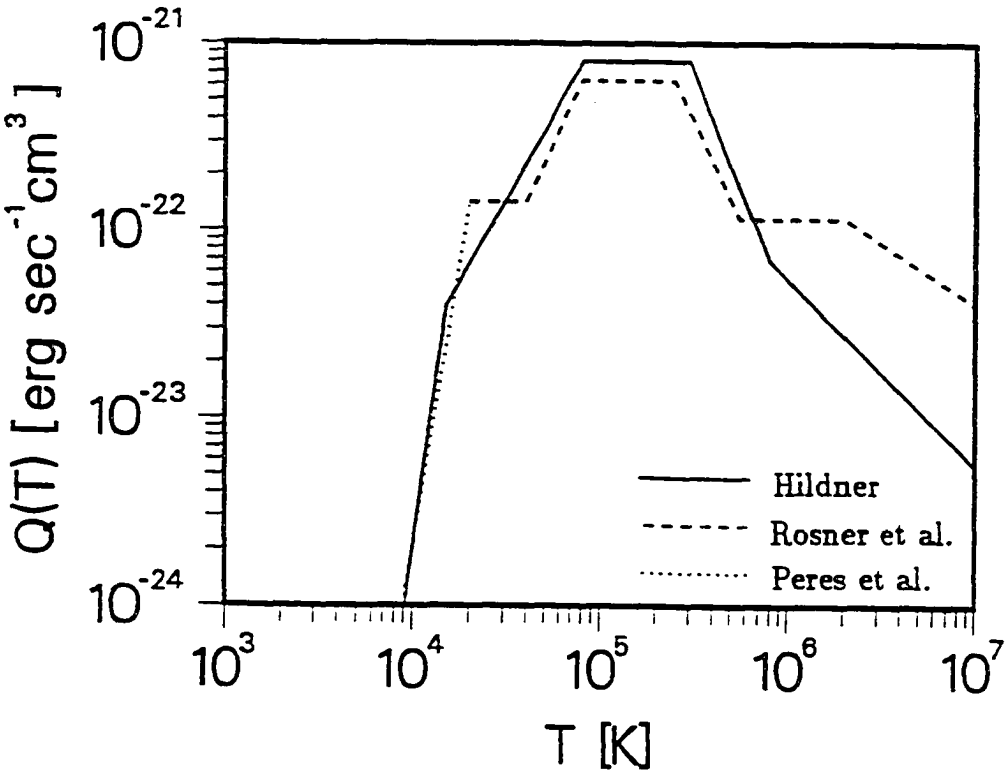

Figure 2.2 Analytic fits of the radiation loss function $Q(T)$. The solid line is from Hildner (1974) and the dashed from Rosner *et al.* (1978). Peres *et al.*'s (1982) curve (dotted line) is attached to Rosner *et al.*'s below 2×10^4 K (from Choe and Lee, 1992).

gives the scale height $L_0 = 6 \times 10^4$ km at $y = 0$. The initial magnetic field is assumed to be a potential field and obtained by numerically solving the Laplace equation $\nabla^2\psi = 0$ with a given B_y profile at the bottom boundary. With no initial motions, the corona in the computational domain is in mechanical and thermal equilibrium.

The boundary conditions at $x = 0$ are determined by the symmetry property. The other lateral boundary and the upper boundary are assumed to be open. Here the zeroth order extrapolation is used for $\rho - \rho_0$ and other variables except ψ, for which the convective derivative is set to zero. At the bottom boundary, the horizontal velocities v_x and v_z are given and no flow across the boundary is allowed, i.e., $v_y = 0$, considering the far higher density of the photosphere. This condition for v_y allows us to determine the time evolution of $\psi(x, y = 0)$ by simply integrating the governing equation (Equation (2.3)). The density and temperature are set to be constant so that the bottom boundary may behave like a pressure and heat reservoir. The toroidal field B_z is obtained by integrating the governing equation (Equation (2.4)) with one side spatial differencing with respect to y.

A uniform 127×257 grid is used for Case 2A and nonuniform 101×101 grids are employed for Cases 2B and 2C. Our test simulations show that a finer resolution yields a higher maximum density in the prominence. Therefore, the maximum density reported in this paper should be interpreted as a low end of the possible maximum density in reality.

The governing equations are finite-differenced and integrated in time using the semi-implicit scheme (Harned and Schnack, 1986). Although this scheme is free from the time-step restriction by the Alfvén and fast modes, the employed time-step size is 4-10 times the CFL time-step due to the nonlinearity of the problems. The heat conduction term is treated by the alternating direction implicit method as in the simulation of Sparks *et al.* (1990). The readers are referred to Appendix A for a detailed description of the numerical procedure.

2.3 Formation of Normal Polarity Prominences by Footpoint Shear (Case 2A)

In this section, we present the formation of NP prominences by the simplest footpoint motion, the shear, following Choe and Lee (1992). The initial B_y profile at $y = 0$ is given by

$$B_y(x, y = 0, t = 0) = B_{y0}\left\{\exp\left(-\frac{(x + X_0)^2}{2{X_w}^2}\right) - \exp\left(-\frac{(x - X_0)^2}{2{X_w}^2}\right)\right\}, \qquad (2.13)$$

where $B_{y0} = 12\,\mathrm{G}$, $X_0 = 0.4\,L_0$, and $X_w = 0.27\,L_0$. The shear velocity pattern imposed at the bottom boundary is

$$v_z(x) = \frac{1}{2}V_{z0}\left\{\tanh\left(\frac{x - X_a}{X_c}\right) - \tanh\left(\frac{x - X_b}{X_c}\right) + \tanh\left(\frac{x + X_a}{X_c}\right) - \tanh\left(\frac{x + X_b}{X_c}\right)\right\}, \qquad (2.14)$$

where $V_{z0} = 4\,\mathrm{km\,s^{-1}}$, $X_a = 0.21\,L_0$, $X_b = 0.59\,L_0$, $X_c = 0.04\,L_0$. The shear is thus localized around $x = \pm(X_a + X_b)/2$ with an approximate halfwidth of $(X_b - X_a)/2$. Starting from zero, the shear velocity is increased to the above value in 470 s. The electron number density at the bottom boundary is taken to be $5 \times 10^9\,\mathrm{cm^{-3}}$ and the plasma β at the origin is initially 0.2. The cooling function by Hildner (1974) is employed for the reported case.

The shear velocity v_z creates the field component B_z, whose pressure force expands the field lines with material attached to them. The first stage of evolution is almost adiabatic; effects of the heating, radiative cooling, and thermal conduction are small compared to the adiabatic cooling. As shown in Figure 2.3, the expansion of the arcade decreases the temperature over the whole domain. The local density is decreased in the lower part of the arcade where the expansion is most active, while the local density above that part is increased because higher density material from below is transported upward by the expanding field lines. The adiabatic cooling causes the enhancement of radiative cooling, which becomes more and more dominant in the temperature variation of plasma as the temperature drops. A runaway cooling—thermal instability—is thus

effected. At $t \approx 7500\,\mathrm{s}$ the temperature drops quickly to about $10^4\,\mathrm{K}$ in an oval-shaped region at a height of $0.5\,L_0 \approx 3 \times 10^4\,\mathrm{km}$ as shown in Figure 2.3. Due to the sudden drop of pressure the material in the vicinity is sucked into the cool region with a speed of several $10\,\mathrm{km\,s^{-1}}$. Although the material flows into the oval-shaped region from all directions, the dominant flow is along the field lines from the lower atmosphere. The oval-shaped patch contracts along the field lines increasing the plasma density. Above and below this region, thermal instability takes place successively upward and downward. This is due to the variation of the onset time for thermal instability for different field lines. The condensed material thus forms a sheet-like structure as shown in the third column of Figure 2.3 ($t \approx 9400\,\mathrm{s}$). The density of the condensed material reaches at the peak about 70 times its initial value, which corresponds to the number density of $n = 2 \times 10^{11}\,\mathrm{cm^{-3}}$. It should be mentioned that we observed a higher value of maximum density by employing a finer grid. This high density material presses down the field lines to form a configuration with a dip, which is the essential signature of the Kippenhahn-Schlüter prominence model.

It should be noted that the length of the cooled regions in the field line direction increases with height, and the uppermost cooled region has even an umbrella-like shape as shown in Figure 2.3. The more the cooled region is elongated the more difficulty it has in contracting into a small volume at the field line apex due to the higher gravitational force component in the field direction. Above a certain height the condensed material is partly shed along field lines. In a greater height, the newly cooled material cannot even condense towards the center any more, but condenses towards the edges of the low temperature region sliding down along the field lines (see the fourth column of Figure 2.3). The upward growth of the vertically elongated prominence is thus saturated. Since the sliding condensed material is of low temperature and of low pressure, material is sucked from below into the condensed region while the whole structure moves downward. As seen in Figure 2.4, at $t \approx 14500\,\mathrm{s}$ the falling material is finally merged into

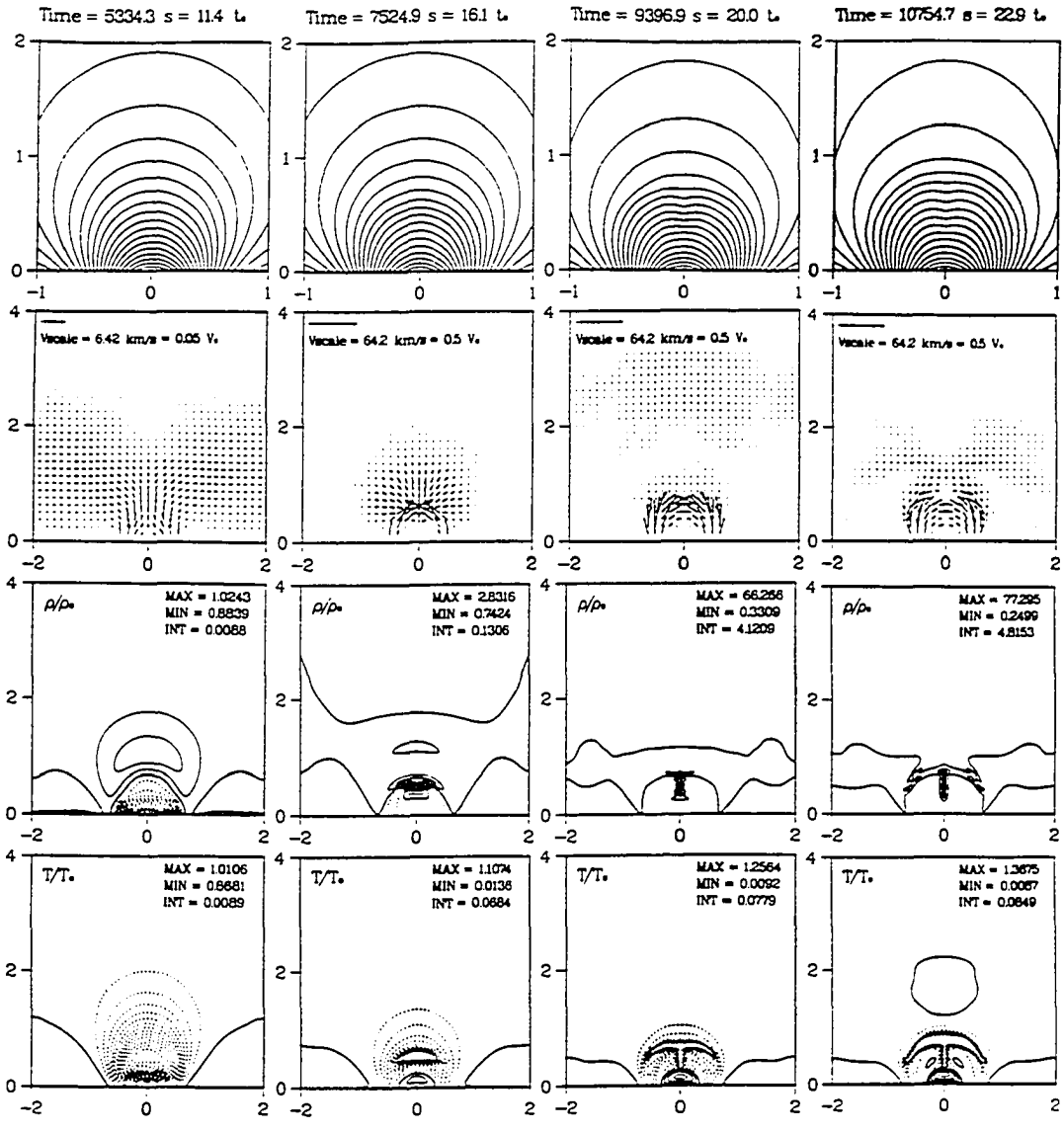

Figure 2.3 Time evolution of the magnetic arcade in Case 2A. From the top, the four rows show respectively the magnetic field lines, velocity fields, ratio of density to the initial local value, and ratio of temperature to the initial value. The time increases from left to right. In the contour plots, the solid lines represent values greater than 1, the dashed lines values less than 1, and the thick solid lines the value of 1. In the upper right corner of each contour plot are shown the maximum and minimum values and the interval between adjacent contours (from Choe and Lee, 1992).

the chromosphere, and the depletion of material results in an arc-shaped cavity of low density (0.01–$0.2\,\rho_0$), low temperature ($\sim$ 1–2 $\times$ 10^5 K) and low pressure (10^{-3}–$10^{-2}\,p_0$) around the prominence. The temperature, however, is still increasing due to the dominance of the heating and expected to recover the initial coronal temperature as observed by Bessey and Liebenberg (1984). It is noteworthy that the cavity in our simulation is formed by the drainage of cooled material. The pre-existing material in the cavity volume does not contribute to the prominence mass and most of the prominence mass is supplied by the siphon-type field-aligned flows. In the mechanism of cavity formation proposed by An *et al.* (1985), the material slides down along the field lines leaving a cavity if the cooling time scale is longer than the free-fall time scale. In our simulation, however, the formation of a prominence or a cavity is determined by the pressure gradient and the component of the gravitational force in the field direction at the edge of the cooled region. We have found that the length of cooled regions along field lines increases with the height and that the inclination of field lines at the edge of the cooled region is larger for outer field lines than for inner ones. This result can be expected for a self-similar expansion of arcades. The cooled material in the lower part of the arcade can thus readily contract towards the field line apex whereas in the upper part the condensed material slides down along the field lines. The NP prominences can thus be formed favorably on rather flattened field lines. This may explain the reason why the NP prominences lie in the low corona, for newly emerging flux tubes may be rather flat at their apex.

If the plasma β is too low, field line dips cannot be formed. In our prominence model, dips are formed on field lines where the plasma β is as low as 0.1, which is quite low in view of the "conventional" criterion for dip formation, $\beta \geq 1$. Here we roughly derive a criterion for the dip formation. Firstly, we assume that the corona without a prominence is in a

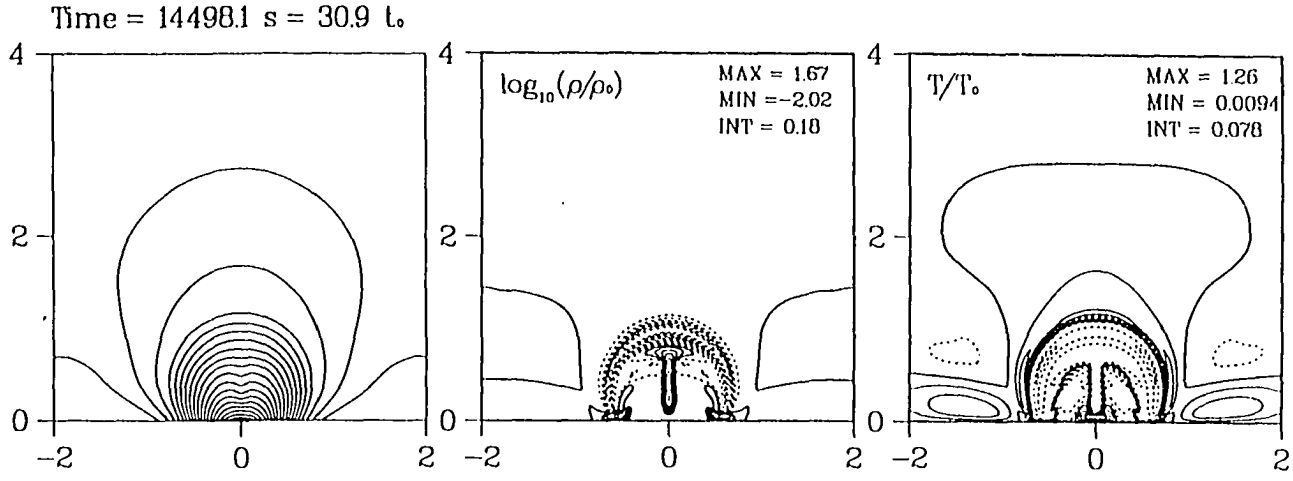

Figure 2.4 Normal polarity prominence with a coronal cavity. Field lines and contours of $\log_{10}(\rho/\rho_0)$ and T/T_0 are plotted for Case 2A at $t = 1.45 \times 10^4$ s (from Choe and Lee, 1992).

hydrostatic equilibrium embedding a magnetic arcade which is force-free in the neighborhood of the symmetry axis $x = 0$. Then we have

$$\rho_o g = -\frac{dp}{dy}, \tag{2.15}$$

$$\frac{B^2}{4\pi R_o} = -\frac{d}{dy}\left(\frac{B^2}{8\pi}\right), \tag{2.16}$$

where R is the radius of curvature of field lines. Throughout our derivation, all the variables are evaluated at $x = 0$ and thus functions of y only. The subscript "o" denotes values just before the prominence formation while the subscript "p" will indicate values just after the prominence formation. Secondly, we also assume that the pressure $p(x = 0, y)$ and the magnitude of the magnetic field $B(x = 0, y)$ change little after the formation of a prominence in the region inside the prominence. Although this assumption is not always valid, it approximately holds if the depth of a dip is small compared to the radius of curvature of the original field lines as in our simulation. By this assumption, $p_o \approx p_p$ and $B_o \approx B_p$, and the subscripts will be deleted for these two variables. After a prominence is formed, the plasma is in an MHD equilibrium with dips on field lines. Then

$$\rho_p g = -\frac{dp}{dy} + \frac{B^2}{4\pi R_p} - \frac{d}{dy}\left(\frac{B^2}{8\pi}\right). \tag{2.17}$$

Note that the curvature normal of the field lines is now upward. Setting $\Lambda_o = (k_B T_o)/(m_H g)$, $\Lambda_p = (k_B T_p)/(m_H g)$, $\beta = 8\pi p/B^2$, we can rewrite the above equation as

$$\frac{p}{\Lambda_o} = \frac{p}{\Lambda_p} + \frac{2p}{\beta R_p} + \frac{2p}{\beta R_o}. \tag{2.18}$$

When the field line just starts to be depressed, $R_p = \infty$ and

$$\beta = \frac{2\Lambda_o}{R_o\left(1 - \frac{\Lambda_p}{\Lambda_o}\right)}. \tag{2.19}$$

Since $(\Lambda_p/\Lambda_o) \approx 10^{-2} \ll 1$, the criterion for dip formation is approximately

$$\beta > \frac{2\Lambda_p}{R_o} \equiv \beta_{min}. \tag{2.20}$$

Considering the width of the weak field corridor ($\sim 2 \times 10^4$ km), the smallest radius of curvature

of field lines over this corridor may be about 10^4 km. With $R_o \approx 10^4$ km and $\Lambda_p \approx 500$ km, the minimum value of plasma β is $\beta_{min} \approx 0.1$. Since outer field lines or sheared field lines have a larger radius of curvature the lowest allowable β can be even smaller.

2.4 Formation of Inverse Polarity Prominences by Shearing and Converging Motions (Case 2B)

The field configuration of the Kuperus-Raadu type inverse polarity prominence has a magnetic island within an arcade, which can be obtained from a potential-like field geometry through magnetic reconnection. Previous studies suggested that a shear imposed on a single magnetic arcade cannot develop a current sheet and reconnection of field lines (Biskamp and Welter, 1989; Klimchuk and Sturrock, 1989; Finn and Chen, 1990; Steinolfson, 1991). Recent studies, however, has shown that magnetic reconnection can be triggered in a highly sheared magnetic arcade (Mikić and Linker, 1994; see also Chapter 4 of this thesis). The angle of shear can be increased not only by a shearing motion but also by a converging motion if the arcade is initially sheared. The observation of flux cancellation (Martin, 1990) suggests that converging motions imposed on a sheared field may drive magnetic reconnection. Based on this observation, van Ballegooijen and Martens (1989) put forward a plausible scenario that prominences are formed by photospheric reconnection driven by converging motions. The simulation studies by Lee (1990) and Inhester *et al.* (1992) have indeed shown that a converging motion superposed to a shearing motion can drive magnetic reconnection and result in a field configuration with a magnetic island. The present study proceeds one step further from this with all the thermodynamic effects taken into account.

In this case, the initial B_y profile at $y = 0$ is given by

$$B_y(x, y = 0, t = 0) = B_{y0}\frac{x}{X_0}\exp\left(\frac{1}{2} - \frac{x^2}{2X_0^2}\right), \tag{2.21}$$

where $B_{y0} = 50\,\mathrm{G}$ and $X_0 = 0.32\,L_0$. The resulting field configuration has a large curvature compared to the footpoint distance, which is in contrast with the field in the former NP case. The shear pattern employed is

$$v_z(x) = V_{z0}\tanh\left(\frac{x}{X_0}\right)\exp\left(-\frac{x^2}{4X_0^2}\right), \tag{2.22}$$

where $V_{z0} = 4\,\mathrm{km\,s^{-1}}$. The converging velocity profile is given by

$$v_x(x) = -\frac{1}{2}V_{x0}\left(\tanh(\frac{x + X_a}{X_b}) + \tanh(\frac{x - X_a}{X_b})\right)\tanh^2\left(\frac{30x}{X_L}\right)\exp\left(\frac{3x^2}{X_L^2}\right), \tag{2.23}$$

where $V_{x0} = 2\,\mathrm{km\,s^{-1}}$, $X_a = 0.23\,L_0$, $X_b = 0.45\,L_0$ and $X_L = 4\,L_0$. With this converging velocity, the normal magnetic field at the bottom boundary always remains finite. The shear velocity is increased from zero at $t = 0$ to the full value in 430 s, kept constant up to $t = 1.7\times10^4$ s and decreased to zero at $t = 2.6 \times 10^4$ s. The converging velocity is increased from zero to its full value between $t = 6.0 \times 10^3$ s and $t = 6.9 \times 10^3$ s, kept constant until $t = 2.6 \times 10^4$ s and decreased to zero at $t = 3.0 \times 10^4$ s. The density at the bottom boundary is taken to be $2 \times 10^9\,\mathrm{cm^{-3}}$, which gives a longer cooling time than in Case 2A.

It was shown in Choe and Lee (1992) that a mild converging motion, when added to a shearing motion, promotes the radiative cooling of material by increasing the density. The initial evolution of the arcade in the present case is similar to that in Case 2A, i.e., as the plasma is cooled down adiabatically by the arcade expansion, the radiative cooling becomes more and more dominant over the heating. The central part of the arcade is first drastically cooled down to the prominence temperature, but the cooled material bifurcates and condenses downwards

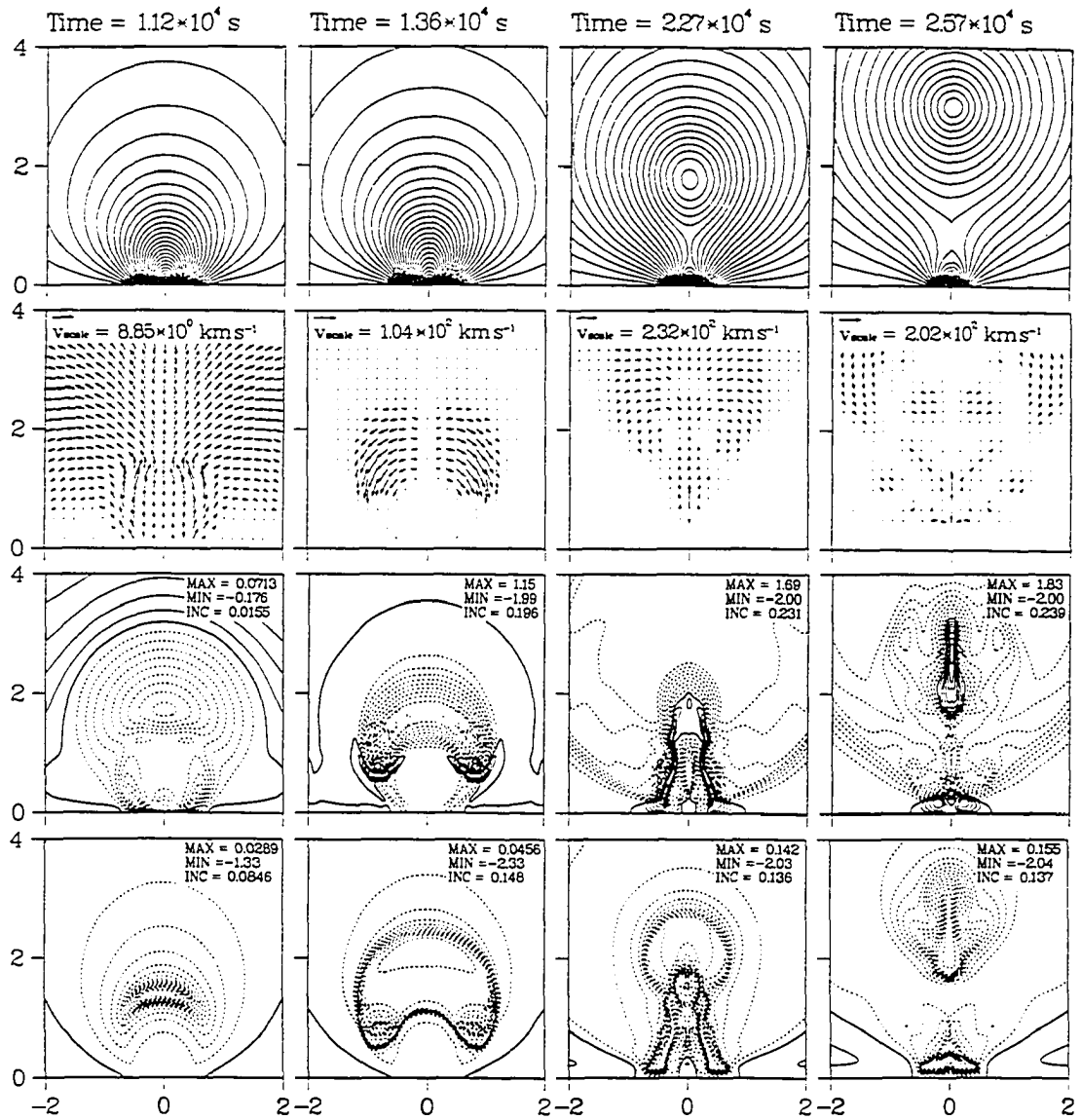

Figure 2.5 Time evolution of the magnetic arcade in Case 2B. Time increases from left to right. From top to bottom, the four rows show respectively the magnetic field lines, velocity fields, contours of $\log_{10}(\rho/\rho_0)$ and contours of $\log_{10}(T/T_0)$. In the contour plots, the solid lines represent values greater than 0, dashed lines values less than 0, and the thick solid lines the value of 0. The maximum and minimum values and the increment between adjacent contour levels are shown in the upper right corner of each contour plot.

along the field lines (see the second column of Figure 2.5), which is attributed to the high field-aligned gravity due to a high curvature of field lines. Above and below this region, plasma cools successively and condenses downwards along the field lines. A cavity is thus formed without any prominence at the field line apices.

As the footpoints get closer a current layer develops along the lower y-axis and fields lines are reconnected (the third column of Figure 2.5). The enhanced density in the magnetic island triggers a thermal instability and a swift cooling to the prominence temperature takes place in the upper part of field lines where plasma is most compressed. Due to the high curvature of the looped field lines, the cooled material cannot condense on the top of the field lines, but moves downwards along the field lines. The condensed material is finally accumulated at the bottom of field lines in the island to form a sheet-like structure which extends from the center to the lower boundary of the island. A minimum temperature of 8500 K and a density increase of 110 times are attained at $t = 26800$ s (Figure 2.6). The prominence formed in Case 2B is located far higher ($\sim$ 2-4 L_0) than the NP prominence in Case 2A, which is consistent with the statistics that IP prominences have a larger population than NP prominences above a certain height (Leroy, 1989). It is also noted that this mechanism is not affected by the plasma β. The plasma β in our prominence is about 0.01. As shown in Figure 2.6, the region in the island, where material is depleted into the prominence, constitutes a cavity, which has a lower pressure ($\sim 4 \times 10^{-3} p_0$) than the surrounding cavity region formed before magnetic reconnection.

At the end of our simulation, the island contains about 62% of the total mass in the volume surrounded by the flux surface crossing the X-line, while the rest 38% is held in the arcade volume below the X-line. The prominence possesses 92% of the mass in the island. Since our simulation domain consists of the corona only, the mass of a prominence is limited to a portion of the coronal mass. The magnetic reconnection responsible for flux cancellation is, however, thought to take place just near or in the photosphere, for otherwise the reconnected flux tube

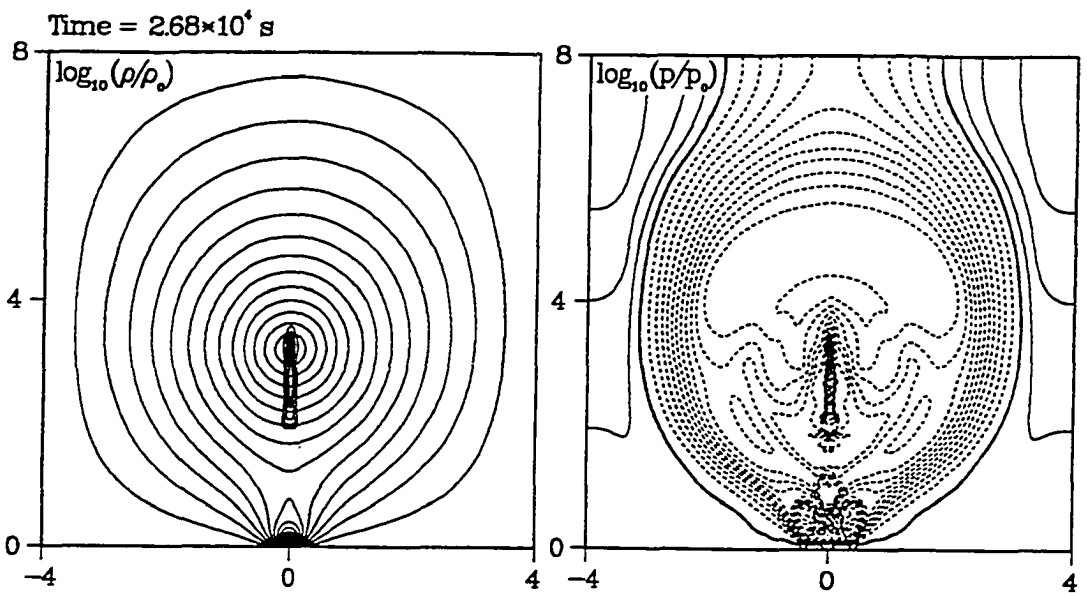

Figure 2.6 Density and pressure profiles of the inverse polarity prominence. On the left, contours of $\log_{10}(\rho/\rho_0) \geq 0$ at $t = 2.68 \times 10^4$ s in Case 2B are superimposed on the magnetic field lines. The corresponding contours of $\log_{10}(p/p_0)$ are shown on the right. The high density prominence material resides mostly at the bottom of field lines in the magnetic island. In the right panel, the lowest pressure appears in the mushroom-shaped region above the prominence (from Choe and Lee, 1993).

would have to make too long a journey to reach the photospheric level where the magnetic flux is measured. If the magnetic reconnection takes place in the photosphere or chromosphere, material of far higher density can be transported into the corona than in our simulation and even such a big prominence may be able to form that its mass is comparable to the whole coronal mass. The siphon flow can also contribute to the mass supply in a three dimensional geometry. Observations show that prominences are anchored in the photosphere by feet which are located with a 3×10^4 km separation (Schmieder, 1989). The feet can thus act as a mass transport channel between the prominence and the photosphere both for a siphon-type mass inflow and for the leakage of condensed material.

The stability of IP prominences is quite robust against lateral perturbations. However, one may not exclude the possibility of disintegration of the prominence structure if a reverse magnetic reconnection takes place. In one simulation, we turned off the footpoint motion after the prominence formation and let the system relax by itself for 10^4 s. The magnetic island and the prominence are found to rise to the end of simulation though slow. Observations show that most prominences have a tendency to rise rather than to descend (Zirin, 1988). Thus a reverse magnetic reconnection is thought to be relatively improbable in reality. However, if there exists a photospheric flow which takes energy away from the coronal field, the line-tied field may collapse downward leading to a reverse reconnection.

2.5 Formation of Prominences between Two Bipolar Regions (Case 2C)

The statistical study by Tang (1987) showed that more prominences are formed between two bipolar regions than inside one bipolar region. This is not surprising because a current sheet is expected to form inevitably when two bipolar regions are brought into contact. By magnetic reconnection, a connection is established between two originally unconnected arcades, and a

field geometry favorable to the prominence support is created. It is not necessary to bring the footpoints of two arcades close together to develop a current sheet. The expansion of arcades by shearing motions will also cause current sheet formation. Furthermore, the shear velocity pattern need not be antiparallel across the neutral line. No matter whether we have an antiparallel shear or a parallel shear as observed by Rompolt and Bogdan (1986), each arcade will expand separately and come into contact to form a current sheet. With an antiparallel shear, the photospheric magnetic field component along the neutral line, B_z, has the same direction on both sides of the neutral line as shown in Figure 2.7a. Observations sometimes show that the magnetic field component along the neutral line, B_z, is oppositely directed across the neutral line (Martin, 1990). This is definitely suggestive of a parallel footpoint motion (see Figure 2.7b). However, for a single arcade overlying the neutral line, an antiparallel B_z distribution cannot be achieved even if a parallel shear is imposed. Therefore, we may assert that where an antiparallel B_z distribution across the neutral line is observed, field lines anchored on the two sides are probably not interconnected.

It should be noted that the polarity of a prominence between two bipolar regions is the inverse polarity from the observational point of view regardless of the presence of magnetic islands because the direction connecting the two inner magnetic poles is always opposite to the direction connecting the two outer poles. Thus there is no equating the Kippenhahn-Schlüter type to the normal polarity in this case.

The initial field profile in our simulation is adopted from Low (1992), which takes on a quadrupolar topology:

$$\psi(x,y) = \frac{B_0}{k}\left[\exp(-ky)\cos(kx) - a\exp(-3ky)\cos(3kx)\right], \qquad (2.24)$$

where $B_0 = 50\,\mathrm{G}$, $k = \pi/(2\,L_x)$ with $L_x = 2\,L_0$ and a is taken to be 0.32. Note that, in the region $y > 0$, the field given above is bipolar for $a \leq 1/9$, quadrupolar with no neutral point for

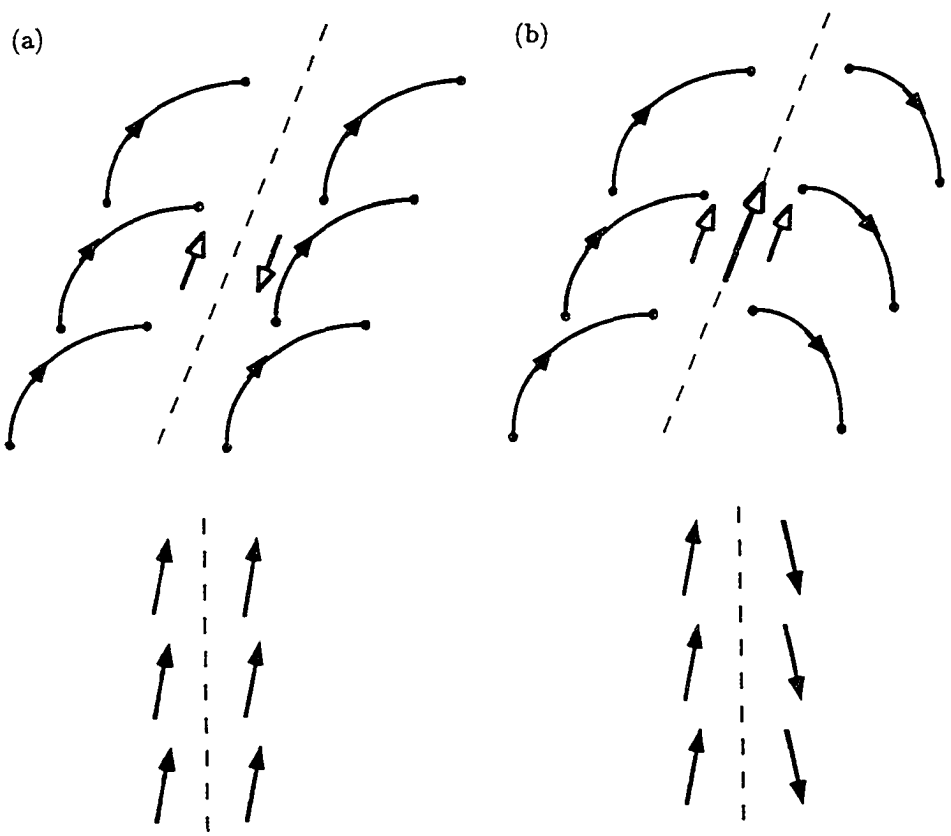

Figure 2.7 Schematic sketch of shear patterns, coronal field lines and the associated photospheric field directions between two bipolar regions. The lower figures show field directions at the footpoints projected on the horizontal plane. The direction of shear flows is indicated by light arrows and the field direction by dark arrows. (a) With an antiparallel shear, the photospheric fields are parallel on both sides of the neutral line. (b) With a parallel shear, the photospheric field components along the neutral line are antiparallel across the neutral line.

$1/9 < a \leq 1/3$, and has an X-type neutral point for $a > 1/3$. The initial field configuration is shown in Figure 2.8, in which three polarity inversion lines are shown at $x = \pm X_n = \pm 0.99\, L_0$ and $x = 0$ in the x-z plane. We have performed two simulations with different shear patterns: one with an antiparallel shear (Case 2Ca) and the other with a parallel shear (Case 2Cb). The antiparallel shear profile is given as follows:

$$v_z(x, y = 0) = \begin{cases} -V_{z0} \sin(\dfrac{\pi x}{X_n}), & \text{if } |x| \leq X_n; \\ 0, & \text{if } |x| > X_n. \end{cases} \tag{2.25}$$

The parallel shear profile employed is:

$$v_z(x, y = 0) = \begin{cases} \dfrac{1}{2} V_{z0} \left[1 + \cos(\dfrac{\pi x}{X_n}), \right] & \text{if } |x| \leq X_n; \\ 0, & \text{if } |x| > X_n. \end{cases} \tag{2.26}$$

To accelerate the current sheet formation, a converging motion is added to the above shears.

$$v_x(x, y = 0) = \begin{cases} -V_{x0} \sin(\dfrac{\pi x}{X_n}), & \text{if } |x| \leq X_n; \\ 0, & \text{if } |x| > X_n. \end{cases} \tag{2.27}$$

The maximum shearing and converging velocities are taken respectively as $V_{z0} = 2\,\mathrm{km\,s^{-1}}$ and $V_{x0} = 0.5\,\mathrm{km\,s^{-1}}$ for both cases. Both v_z and v_x are increased starting from zero at $t = 0$ to their full values at $t \approx 860\,\mathrm{s}$. An electron number density of $2 \times 10^9\,\mathrm{cm^{-1}}$ is assumed along $y = 0$. With the above field and density, a minimum plasma β of 1.4×10^{-3} is obtained, but the β at the origin is rather high (~ 2) since a virtual X-point is located just below the origin. In the present case the cooling function by Rosner *et al.* (1978) is employed. As mentioned in Section 2, we set $v_y\,(y = 0) = 0$ in our calculation and the flux profile at $y = 0$ is thus fixed. Regarding this boundary condition, it is noted that Karpen *et al.* (1990) argued that relief of the line-tying at the origin may suppress the formation of a current sheet. Low (1991) refuted this

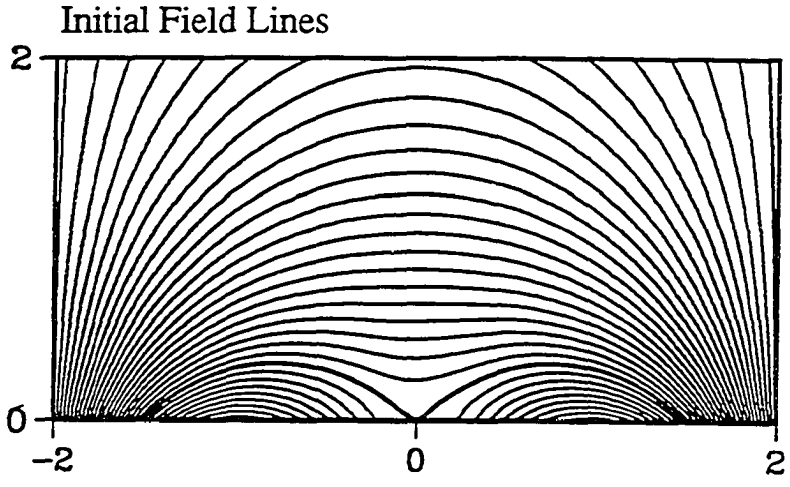

Figure 2.8 Initial magnetic field configuration in Case 2C. The height of the computational domain is three times as large as the vertical size of the panel shown. The thick solid line represents the field line passing through the origin, which initially separates three flux systems.

argument by giving a counterexample where the tip of the field line forming a current sheet can be maintained by a localized high but finite pressure.

Our results of Cases 2Ca and 2Cb turn out to be quite similar as expected, and we will mostly present the results of Case 2Ca. Our field configuration consists of three separate flux systems. As shown in Figure 2.9, the expansion of both arcades expels magnetic flux towards the neutral line at $x = 0$, and the overlying arcade is lifted up. The current layer first forms at the origin, where magnetic reconnection first takes place. As time grows, the X-point slowly moves up, field lines being reconnected successively. Due to the expansion of all three arcades, the temperature drops over the whole domain except just below the X-point. The temperature minimum is located in the lower part of the overlying arcade. The density is decreased inside the two expanding arcades, but increased in the overlying arcade. The highest density enhancement is, however, achieved in the current layer region, especially just above the X-point. The density

enhancement maximum moves up slowly while the temperature minimum remains at the same site.

The cooling mechanism in this case is very similar to that in Case 2A. In the first evolutionary stage, the adiabatic cooling leads the nonadiabatic processes. In Case 2C, however, the density near the temperature minimum is increased not only by the shear-induced expansion but also by magnetic reconnection. After $t \approx 15000\,\mathrm{s}$, the temperature decreasing rate is abruptly accelerated at the site of temperature minimum. As material is sucked into the cool region the density enhancement maximum also moves from the current layer region to the temperature minimum. The cooling to the prominence temperature takes place successively above and below the first cooled spot, forming a vertical sheet-like structure. By the end of the simulation, the prominence extends to a height of $1.2\,L_0$ (Figure 2.10a). Different from Case 2A, however, neither shedding of condensed material nor cavity formation can be seen due to the very flat field geometry. The small field line curvature also enables high density material to stay at the apex of upper field lines without dips although this equilibrium seems to be unstable to a strong perturbation. The plasma β in the prominence is less than 0.01, which makes it impossible for a dip to be formed by the gravity of the material. The dips on field lines in Case 2C are due to the intrinsic field topology associated with the presence of the X-point. Judging from our results, prominences between two bipolar regions are most likely to have a Kippenhahn-Schlüter type field geometry.

The outstanding difference of Case 2Cb from Case 2Ca lies in the fact that the reconnected field lines below the X-point have no z-component. The rising of the X-point and the overall field configuration is thus a little slower than in Case 2Ca. The thermal instability sets in around 17000 s, retarded compared to Case 2Ca. This results in a smaller height of the prominence as shown in Figure 2.10.

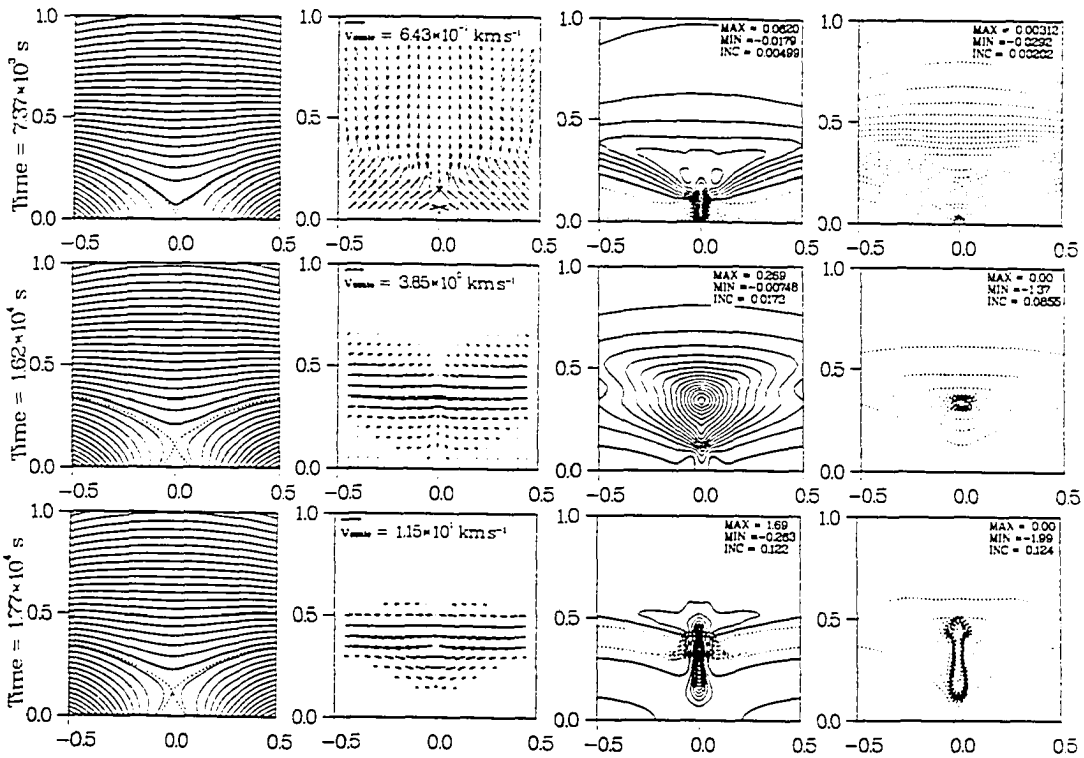

Figure 2.9 Time evolution of the magnetic arcade system in Case 2Ca. Time increases from top to bottom. From left to right, the four columns show respectively the magnetic field lines, velocity fields, contours of $\log_{10}(\rho/\rho_0)$ and contours of $\log_{10}(T/T_0)$. In the plot of field lines, the thick solid line represents the field line passing through the origin at $t = 0$ and the dashed line the field lines passing through the X-point. In the contour plots the solid lines represent values greater than 0, dashed lines values less than 0, and the thick solid lines the value of 0.

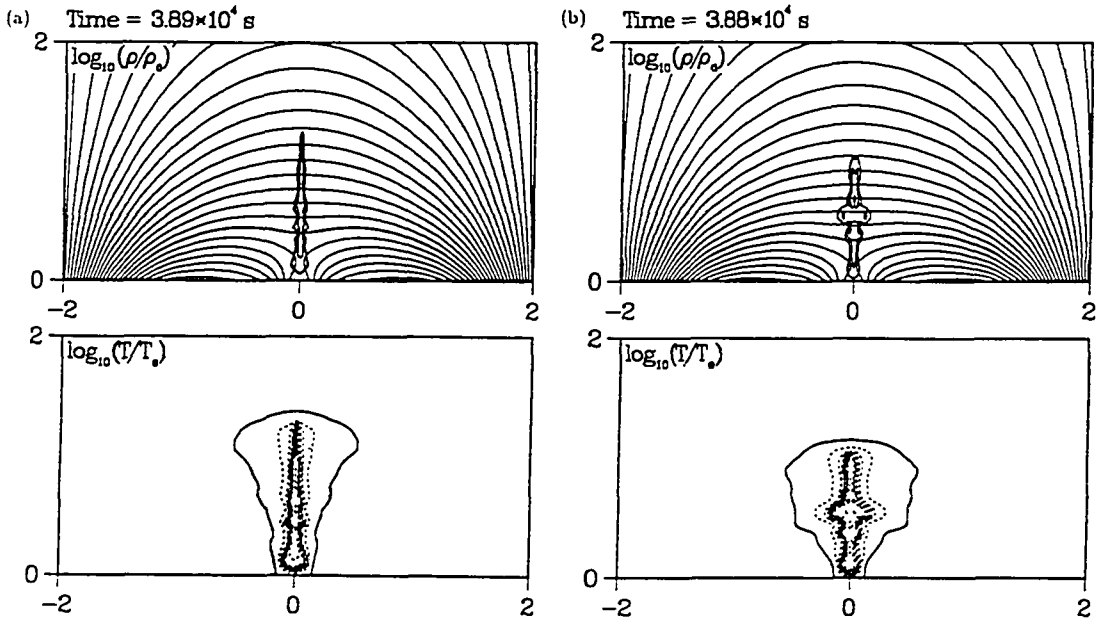

Figure 2.10 Pressure and temperature profiles for the prominences in (a) Cases 2Ca and (b) Case 2Cb. In the top panels, contours of $\log_{10}(\rho/\rho_0) \geq 0$ are superimposed on the magnetic field lines. At the bottom, contours of $\log_{10}(T/T_0)$ are shown for Case 2Ca at $t = 3.89 \times 10^4$ s and for Case 2Cb at $t = 3.88 \times 10^4$ s.

2.6 Summary and Discussion

In summary, we have demonstrated prominence formation in three different cases by numerical simulation. In Case 2A, the shear-induced expansion of a magnetic arcade is shown to lead to a thermal instability through adiabatic cooling and upward material transport by magnetic fields. In Case 2B, a converging motion combined with a shear is found to create a current layer and drive magnetic reconnection in a single arcade. The compression of material in the upper part of the island generates thermal instability. In Case 2C, a shearing or a converging motion near the neutral line can bring two arcades into contact to form a current sheet. The magnetic reconnection and plasma expansion give a perturbation in temperature and density above the X-point, which leads to a thermal instability. Formation of a prominence cavity is also observed in Case 2A and Case 2B.

The mechanism of prominence formation in Case 2A is restricted by the density and the plasma β. The condensation cannot be achieved within a reasonable time if the density at the coronal base is less than $10^9\,\mathrm{cm}^{-3}$. Also, a dip on field lines is hard to form if $\beta < 0.1$. But this β-restriction can be relaxed with increasing magnetic shear. This mechanism may thus be applied to low-lying filaments in active regions where the density is higher than in quiet regions. In this respect, it is noteworthy that normal polarity prominences are usually located lower than inverse polarity prominences (Leroy, 1989).

Mechanisms 2B and 2C are free from the β-restriction. Although the linear cooling time-scale indeed depends on the initial density, the magnetic reconnection can efficiently enhance the local density. Furthermore, the effect of heat conduction is minimized in Mechanism 2B. In the aspect of stability, the prominence in Case 2B seems to be most stable to the lateral perturbation. The high location of the prominence in Case 2B is consistent with the aforementioned statistics. This prominence model is thus close to the long-lived quiet region prominences.

The peculiar field geometry in Case 2C allows this mechanism to work with most diverse flow patterns. Due to the existence of an X-point, a weak field corridor is naturally realized, and a high shear angle of photospheric magnetic fields can be readily obtained with a small amount of footpoint shear. Our model prominences in Case 2C show an inverse polarity geometry and a modest height, which is consistent with observation (Leroy, private communication). It remains to be answered whether a magnetic island can be formed from this field geometry either by a secondary reconnection at a high altitude or by a multiple X-line reconnection (Lee and Fu, 1986) in a long current sheet. In this regard, Hirayama (1985) put forward a scenario, in which the sagging of field lines leads to magnetic reconnection above the prominence. The resulting field geometry is very interesting since it contains a diamagnetic "melon seed" (e.g., Hyder, 1967), whose stability is not much studied yet.

CHAPTER 3

Quasi-Static Evolution of Magnetic Arcades under Footpoint Shearing

3.1 Introduction

In the solar corona, the plasma β, the ratio of plasma pressure to magnetic pressure, is of the order of 10^{-2} or even smaller. The coronal dynamics is thus governed by magnetic fields. The coronal magnetic fields mostly behave passively responding to photospheric motions which shuffle around and collectively move footpoints of the magnetic fields. Any disturbance given to the magnetic fields at the photospheric level brings about a prompt deformation of coronal fields due to a short Alfvén transit time between two conjugate footpoints, which is typically of the order of a minute for the arclength $\sim 10^5\,\mathrm{km}$ and the Alfvén speed $\sim 10^3\,\mathrm{km\,s^{-1}}$. Compared to these numbers, collective photospheric motions have a far smaller speed $\sim 1\,\mathrm{km\,s^{-1}}$ and a long duration ($> 1\,\mathrm{day}$). It is thus justified to call the coronal evolution as being in a quasistatic equilibrium at every snapshot of time.

In the more than two decade old investigations of quasi-static evolution of solar magnetic fields, what has been questioned is whether there exists an instability, a loss of equilibrium (or global nonequilibrium) or a global singular nonequilibrium. Although there is no consensus in the definition of the last two terms, we will clarify the meaning of these mostly according to Aly (1994a). Assume that we continuously change a certain parameter which is determined by the outside world of the system, for example, a boundary condition. If there exists no equilibrium at all beyond a certain value of the external parameter, this catastrophic switchover is called a "loss of equilibrium." We can think of an example of loss of equilibrium in any dynamical system. The

word "global nonequilibrium (GNE)" is rather an MHD terminology describing this phenomena. We talk of a "global singular nonequilibrium (GSNE)" if the available equilibrium is suddenly no longer a smooth function in space and contains a tangential discontinuity (TD). This happens when no equilibrium can be found in the initial topology of field lines, but an equilibrium exists in a different field topology satisfying the same boundary condition and constraints. Then a part of field lines will collapse to form a current sheet, i.e., a TD. This spatially non-smooth equilibrium is also called a weak equilibrium. Applied to the solar situation, the loss of equilibrium, if any, may be related to an indefinite rising of the field structure conserving the topology towards opening up of field lines. The GSNE suddenly creates a current sheet of either finite length or infinite length. The latter case can also be involved in opening up of field lines. A weak equilibrium state can then be converted to a smooth equilibrium in a different topology with a sudden release of energy when a resistivity initiates magnetic reconnection.

A typical sequence of a solar eruptive process consists of rising of the cavity and formation of a CME loop, an erupting prominence, opening up of field lines, and magnetic reconnection occurring from near the solar surface upwards, which recovers the closed field configuration as before the eruption (e.g., Hundhausen, 1988). The above order is composed by conspicuous manifestations and is not necessarily the order of the onset times of individual events. The former three phenomena show up in the corona and constitute a coronal mass ejection (CME) in a narrow sense while the effects of reconnection appear in the chromosphere as well as in the corona and are associated with a flare. Most CMEs are accompanied by flares, but not all flares take place following CMEs.

The study of the quasistatic evolution of coronal magnetic fields has been focused on how the field lines open up. It was thus naturally questioned whether a sheared closed field configuration can have more energy than a fully open field configuration. Barnes and Sturrock (1972) numerically obtained force-free field solutions in an axisymmetric cylindrical geometry

and claimed that some of their solutions contained more energy than the fully open field satisfying the same boundary condition. On the contrary, Aly (1984) showed that, if the magnetic field decays sufficiently fast at infinity, then there exist an upper bound for the magnetic energy contained in force-free fields with the same normal magnetic field on the boundary. From this, he advanced the conjecture that the state of maximum energy is the corresponding open field configuration. This conjecture was later backed up by Aly (1991) and Sturrock (1991). In a numerical study, Yang *et al.* (1986) found that the energy of sheared fields of Barnes and Sturrock (1972) asymptotically approaches that of the open field with increasing shear and supported Aly's conjecture. On the other hand, Low (1986) proposed that magnetic fields in an axisymmetric spherical geometry may partially open up in response to certain footpoint shears. This argument was supported by Wolfson and Low (1992), who numerically obtained force-free fields in a closed configuration whose energy is greater than that of the corresponding partially open fields. Recently, Mikić and Linker (1994) used a zero β MHD code to simulate the evolution of a magnetic arcade in a zero β plasma in an axisymmetric spherical geometry and found that their quasi-force-free field tends to open up partially after a long enough shear is applied. Roumeliotis *et al.* (1994) also constructed force-free fields in an axisymmetric geometry and found that after a certain critical shear the field line expansion becomes a far more rapidly increasing function of shear than before. The recent study by Aly (1995) showed that the opening of axisymmetric field lines can take place either asymptotically at a fast rate or in a finite time.

Although real coronal magnetic fields are three-dimensional structures, two-dimensional approximations have been widely adopted, firstly because magnetic fields in a flaring region form an arcade-like structure along the polarity inversion line, and secondly because the outstanding observational indicator of energy buildup is a magnetic shear and/or a velocity shear along this line. The solar magnetic field can indeed be adequately described in the spherical coordinates, but

it is still worthwhile to study 2-D fields in the Cartesian coordinates. This is not merely because the Cartesian geometry is easier to handle but because the study of difference and similarity in two different geometries can also provide us with insights into the problem. As for 2-D force-free fields invariant in one coordinate (say z), Aly (1985) proved that the toroidal magnetic energy is bounded for any amount of shear and that, as the shear increases indefinitely, the force-free field asymptotically approaches an open field, in which all the current is concentrated in an infinitesimal current sheet. Recently, Aly (1994b) gave an example of the sequence of z-invariant force-free fields obtained by the generation function method.

In this chapter, we address the shear-induced evolution of z-invariant arcades using MHD simulation and the magnetofrictional method. The objectives of this study are to find (1) whether there exists a GSNE in the evolutionary sequence of a z-invariant arcade, and (2) how the current layer evolves into a singular current sheet. In section 3.2, an account is given for the formulation of the 2-D MHD equilibrium. In Section 3.3, a dynamic MHD code is employed to follow the evolution of a magnetic arcade with a slow footpoint motion in an isothermal low β plasma. Section 3.4 discusses MHD equilibria in a zero β plasma, i.e., force-free field configurations, which are obtained by a magnetofrictional method. Section 3.5 gives a brief summary and discussion.

In this place, we feel need to clarify our usage of the terms "current sheet" and "current layer" in this thesis. The word "current sheet" indicates a zero-width layer across which the tangential component of the magnetic field changes discontinuously. Thus the "current sheet" is the synonym of the "tangential discontinuity." On the other hand, the word "current layer" means a layer of finite width where a high but finite current density appears. Physically, this differentiation is meaningless when the width of a current layer becomes smaller than the order of the ion gyro-radius which is about 13 m with $T = 2 \times 10^6$ K and $B = 1$ G. A "current sheet" appearing in MHD may thus be interpreted as a sufficient condition to enter this kinetic regime.

Usually in MHD literature, a "current sheet" is considered as a sufficient condition for magnetic reconnection to take place with any nonzero resistivity. The distinction taken here is limited to this thesis. Oftentimes, both terms are used interchangeably although giving a little different nuances.

3.2 Formulation of 2-D MHD Equilibrium

The spatial domain concerned in this study is a halfspace $\{y > 0\}$ in a Cartesian coordinate system as shown in Figure 3.1. The x-z plane is taken to correspond to the photosphere. All the physical variables are assumed to depend on x and y only and to be invariant with respect to z. In this geometry, the magnetic field can be described by

$$\mathbf{B} = \hat{z} \times \nabla\psi + B_z\hat{z}, \tag{3.1}$$

where the flux function ψ is the negative of the z-component of the vector potential, i.e., $\psi = -A_z$, and ψ is constant along the individual field line. For simplicity, we assume the following symmetry without a significant loss of generality:

$$\psi(-x) = \psi(x),$$

$$V_z(-x) = -V_z(x),$$

where $V_z(x)$ is the speed of motion in the z-direction given in $\{y = 0\}$. We further assume that

$$B_y(x, y = 0) = \begin{cases} \geq 0 & \text{if } x < 0, \\ \leq 0 & \text{if } x > 0. \end{cases}$$

Thus the polarity inversion line lies at $x = 0, y = 0$ and ψ is at maximum here. For a given distribution $\psi(x, y = 0)$ in $\{y = 0\}$, the minimum energy state is the potential field if no constraints on the field topology are imposed. Starting with this potential field, we now impose

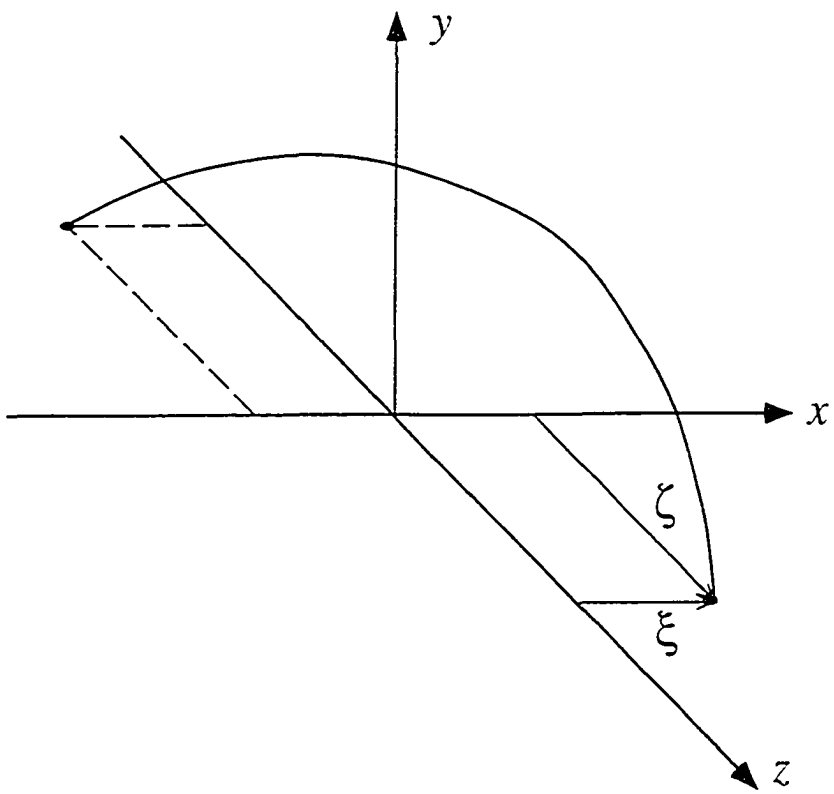

Figure 3.1 A sketch of a field line in our model arcade. The footpoint moving distance in z-direction from the corresponding potential field is denoted by ζ and the x-distance between the footpoint and the symmetry axis (here y-axis) is denoted by ξ.

a shearing motion $V_z(x,t) = v_z(x, y = 0, t)$ and define the moving distance of fluid elements as

$$\zeta(x,t) \equiv \int_0^t V_z(x,t')dt'. \tag{3.2}$$

On the other hand, half the distance in the z-direction between the two conjugate footpoints connected by a field line is given by

$$Z(\psi(x)) \equiv \frac{1}{2}(Z_{out} - Z_{in}) = \frac{1}{2}\int_\psi \frac{B_z}{|\nabla\psi|}ds_p, \tag{3.3}$$

where Z_{in} is the z-coordinate of the footpoint where the field line comes out of the boundary and Z_{out} is the z-coordinate of the other conjugate footpoint. The above integration is performed along the field line designated by ψ, and s_p is the arclength of the field line projected on the x-y plane. In a perfectly conducting plasma, it holds that

$$|\zeta(\psi)| = |Z(\psi)|.$$

Since the B_z flux through the surface surrounded by the field line ψ and the plane $\{y = 0\}$ is

$$\Phi_z(\psi) = \int_{\psi'=\psi}^{\psi'=\psi_o}\left(\int_{\psi'}\frac{B_z}{|\nabla\psi'|}ds_p\right)d\psi', \tag{3.4}$$

where $\psi_o = \psi(x = 0, y = 0)$, we can see that

$$2Z(\psi) = -\frac{d\Phi_z(\psi)}{d\psi}, \tag{3.5}$$

that is, the shear is nothing but the differential B_z flux between flux surfaces ψ and $\psi + d\psi$. Now we allow a nonzero resistivity pointwise only so that magnetic reconnection may take place in diffusion regions of infinitesimal size. In this point reconnection, it is expected that the distribution of toroidal flux and plasma mass is almost conserved, i.e., the toroidal flux between

ψ and $\psi + d\psi$ remains unchanged after the reconnection although there are now more than one flux surfaces named by ψ. In this case, it holds that

$$|\zeta(\psi)| = \left|\sum_i Z_i(\psi)\right|, \tag{3.6}$$

where

$$Z_i(\psi) = \frac{1}{2}\int_{\psi_i} \frac{B_z}{|\nabla\psi|} ds_p. \tag{3.7}$$

The subscript i here denotes an individual field line among those labeled by the same flux function. Assuming the bottom boundary to be rigid, i.e., $v_y(y = 0) = 0$, $\zeta(\psi)$ is conserved whatever motions arise in $\{y \geq 0\}$ as long as $v_z(y = 0) = 0$. The motion in z-direction in $\{y = 0\}$ can either create or remove the B_z flux depending on its direction.

In a perfectly conducting plasma above a rigid surface, mass in each flux tube is also conserved. If we further assume that there is no heat source or sink in the domain $\{y \geq 0\}$ and that no heat conduction is possible across the boundary $\{y = 0\}$, conserved is the entropy content in unit flux tube described by

$$S(\psi) = \int_{\psi} \frac{p^{\frac{1}{\gamma}}}{|\nabla\psi|} ds_p, \tag{3.8}$$

where γ is the adiabatic constant.

The exposition so far is regarding general 2-D magnetic fields. Now we consider the 2-D MHD equilibrium, which is described by

$$(\nabla \times \mathbf{B}) \times \mathbf{B} - \nabla p = 0. \tag{3.9}$$

From this, it can be shown that

$$\mathbf{B} \cdot \nabla p = 0 \quad \Rightarrow \quad p = p(\psi), \tag{3.10}$$

$$\mathbf{B} \cdot \nabla B_z = 0 \quad \Rightarrow \quad B_z = B_z(\psi), \tag{3.11}$$

$$\mathbf{B} \cdot \nabla J_z = 0 \qquad \Rightarrow \qquad J_z = J_z(\psi). \tag{3.12}$$

Rewriting Equation (3.9) in terms of ψ yields the so-called Grad-Shafranov equation

$$\nabla^2 \psi + \frac{d}{d\psi}\left(\frac{B_z^2}{2} + p\right) = 0. \tag{3.13}$$

Equation (3.9) or (3.13) can also be obtained from the variational principle extremizing the potential energy (e.g., Chodura and Schlüter, 1981; Low, 1978). A stable equilibrium is an energy minimum. The simplest type of this variational problem can be formulated specifying only the boundary flux distribution without any specification on B_z or p, and the solution is a potential field. In more specific formulations, one usually adds constraints on B_z and p and/or constraints on field line connectivity. The constraints on B_z and p are usually given either in the form of (3.11) and (3.10) or in the form of (3.3) and (3.8). Of course, the constraint on B_z and that on p may be of different types (e.g., Zwingmann, 1987). In the literature on solar physics (e.g., Aly, 1984), the problem with a constraint of (3.11) or (3.10) is often called the boundary value problem 1 (BVP1) and the problem with a constraint of (3.3) or (3.9) is called the boundary value problem 2 (BVP2). In the limit of vanishing p, the equilibrium configuration can be approximated by a force-free magnetic field

$$\nabla \times \mathbf{B} = \alpha \mathbf{B}, \tag{3.14}$$

and Equation (3.13) gives

$$\alpha = -\frac{dB_z}{d\psi}. \tag{3.15}$$

A BVP1 can be formulated by prescribing

$$\alpha(\psi) = \lambda f(\psi), \tag{3.16}$$

where λ is a nonnegative parameter and $f(\psi)$ is an arbitrary function of ψ. Aly (1984) formulated this BVP1 more generally in 3-D than we do here and showed that there exists a number λ_c such

that the problem has no solution decaying rapidly to zero at infinity if $\lambda > \lambda_c$. The BVP1 type constraint on B_z, however, is of little consequence in the evolutionary sequence of magnetic fields because it is not B_z but the footpoint displacement that is imposed by the external motions. On the BVP2 for force-free fields, where a shear is given as a constraint, Aly (1985) showed that there is an upper bound of the toroidal magnetic energy and that B_z goes to zero as the shear increases indefinitely. This suggests that the critical value of λ aforementioned cannot be exceeded for any amount of shear. The numerical studies by Klimchuk *et al.* (1988) and Klimchuk and Sturrock (1989) dealt with the BVP2 for force-free fields and found no loss of equilibrium nor any critical behaviour. In a numerical study, Zwingmann (1987) formulated a problem of the 2-D MHD equilibrium with a BVP1 type constraint on p and a BVP2 type constraint on the shear and found that the solution bifurcates beyond a certain value of $dp/d\psi$ while the increase of shear does not create any critical behaviour. This result, though interesting, can hardly be applied to the solar eruptive processes because in the solar corona the thermal energy is negligible compared to the magnetic energy. In the numerical study by Finn and Chen (1990), BVP2 type constraints are imposed on both p and shear, and it was reported that no bifurcation of the solution was found.

We now consider the implementation of the BVP2 type constraint on the shear, namely, the differential toroidal flux. Zwingmann (1987) and Klimchuk *et al.* (1988) expressed the magnetic field by Euler potentials as

$$\mathbf{B} = \nabla\alpha \times \nabla\beta. \tag{3.17}$$

and chose the form

$$\alpha = \alpha(x, y), \qquad \beta = z - \gamma(x, y). \tag{3.18}$$

It is clear that α and β are constant along field lines, and it can be shown that α is equivalent to

ψ. The z-distance between two conjugate footpoints is simply given by

$$\Delta z = z_2 - z_1 = \gamma_2 - \gamma_1. \tag{3.19}$$

The above description is thus a convenient way to prescribe a shear in an arcade-like geometry. However, it is not capable of describing a helical field configuration or a current sheet with a toroidal field component. For a helical field, Δz is not zero after one revolution of the field line, but $\gamma_2 - \gamma_1$ must be zero for the function $\gamma(x, y)$ to be single-valued. Thus the field lines in a magnetic island with a toroidal component cannot be described by Equation (3.18). In this regard, it is interesting that Zwingmann's (1987) upper branch solutions contain a magnetic island. Although it is not stated in his paper, the field lines in the island must have no toroidal component. Thus the O-line in his solutions is sustained by the plasma pressure gradient only, and he could not have found a bifurcation of the solution due to shear even if there were any. Aly (1990) asserted that, if a constraint on toroidal flux is imposed in the form of Equation (3.6) and no constraint on topology is given, there would be more than one nonlinearly stable solution of force-free field with different topologies beyond a critical value of shear. The minimum energy configuration would then contain one or more islands. The Euler potential description given by Equation (3.18) implicitly enforces a field topology without magnetic islands and is not competent to address Aly's argument.

In Section 3.4, we deal with force-free magnetic fields in a BVP2 type formulation. Since we do not yet have a numerical tool to find the solutions of all the possible topologies, we only investigate the existence of a weak equilibrium in an arcade-like topology. To be prepared for the case where a current sheet develops, the magnetic field is described by ψ and B_z.

3.3 Evolution of a Magnetic Arcade under Slow Footpoint Shearing: Dynamic Simulation

3.3.1 Description of Modelling

In this section, an MHD code is used to follow the evolution of the coronal magnetic fields more realistically than in the force-free field approximation taken in the next section. In our model, the corona is assumed to occupy the halfspace $y > 0$. All the physical variables are assumed to depend only on the horizontal coordinate x and the vertical coordinate y and to be invariant in the z-direction in the Cartesian coordinate system.

In this study, only motions in z-direction are imposed at the coronal base, and thus the magnetic flux profile at $y = 0$ is fixed in time as given by

$$\psi(x, y = 0, t) = \frac{8}{x^2 + 3}, \tag{3.20}$$

which can be generated by a dipole located at $x = 0, y = -\sqrt{3}$. With this boundary flux distribution, the maximum strength of the normal magnetic field ($|B_y|$) is located at $x = \pm 1$ and its value is 1. This unconventional normalization of a dipole flux profile facilitates comparing the numerical results directly with observation. The initial field is assumed to be potential as

$$\psi(x, y, t = 0) = \left(\frac{8}{\sqrt{3}}\right) \frac{y + \sqrt{3}}{x^2 + (y + \sqrt{3})^2}. \tag{3.21}$$

For simplicity, the coronal temperature is assumed to be constant in space and time. This isothermal assumption may be justified by a high thermal conductivity in the corona and is regarded to fit better to model the slow evolution of the corona than the common adiabatic assumption with $\gamma = 5/3$.

The governing equations for the simulation are a full set of ideal MHD equations including gravity as follows:

$$\frac{\partial \rho}{\partial t} + \nabla \cdot (\rho \mathbf{v}) = 0 \tag{3.22}$$

$$\rho(\frac{\partial \mathbf{v}}{\partial t} + \mathbf{v} \cdot \nabla \mathbf{v}) = \mathbf{J} \times \mathbf{B} - \nabla p + \rho \mathbf{g} + \nabla \cdot \mu \nabla \mathbf{v} \tag{3.23}$$

$$\begin{aligned} &\frac{\partial \psi}{\partial t} + \mathbf{v} \cdot \nabla \psi = \eta \nabla^2 \psi, \\ &B_x = -\frac{\partial \psi}{\partial y}, \qquad B_y = \frac{\partial \psi}{\partial x} \end{aligned} \tag{3.24}$$

$$\frac{\partial B_z}{\partial t} = \frac{\partial}{\partial x}(v_z B_x - v_x B_z) + \frac{\partial}{\partial y}(v_z B_y - v_y B_z) + \nabla \cdot (\eta \nabla B_z) \tag{3.25}$$

$$T = T_0, \qquad p = \rho R T \tag{3.26}$$

$$\mathbf{J} = \nabla \times \mathbf{B} \tag{3.27}$$

where all quantities are expressed in a nondimensionalized form by a proper normalization. The reference values of physical quantities are tabulated in Table 3.1.

As stated earlier, the magnetic field $\mathbf{B}$ is normalized by B_0 which is the maximum magnitude of B_y at the base and taken to be 50 G here. The length unit is the half distance between the B_y maxima and taken to be 3×10^4 km. The mass density ρ is referenced to the initial density ρ_0 at the base, which is obtained from the assumed proton number density at the base $n_0 = 1 \times 10^9\,\mathrm{cm}^{-3}$. The pressure p is normalized by $p_0 = B_0^2/(4\pi)$, the velocity $\mathbf{v}$ by $v_0 = B_0/(4\pi\rho_0)^{1/2}$, and the time t by $t_0 = L_0/v_0$. The temperature is set to 2×10^6 K. The gravity $\mathbf{g} = -g\hat{\mathbf{y}}$ is a function of y given by

$$g(y) = \frac{4\pi G M_\odot}{(R_\odot + y)^2} = g_0 \frac{{R_\odot}^2}{(R_\odot + y)^2} \tag{3.28}$$

where G is the gravitational constant, $M_\odot$ the solar mass, $R_\odot$ the solar radius and $g_0 = 2.74 \times 10^4\,\mathrm{cm\,s}^{-2}$ is the surface gravity. It is to be noted that without the gravity the plasma β would become too large in the upper part of the computational domain to describe the low

TABLE 3.1 Normalization Units and Symbols in Chapters 3 and 4

Quantity	Symbol	Unit	Value in CGS
Length	x	L_0	3.0×10^9
Magnetic Field	$\mathbf{B}$	B_0	50
Number Density	n	n_0	1.0×10^9
Mass Density	ρ	ρ_0	1.9×10^{-15}
Pressure	p	$p_0 = B_0^2/4\pi$	2.0×10^2
Temperature	T	T_0	2.0×10^6
Velocity	$\mathbf{v}$	$v_0 = B_0/(4\pi\rho_0)^{1/2}$	3.2×10^8
Time	t	$t_0 = L_0/v_0$	9.3
Energy	W	$W_0 = (B_0^2/4\pi)L_0^3$	5.4×10^{30}
Poynting Vector	$\mathbf{S}$	$S_0 = (B_0^2/4\pi)v_0$	6.4×10^{10}

3 corona. In our simulation, a constant kinematic viscosity $\nu = \mu/\rho$ is used for the purpose of numerical smoothing. The adopted value in units of $L_0 v_0$ is $\nu \approx 10^{-3}$, while in the solar corona the classical value (Spitzer, 1962) is $\nu \approx 3 \times 10^{-4}$ in the same units. The resistivity η in Equations (3.24) and (3.25) is set to zero to simulate an ideal MHD evolution.

Our computational domain consists of a rectangular area $\{(x, y) | 0 \leq x \leq 100,\ 0 \leq y \leq 150\}$ and this is twice as large in linear scale as the domain used in the simulation by Biskamp and Welter (1989). A nonuniform grid with 127×181 mesh points is employed, where the ratio of the smallest grid size to the largest in each direction is 1 to 40.

The boundary conditions at $x = 0$ are determined by the symmetry property. The other lateral boundary and the upper boundary are taken to be open and the zeroth order extrapolation

is used for $\rho^{n+1} - \rho^n$, where the superscripts denote the time step, and all the other variables except ψ. For the flux function ψ we impose the following boundary condition at these two open boundaries:

$$\frac{\partial \psi}{\partial t} = -(\mathbf{v}_n^* + \mathbf{v}_t) \cdot \nabla \psi, \tag{3.29}$$

where n and t respectively denote the normal and tangential components and

$$\mathbf{v}_n^* = \begin{cases} \mathbf{v}_n, & \text{if } \mathbf{v} \cdot \hat{\mathbf{n}} > 0; \\ 0, & \text{if } \mathbf{v} \cdot \hat{\mathbf{n}} \leq 0 \end{cases}$$

where $\hat{\mathbf{n}}$ is the outward normal unit vector.

At the bottom boundary, the shear velocity v_z is given by

$$v_z(x, y = 0, t) = f_z(t) V_z(x),$$

where

$$V_z(x) = V_{z0}\, x \exp\left(\frac{1}{2} - \frac{x^2}{2}\right) \tag{3.30}$$

and

$$f_z(t) = \begin{cases} \dfrac{t}{t_R}, & \text{if} \quad 0 \leq t < t_R; \\ 1, & \text{if} \quad t_R \leq t. \end{cases} \tag{3.31}$$

We have tried two values of V_{z0}, $0.001\, v_0$ and $0.01\, v_0$, and the results in both cases are almost identical as shown in the next subsection. The velocity is linearly increased from zero to its full value in $t_R = 50\, t_0$ to reduce the effect of the initial blast. The other two components of the velocity v_x and v_y are set to zero at the bottom boundary and the flux function ψ thus remains unchanged in time. The density ρ is set to be constant in time and equal to the initial value. Since this setting is an overspecification of the boundary condition, an unresolvable boundary layer appears at the bottom boundary. However, the effect of this boundary layer to the overall computation is minimal due to the low plasma β ($\sim 2.5 \times 10^{-3}$ at the origin). In the present computation, all the variables are defined at the meshpoints, but the fluxes are defined

between two adjacent meshpoints. This allows a nonzero mass flux between the first and second meshpoints from the bottom boundary even though $v_y = 0$ at this boundary. Thus this diffusion flux makes the coronal base act as a density reservoir, and it rather helps keep the time-step size from getting too small due to the rarefaction of plasma. The toroidal field B_z at the bottom boundary is obtained by placing a half-size cell contiguous to the boundary.

The governing equations are finite-differenced and integrated in time using the semi-implicit scheme (Harned and Schnack, 1986), which allows a time-step to be 4-10 times as large as the CFL time-step. For the numerical algorithm, readers are referred to Appendix A.

3.3.2 Numerical Results

At the bottom boundary, the shearing speed $|v_z|$ and the normal component of the magnetic field $|B_y|$ both have their maximum at $x = \pm 1$ as prescribed by Equations (3.20) and (3.30). The maximum shear is from now on designated ζ_m, which is

$$\zeta_m(t) = V_{z0} \int_0^t f_z(t')dt'. \tag{3.32}$$

We have tried two shearing speeds $V_{z0} = 10^{-3}\, v_0$ and $10^{-2}\, v_0$ and the two cases do not show any notable difference in field configurations with respect to the same shear. This point will be discussed later. The reported case is obtained with $V_{z0} = 10^{-3}\, v_0$ unless stated otherwise. It should be also noted that the shear given by Equation (3.30) produces currents in the negative z-direction over the whole domain. The current direction may depend on the different shear profile used, but it is always negative in the outer part of the arcade as long as the shear vanishes for $x \to \pm\infty$. When we speak of "current density" hereafter, it will mean $|J_z|$ unless otherwise noted. Thus a "current density maximum" will imply a "J_z minimum" in the strict sense.

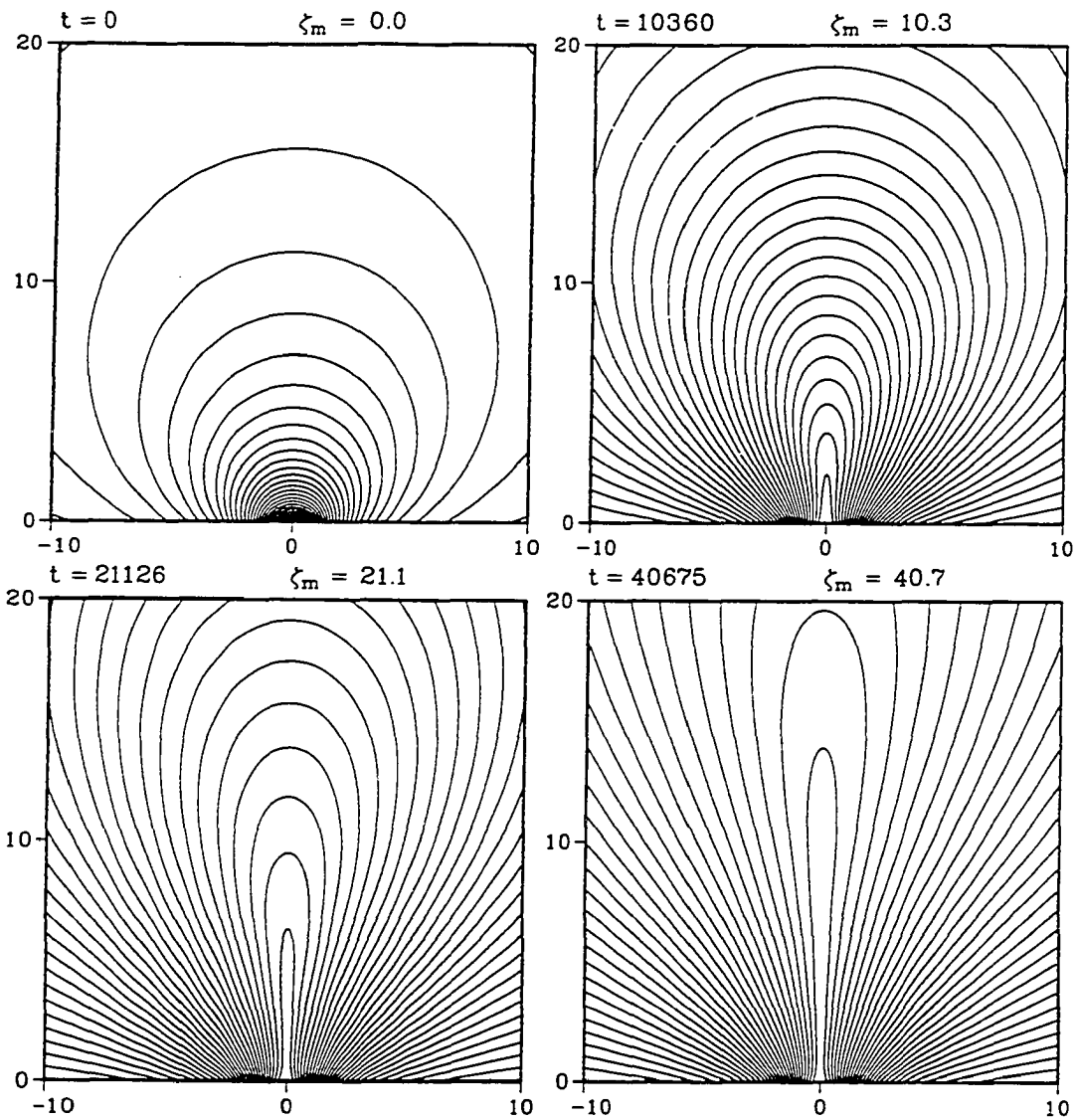

Figure 3.2 Evolution of a magnetic arcade subject to a shearing motion of $V_{z0} = 10^{-3} v_0$. The time and shear above each panel are referenced to normalization units given in Table 3.1.

In the case with $V_{z0} = 10^{-3}\, v_0$, we have continued to increase the shear up to $\zeta_m \approx 50$, which corresponds to about one third of the circumference of the solar sphere. In terms of the shear angle defined by

$$\theta_s = \arctan\left(\frac{d\zeta}{dx}\right)_{x=0} \tag{3.33}$$

the above shear is translated as $\theta_s = \arctan(e^{1/2}\zeta_m) = 89.6°$. In the case with $V_{z0} = 10^{-2}\, v_0$, the maximum shear reaches $\zeta_m \approx 100$ and yet even in the later stage no particular deviation is found from the evolutionary characteristics in the other case. The evolution of the field configuration is shown in Figure 3.2. A current layer becomes noticeable after $\zeta_m \sim 7$ in the central part of the arcade and grows in height with increasing shear. The current density in the current layer keeps increasing (see Figure 3.6(c)). In the initial potential field, the curvature vectors of all the field lines are directed inward, which is also true for field configurations with small shears. For $\zeta_m \gtrsim 7$, the inner field lines are more stretched vertically and pinched laterally in some parts where the curvature vector is directed outward. In the y-axis, the $|J_z|$ maximum is located near the concave parts of field lines. In Figure 3.3, the y-coordinates of field line apices are shown against the flux functions labeling field lines. In the initial phase of evolution for $\zeta_m \lesssim 2$, the expansion is confined to the inner part of the arcade. The ψ-y curve has no point of inflection for $\zeta_m = 0$, but shows two points of inflection for shears $\zeta_m \gtrsim 2$. The lower point of inflection is the B_x minimum and related to the current density maximum for a large shear. The minimum B_x is decreased with increasing shear, but is never zero. The plateau around the B_x minimum corresponds to a current layer, whose length is increased with shear.

In Figure 3.4, the total and partial magnetic energies per unit length in z are plotted in units of the energy of the potential field ($\sim 1.4 W_0$) against shear. For a small shear ($\zeta_m \lesssim 2$), the increase in the toroidal magnetic energy (thin solid line), $W_z = \int (B_z^2/2) dV$, exceeds the increase in the poloidal magnetic energy (chain-dotted line), but W_z ceases to increase around

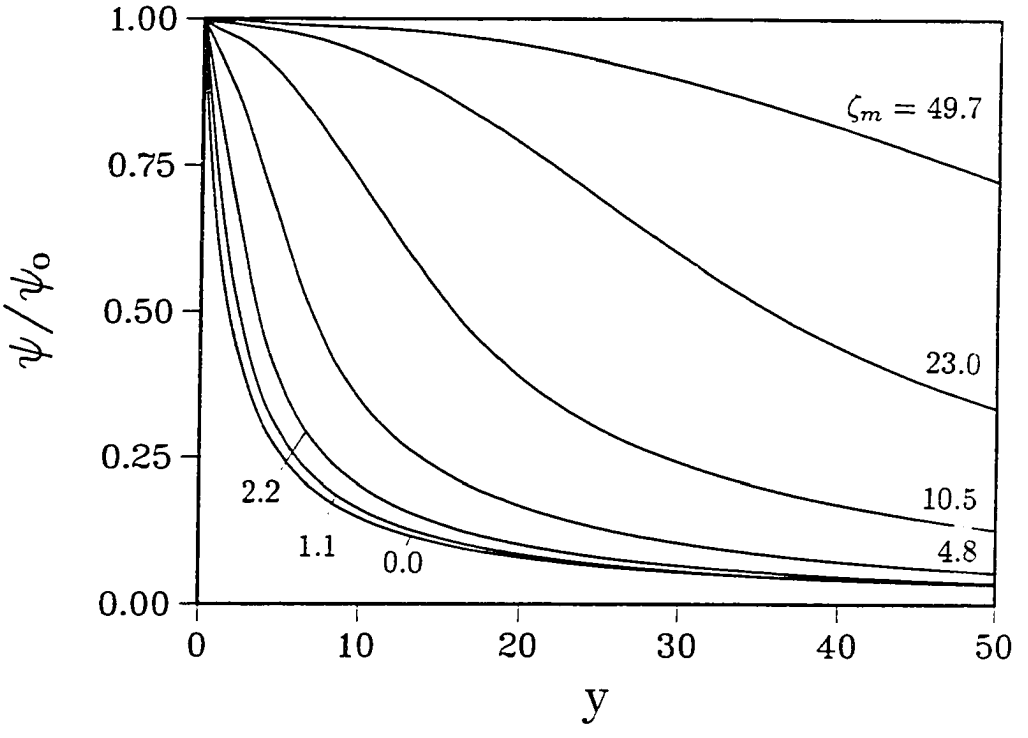

Figure 3.3 Flux function (ψ) versus the height of field line apices for seven different shears.

$\zeta_m \approx 7.3$ and keeps retaining 93 % of the potential field energy. After that, the total energy (thick solid line) continues to increase probably indefinitely. It can be readily noticed that two partial poloidal energies $W_y = \int (B_y^2/2)\, dV$ (dashed line) and $W_x = \int (B_z^2/2)\, dV$ (dotted line) have just as much a difference as the toroidal magnetic energy, i.e.,

$$W_y = W_x + W_z \,. \tag{3.34}$$

This relation was obtained by Aly (1984) for general force-free fields using the tensor virial theorem.

In Figure 3.4, it catches our attention that W_x decreases up to $\zeta_m \approx 2$ and then starts to increase. This is suggestive of two different phases in the arcade evolution. In the potential field, $|B_x|$ is maximum at the origin. When a shear begins to be applied to the potential field, the field lines near the origin are slightly lifted and B_x is mostly decreased there resulting in decrease of W_x. Beyond a certain amount of shear, outer field lines expand more rapidly and $|B_x|$ increases near footpoints of the expanding outer field lines. This argument can be supported by Figure 3.5, where the current density, $-J_z$, at $y = 0.091$ is plotted against x. Note that the current density can only be calculated at the grid points inside the boundary and that the first row of grid points just above the bottom boundary is located at $y = 0.091$. For $\zeta_m = 1.0$ and 1.9, the current density maximum is located at $x = 0$, which implys that the decrease in B_x is most serious in the inner field lines. From $\zeta_m = 2.9$ on in the figure, the current density maxima are located at a little distance from $x = 0$. As the shear increases, the maximum current density grows and the current peaks become sharper. As shown in Figure 3.5(b), the distance between a current density maximum and the y-axis becomes smaller with increasing shear. If the flux function corresponding to the current density maximum is denoted by $\psi_c(\zeta_m)$, then our result

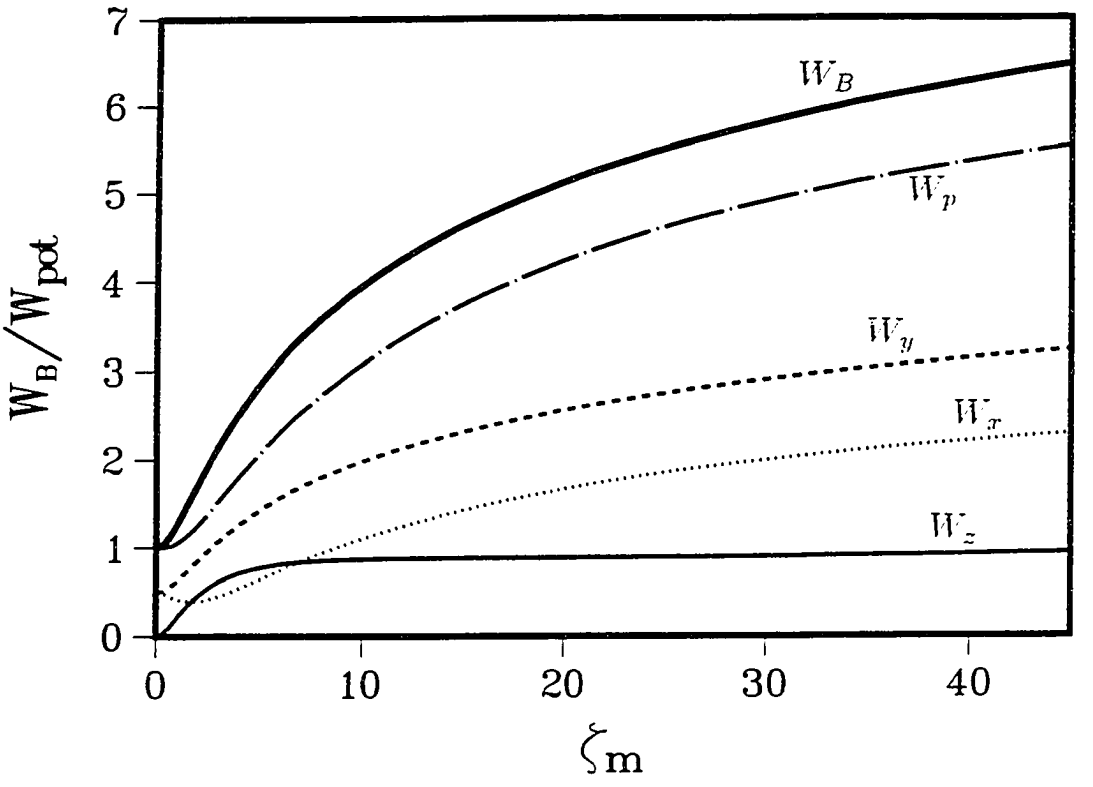

Figure 3.4 Magnetic energy in units of the potential field energy against shear. The thin solid line represents the toroidal magnetic energy, $W_z = \int (B_z^2/2) dV$, the dotted line $W_x = \int (B_x^2/2) dV$, the dashed line $W_y = \int (B_y^2/2) dV$, the chain-dotted line the poloidal magnetic energy, $W_p = W_x + W_y$, and the thick solid line the total magnetic energy.

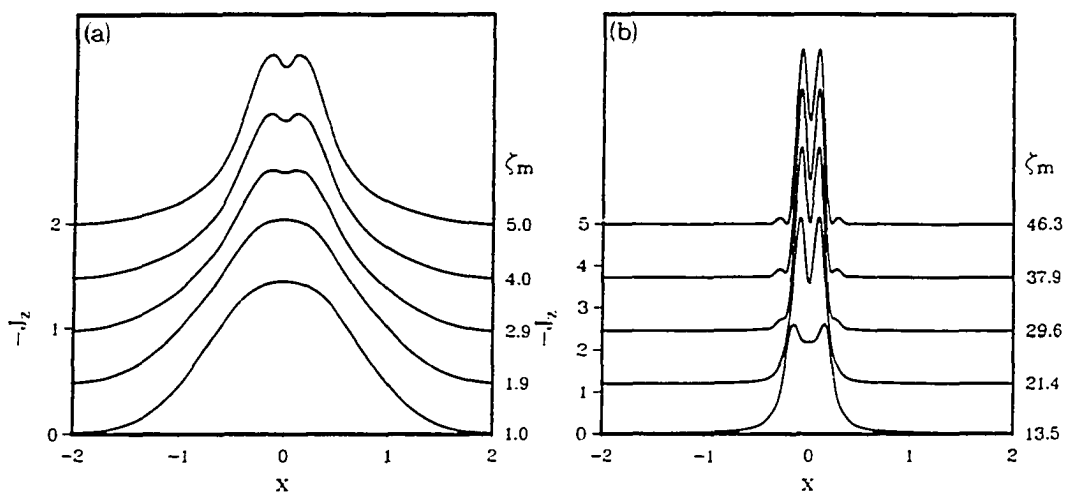

Figure 3.5 Current density $(-J_z)$ at $y = 0.091$ versus x. (a) Five cases in the early evolutionary stage; (b) five cases in the later stage. Note that the zero point of each curve is the bottom of the label characters. Small ripple structures in (b) are dynamical effects which are not found in static solutions in the next section.

tells the asymptotic behaviour

$$\lim_{\zeta_m \to \infty} \psi_c = \psi_o, \tag{3.35}$$

where $\psi_o = \psi(x = 0, y = 0)$.

The effects of different shearing speeds are illustrated in Figure 3.6. The tiny difference between two cases tells that a quasi-static evolution is well approximated by our dynamic simulation. What is shown in the second panel is the integral of the y-component of Poynting vector, i.e., the energy input rate generated by the shearing motion:

$$\frac{1}{2}P_y = \int_0^{L_x} S_y dx = -\int_0^{L_x} B_y(\mathbf{v}\cdot\mathbf{B}), \tag{3.36}$$

where the integration is performed at $y = 0$. In the figure, this quantity is divided by V_{z0} to compare cases with different shearing speeds. Since the shearing speed is constant after $t = 50\,t_0$, the variation of the energy input rate wholly depends on B_z. It is evident from the figure that there are two different evolutionary phases. Up to $\zeta_m \approx 1.8$, the energy input rate increases and after that it decreases. Although $B_z(\psi)$ depends on ζ_m, it implies that B_z increases and the arcade expansion is mild in the first phase while B_z decreases and the expansion is rapid in the second phase. As the shear increases indefinitely, B_z and the energy input rate asymptotically go to zero. The barely noticeable difference between two cases with different shearing speeds is that both the energy and the energy input rate is higher in the case with $V_{z0} = 10^{-2}\,v_0$ (dashed line) than the case with $V_{z0} = 10^{-3}\,v_0$ (solid line). This can be attributed to the fact that the higher the shearing speed is, the farther the whole configuration is away from the equilibrium. The faster motion of footpoints will drag the field lines more and create larger B_z near the footpoints than the slower motion; hence the larger energy input rate. The third panel shows the maximum value of $|J_z|$ obtained at all inside grid points. Since $J_z = -B_z(dB_z/d\psi)$ in equilibrium, the initial shooting up of $|J_z|_{max}$ up to $\zeta_m \approx 1.4$ indicates

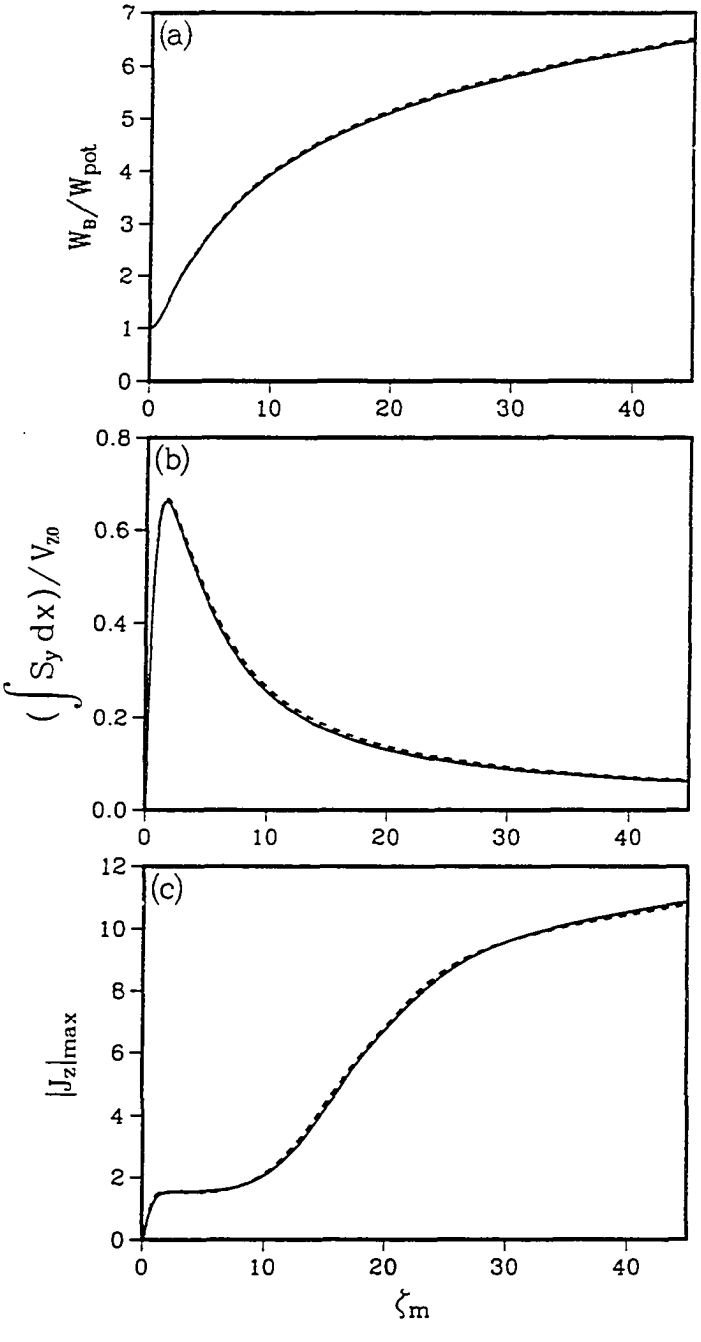

Figure 3.6 Evolution of (a) magnetic energy in units of the potential field energy, (b) Poynting flux through the bottom boundary ($x \geq 0$, $y = 0$) per unit length in z, and (c) the maximum of $|J_z|$. The solid line stands for the case with $V_{z0} = 10^{-3}\, v_0$ and the dashed line for the case with $V_{z0} = 10^{-2}\, v_0$.

that a rapid increase of B_z raises a slope of B_z from the origin outward, which is possible due to the mild distension of the arcade. After that, the $|J_z|_{max}$ curve is flattened, which implies a more or less self-similar expansion. Beyond $\zeta_m \approx 7$, $|J_z|_{max}$ starts to increase again, which is not due to the overall increase of the slope in the $B_z(\psi)$ curve, but due to the generation of a large slope only around a certain ψ. In this stage, a current layer becomes more and more noticeable and extended vertically with some part of pinched field lines as mentioned earlier. We are naturally led to suspect possibility of magnetic reconnection in this phase. The study in the next chapter shows that this expectation turns out true.

In a dynamic numerical simulation, small perturbations are always present and if the system is unstable, an instability quickly develops. An example of the ideal MHD instability is provided by the simulation by Mikić *et al.* (1988), where the symmetry-breaking perturbations brought about by round-up errors are amplified so that one arcade is pinched by the neighboring arcades. As for a single arcade, no simulation studies have found an ideal MHD instability developed by footpoint shearing (Biskamp and Welter, 1989; Steinolfson, 1991; Mikić and Linker, 1994). The arcade simulated here is stable up to $\zeta_m \approx 100$ and it seems to be so even when the shear increases to infinity. A current layer is located around $\psi_c < \psi_o$ and it asymptotically approaches a singular current sheet of an open field. With the shear profile given by Equation (3.30), no partial opening of the field is expected for any amount of shear, but if we consider a finite extension of the observation area, the observed field may look like a partially open field for a very large shear. Further discussions on our results are given in Section 3.5.

3.4 Two-Dimensional Sheared Force-Free Fields: Static Solutions

In this section, 2-D force-free field solutions are presented, which are obtained by the magnetofrictional method. The main objectives in this section are to compare the dynamic

solutions obtained above with force-free solutions to examine the quasi-static nature and to investigate the fine structures of current layers with such a high resolution that can hardly be achieved in dynamic simulations.

3.4.1 Description of Modelling

Historically, two numerical methods have been mostly used to study force-free fields; one is the magnetofrictional method (Yang *et al.*, 1986; Klimchuk *et al.*, 1988) and the other is the so-called zero β dynamic simulation (Mikić *et al.*, 1988; Biskamp and Welter, 1989; Mikić and Linker, 1994). The latter is not to find exact solutions of force-free fields, but to follow the evolution of force-free fields approximately. In the zero-beta formulation, the pressure term is ignored while the inertia comes in by an arbitrarily prescribed density distribution. Neither momentum nor energy is conserved here although the kinetic energy is negligible compared to the magnetic energy in a quasi-static evolution of a low β plasma. The solutions obtained by a zero β code is thus not as realistic as those obtained by a conventional MHD code, nor do they represent force-free fields as exactly as those obtained by other methods of finding static equilibria.

The magnetofrictional method was devised to find a stable magnetohydrostatic equilibrium with given boundary conditions under the perfect conductivity constraint. Let us imagine a system which is not in equilibrium under certain boundary conditions and constraints. The excessive potential energy will then generate a force, which will drive the system towards the state of minimum energy. If the total energy is conserved, the system cannot settle down in an equilibrium but passes it by since the kinetic energy will be maximum when the potential energy is minimum. If the whole or a part of the kinetic energy is artificially removed out of the system during its evolution, the system can settle down in the minimum energy state, i.e., a

stable equilibrium, at least asymptotically. The loss of the kinetic energy may be likened to the frictional dissipation in a mechanical system; hence the term "magnetofrictional method."

If the magnetic field is expressed by $\mathbf{B}$ or $\mathbf{A}$, the initial configuration must satisfy all the boundary conditions and constraints which specify the solution. As mentioned in Section 3.2, the Euler potential description given by Equation (3.18) enforces a specific field topology. This can be an advantage as long as a smooth equilibrium solution is guaranteed to exist in that topology since we have more freedom in choosing the initial configuration. However, it cannot be employed if the purpose is to investigate the existence of a singular solution or to find the minimum energy state under a relaxed constraint on field topology with pointwise reconnection allowed. We thus use ψ and B_z to describe the magnetic field.

The governing equations in the magnetofrictional method are:

$$\mathbf{v} = \alpha\, \mathbf{J} \times \mathbf{B}, \tag{3.37}$$

$$\frac{\partial \psi}{\partial t} = -\mathbf{v} \cdot \nabla \psi, \tag{3.38}$$

$$\frac{\partial B_z}{\partial t} = \frac{\partial}{\partial x}(v_z B_x - v_x B_z) + \frac{\partial}{\partial y}(v_z B_y - v_y B_z), \tag{3.39}$$

where α is a positive number and function of space and time, whose magnitude is limited by the numerical stability condition. It is to be mentioned that the momentum equation is reduced to to the form of Equation (3.37) by resetting the velocity to zero after each time-step, not due to the fact that ρ and p are negligible in a low β plasma as stated by Yang *et al.* (1986). Equation (3.37) is usable regardless of plasma β (see Lee *et al.* (1995) for application to the Earth's magnetosphere). While the MHD equations constitute a hyperbolic system, the equations in the frictional MHD form a parabolic system. The solution sequence of this system converges to the solution of the equilibrium equation (Equation (3.9) or (3.13)) that is elliptic.

As far as a 2-D MHD equilibrium is concerned, the toroidal magnetic field pressure $p_z = B_z^2/2$ plays the same role as the plasma pressure as can be seen in Equation (3.13). This allows an alternative expression of 2-D force-free fields as

$$(\nabla \times \mathbf{B_p}) \times \mathbf{B_p} - \nabla p_z = 0, \tag{3.40}$$

where $\mathbf{B_p} = B_x\hat{\mathbf{x}} + B_y\hat{\mathbf{y}}$ is the poloidal field. The toroidal field is now treated as if it were a gas with $\gamma = 2$, and the governing equations are:

$$\mathbf{v} = \alpha\,(\mathbf{J_z} \times \mathbf{B_p} - \nabla p_z)\,, \tag{3.41}$$

$$\frac{\partial \psi}{\partial t} = -\mathbf{v} \cdot \nabla \psi = 0\,, \tag{3.42}$$

$$\frac{\partial h}{\partial t} = -\nabla \cdot (h\mathbf{v})\,, \tag{3.43}$$

where

$$h \equiv (2p_z)^{\frac{1}{2}} = B_z \tag{3.44}$$

and $\mathbf{v}$ in Equations (3.41)–(3.43) has x- and y-components only. With this formulation, one can save about one third as much computation time as is needed with the earlier formulation.

As the initial configuration, the potential field given by Equation (3.21) is adopted. With this choice, some field lines inevitably touch the top and lateral boundaries of the finite computational domain. Thus we also tried a potential field obtained numerically in the computational domain setting

$$\psi(x = L_x) = \psi(y = L_y) = \psi(x = L_x, y = 0),$$

where L_x and L_y are respectively the x- and y-size of the computational domain, so that no field lines may cross those boundaries. The results obtained from the two initial conditions have

shown no visible difference. The employed shear profile is the same as in the previous section, i.e.,

$$\zeta(x) = \zeta_m \, x \exp\left(\frac{1}{2} - \frac{x^2}{2}\right). \tag{3.45}$$

Now we assign a toroidal field B_z to each field line in such a way that

$$|\zeta(\psi)| = \frac{1}{2} B_z(\psi) \left|\frac{d\Sigma}{d\psi}\right|, \tag{3.46}$$

where $d\Sigma/d\psi$ is the differential flux volume (more exactly area in 2-D) defined as

$$\frac{d\Sigma}{d\psi} = -\int_{\psi} \frac{ds_p}{|\nabla\psi|}. \tag{3.47}$$

The minus sign comes from the definition of Σ as the area of the surface in the poloidal plane surrounded by field line ψ and the bottom boundary. For our initial configuration (Equation (3.21)), the differential flux volume can be analytically obtained and

$$\left|\frac{d\Sigma}{d\psi}\right| = \frac{64}{3\psi^3}\left[\sqrt{\frac{3}{8}\psi\left(1 - \frac{3}{8}\psi\right)} + \arcsin\sqrt{1 - \frac{3}{8}\psi}\right]. \tag{3.48}$$

It should be noted that

$$\left|\frac{d\Sigma}{d\psi}\right|(x = 0, y = 0) = 0.$$

Thus we cannot use Equation (3.46), but can exploit the following relation to assign B_z to the origin:

$$\frac{d\zeta}{dx} = \frac{B_z}{B_x}. \tag{3.49}$$

For an arbitrary field configuration, the differential flux volume cannot be obtained analytically and a numerical evaluation is required. We have compared the numerical value of $|d\Sigma/d\psi|$ with the analytical value for several field configurations and found that the differences are within a few percent in our numerical setup.

The computational domain is a rectangular area $\{(x,y)|\, 0 \leq x \leq 200,\ 0 \leq y \leq 400\}$ and is covered with a nonuniform grid with 181×301 mesh points, where the ratio of the smallest grid size to the largest in each direction is 1 to 200. In one case, the results obtained in the above domain are mapped to a smaller domain ($L_x = 50, L_y = 100$) with a finer grid and further relaxed in order to reveal the structure of the inner region of the arcade. The smallest grid size in the finer grid is 1.5×10^{-2}, which is about one third of the smallest grid size in the coarser grid.

The magnetofrictional method in itself prescribes the allowable boundary condition:

$$\mathbf{v} = 0,$$

$$\frac{\partial B_n}{\partial t} = 0 \qquad \text{or} \qquad \frac{\partial \psi}{\partial t} = 0,$$

so that any globally conserved quantities as well as magnetic fluxes remain invariant.

In this calculation, only the final solution is meaningful and we can use the maximum allowable time-step at each grid point. The time-integration is done using a modified semi-implicit scheme. The frozen-in condition is slightly violated due to the implicit diffusion inherent in the numerical scheme although the total magnetic flux is exactly conserved. The deviation of the shear from the prescribed value is found to be less than 5 % at the end of relaxation.

To end the relaxation procedure, the following criteria are adopted:

$$\frac{W^{n-1} - W^n}{W^n} < 6 \times 10^{-7}, \tag{3.50}$$

$$W^n / W^0 < 10^{-14}, \tag{3.51}$$

$$\frac{F^{n-1} - F^n}{F^n} < 5 \times 10^{-3}, \tag{3.52}$$

$$F^n / F^0 < 10^{-11}, \tag{3.53}$$

where W is the total magnetic energy and $F = \int (\mathbf{f} \cdot \mathbf{f}) dV$ the volume integral of force squared and the superscript denotes the relaxation step number.

3.4.2 Numerical Results

The force-free field solutions obtained by the magnetofrictional method are found to be quite similar to the field configurations obtained by the dynamic simulation in the previous section. Figure 3.7 shows the equilibrium configurations for $\zeta_m = 8$ and $\zeta_m = 40$. Comparing Figure 3.7 with Figure 3.2, it can be noticed that the central field line for $\zeta_m = 40.0$ in the former is taller than that for $\zeta_m = 40.7$ in the latter. In our dynamic simulation, the arcade expansion is retarded partly by gravity and partly by the finite propagation speed of waves. We have obtained force-free field solutions up to $\zeta_m = 80$ and found no weak equilibrium nor any other singular behaviour as in the previous section.

Since the finest grid size used in the force-free field calculation is about one sixth of that used in the dynamic simulation, we can illuminate the fine structure of the central current layer, which is shown in Figure 3.8. The good agreement of the field lines and the B_z contours speaks for the accuracy of our numerical solutions. The contours of J_z do not match so well with field lines as the contours of B_z, which is attributed to the fact that J_z is not a primary variable in our calculation, but a derived quantity. The highly stretched field lines running parallel to the y-axis lead us to suspect the current layer to be a tangential discontinuity. However, it is found that B_x along the y-axis is not zero and roughly constant in $0.9 < y < 3$.

The most remarkable feature in Figure 3.8 is that the field lines in the current layer are bent near the footpoints. In relation to current sheets in force-free fields, Low and Wolfson (1988) reasoned that the separatrix field line threads the base horizontally. For force balance in

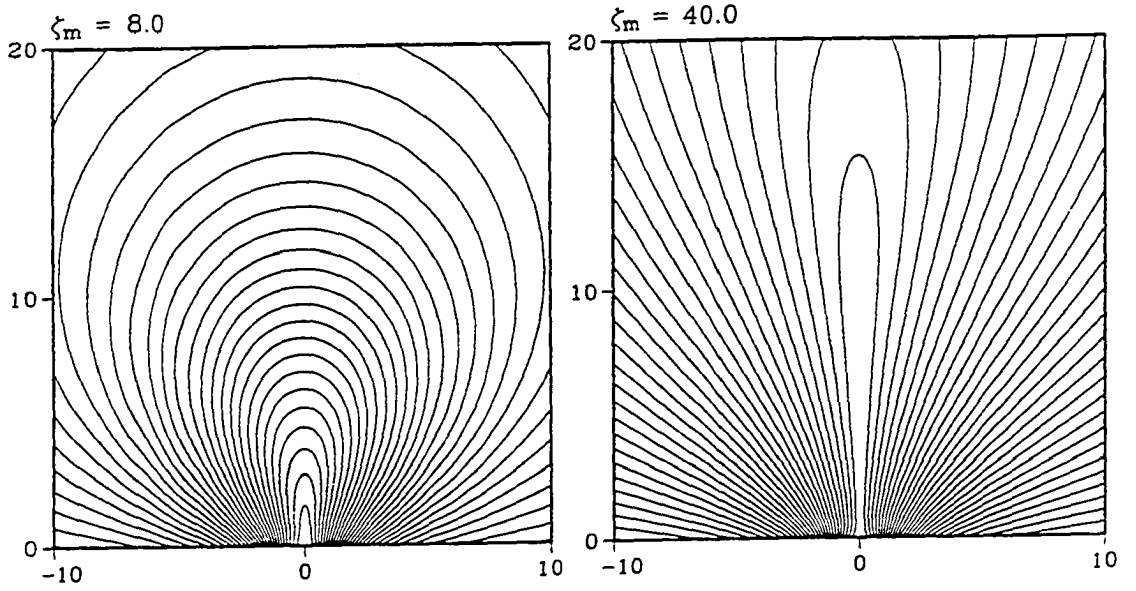

Figure 3.7 Magnetic field configurations for force-free fields obtained by the magnetofrictional method.

a tangential discontinuity, the total pressure must be continuous across the separatrix field line, i.e.,

$$\left[p + \frac{B_p^2}{2} + \frac{B_z^2}{2}\right] = 0, \tag{3.54}$$

where the square bracket denotes the difference between the values on the two sides of the discontinuity. In a force-free field, if $B_y(x)$ is continuous at the bottom boundary, the only way to compensate for the jump in $|B_z|$ at the footpoint is to make $|B_x|$ infinite so that the two infinite values have a finite difference. The field line thus runs horizontally at the footpoint and above the base it bulges out towards the weaker side of $|B_z|$ (Vekstein and Priest, 1992). Although our current layer is not singular, the stronger toroidal magnetic pressure ($B_z^2/2$) tends to expand its domain into the weaker side creating so highly bent field lines that the magnetic tension force can balance the toroidal magnetic pressure force.

As seen in the previous section, the current layer is centered on a certain flux function $\psi_c < \psi_o$. To find the asymptotic behaviour of the current layer, the x-coordinate of the current density maximum at the bottom boundary is plotted against five different shears along with the range over which current density is more than half the maximum value (Figure 3.9). As the shear increases, the footpoint of the current layer approaches the origin and the width of the current layer becomes smaller. Though not shown in the figure, the vertical length of the current layer is increased with shear. It can be thus inferred that the central current layer in a z-invariant magnetic arcade asymptotically turns into a current sheet of an infinite length located at the origin as the shear increases to infinity.

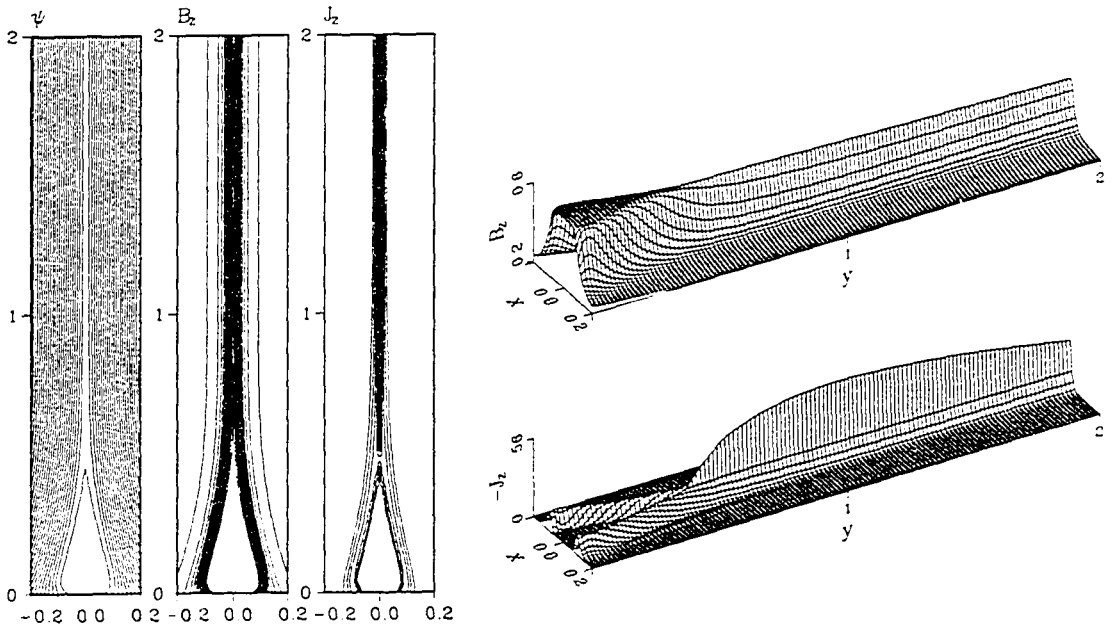

Figure 3.8 Magnified view of the lower part of the current layer for $\zeta_m = 40$. Field lines, contours of B_z and J_z, and surface plots of B_z and $-J_z$ are shown.

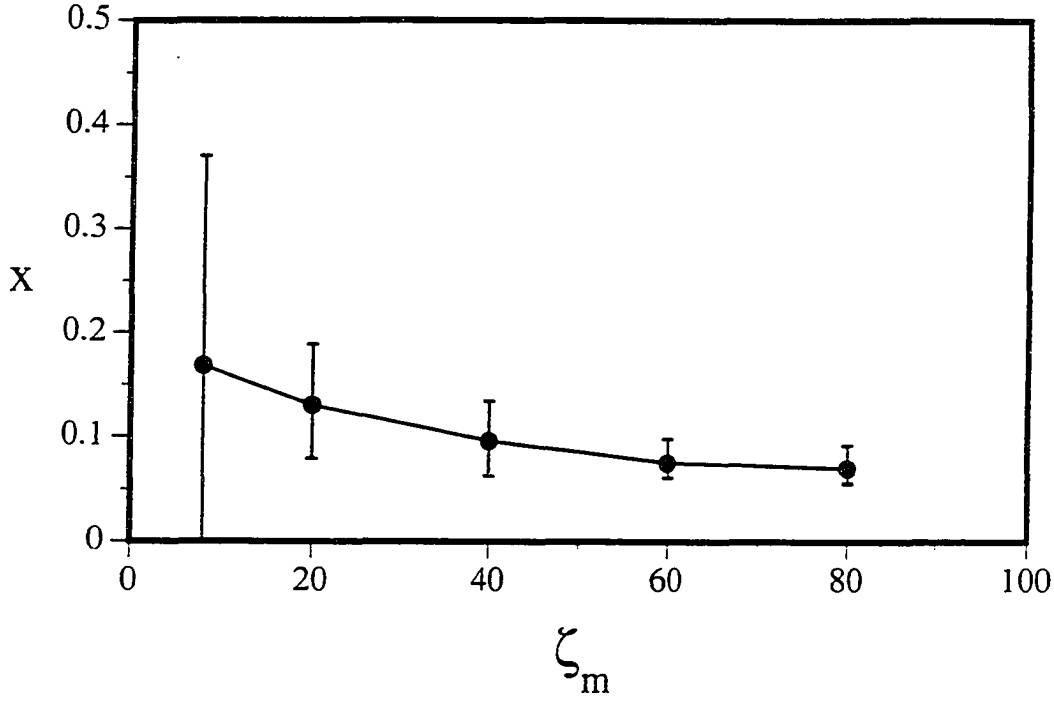

Figure 3.9 The x-coordinate of the current density maximum at the bottom boundary versus shear. The vertical bars are extended to the points where the current density is half the maximum.

3.5 Discussions and Summary

In this chapter, we have investigated the quasi-static evolution of a 2-D magnetic arcade in a Cartesian geometry using an MHD simulation and the magnetofrictional method. The results obtained by both methods have shown a good agreement and can be summarized as follows.

(1) The quasi-static evolution in a low β plasma is found stable up to $\zeta_m \sim 100$ and is expected to be so for any amount of shear.

(2) There is no nonequilibrium found whether it is GNE or GSNE.

(3) The evolutionary sequence is composed of three distinct phases. In the first phase ($\zeta_m \lesssim 1.8$), the overall arcade expansion is very mild and inner field lines are most lifted. However, the growth rates of B_z, W_z and $|J_z|$ are the highest of all three phases. In the second phase ($1.8 \lesssim \zeta_m \lesssim 7$), the arcade expansion is more or less self-similar and there is little variation in $|J_z|_{max}$. The toroidal field B_z starts to decrease and the increase of W_z is decelerated. In the third phase ($\zeta_m \gtrsim 7$), the most remarkable feature is the formation of a central current layer, where $|J_z|$ keeps increasing. The arcade expansion is the fastest and W_z is kept constant while B_z asymptotically goes to zero.

(4) In the ψ-space, the current layer is located around a certain $\psi_c < \psi_o$ with a finite width $\delta\psi$. As the shear increases, ψ_c approaches ψ_o and $\delta\psi$ becomes smaller. The length of the current sheet is found to be an increasing function of shear. From our results, an open field is an asymptotic state in a z-invariant arcade.

It is to be mentioned that many of the above results are consistent with the assertions by Aly (1990) regarding force-free magnetic fields, which can be summarized as follows.

(1) There exists a nonlinearly stable solution for any amount of shear.

(2) In the initial phase of evolution, the arcade volume does not change much, while $B_z \propto t$ and $(W - W\mathrm{pot}) \propto t^2$.

(3) In the asymptotic phase, the flux volume increases so that $\Sigma(\psi) \propto t^2$, while $B_z \propto t^{-1}$ and $W \propto \log t$.

(4) When $t \rightarrow \infty$, the solution asymptotically converges to a quasi-potential configuration, where from the innermost sheared field line all the outer field lines are open.

Proofs of the above arguments are not available yet, but if proven, they will be able to bestow a theoretical basis and generality on our conclusions.

The study by Biskamp and Welter (1989) is the only MHD simulation of a single isolated arcade in a z-invariant geometry known to date and they employed the same flux profile at the bottom boundary as ours. Since their shear profile is different from ours, we will consider the shear at the $|B_y|$ maximum to make a comparison between their results and ours. Their simulation was continued up to $\zeta_m \approx 8$ in our units, but no hint of our third evolutionary phase was witnessed, for which we can think of several reasons. Firstly, their boundary treatment for B_z caused unwanted slippage of field lines as indicated by Steinolfson (1991). Secondly, they included a resistivity from the beginning and it retarded the development of a current layer. Finally, their shear profile has a maximum far outside the B_y maximum. Our unreported study shows that the current layer formation is less favored with such a shear pattern. It should be mentioned in this regard that slippage of field lines usually reduces shear in the inner field lines and increases shear in the outer field lines (Steinolfson, 1991). The force-free solutions obtained by Klimchuk *et al.* (1988) are based on a flux profile slightly different from ours and the imposed shear in their own normalization was only up to $\zeta_m \approx 5$. It thus seems natural that they could not find any manifestation of a current layer.

Comparing our study with studies by Mikić and Linker (1994) and Roumeliotis *et al.* (1994), it can be said that the last evolutionary phase in 2-D Cartesian geometry corresponds to the highly expansive phase in axisymmetric geometry. What makes the evolutions in the two

geometries so different is that the partial opening up of field lines requires a finite shear in the latter, but an infinite shear in the former. In a small finite domain, however, a highly sheared z-invariant field also looks like a partially open field with a quasi-singular current layer.

CHAPTER 4

Effect of Resistivity and Eruption of a Sheared Magnetic Arcade

4.1 Introduction and Modelling

Historically, the simulation study by Mikić *et al.* (1988) first demonstrated that the resistive evolution of magnetic arcades undergoing shearing motion can end up in magnetic reconnection and expulsion of a plasmoid. Their magnetic field model consisted of periodic arcade structures. It was pointed out by Biskamp and Welter (1989) that the breaking of the symmetry due to a numerical roundup error enabled an instability to develop in the multiple arcade system in Mikić *et al.* (1988). Biskamp and Welter (1989) further presented a simulation result that a single isolated arcade does not erupt when sheared under resistivity. However, Steinolfson (1991) pointed out that the boundary condition on the toroidal field used by Biskamp and Welter (1989), which was a first order extrapolation, could not create as much shear as prescribed. Steinolfson (1991) simulated evolution of an axisymmetric arcade in spherical geometry and found a dynamic stage after a long shear, but no reconnection was observed. Lee (1990) and Inhester *et al.* (1992) found that magnetic reconnection can take place in a 2-D arcade when a converging footpoint motion is added to a shearing motion. In these studies, however, it was somewhat uncertain what the role of the converging motion is. The converging motion is an effective way to increase the shear angle, and the results of these studies may imply that highly sheared arcades are vulnerable to magnetic reconnection. However, their magnetic fields behave quite dynamically before the reconnection, and a kind of dynamic pinching might play an essential role in the thinning of the current layer. In this respect, Lee (1990) suggested that

magnetic reconnection is triggered at the point, on which most of Poynting fluxes generated by the converging motion are focused. The reasoning by the above authors was more biased towards the dynamic effect of converging motions than the quasi-static effect. It was Mikić and Linker (1994) who for the first time showed that magnetic reconnection can take place in a single magnetic arcade in axisymmetric spherical geometry when only a shearing motion is imposed. In a zero β simulation, they also found that the magnetic field tends to open up partially and form a current sheet beyond a certain amount of shear. The partial opening up of field lines for a finite shear was first proposed by Low (1986) in axisymmetric geometry. Lynden-Bell and Boily (1994) showed that an axisymmetric field fully opens up after a certain amount of rotation of the flux of one polarity. However, their footpoint displacement has a discontinuous jump across the polarity inversion line. As suggested by Aly (1985) and as seen in the previous chapter, opening up of field lines is impossible in 2-D Cartesian geometry for a finite shear. Thus, no singular current sheet appears. Then comes the question: "Is the magnetic reconnection possible in a magnetic arcade in 2-D Cartesian geometry without dynamic pinching effect or driving boundary condition?" One may think that this problem is purely of theoretical interest and of minor significance because the real solar magnetic field is best described in 3-D or at least in 2-D spherical geometry. However, as long as magnetic reconnection occurs in a non-singular current layer as in Mikić and Linker (1994), this question has a full meaning and can also be shaped as "How is the current layer not dispersed but rather becomes so thin to make the reconnection possible?" This question is not trivial as long as there are field lines which cross the current layer and are tied to a rigid boundary. The problems that will be addressed in this thesis is of equal significance regardless of the assumed geometry.

In this chapter, we employ the same numerical model as in Section 3.3 except that a nonzero resistivity is included in the induction equation (Equations (3.24) and (3.25)). The normalization of units is the same as in Chapter 3. The magnetic field B is referenced to

B_0 which is the maximum magnitude of B_y at the base, the length to L_0, half the distance between the B_y maxima, the mass density to the initial density ρ_0 at the base, the velocity v to $v_0 = B_0/(4\pi\rho_0)^{1/2}$, the time t to $t_0 = L_0/v_0$, and the resistivity to $L_0 v_0$. For the numerical values of these units, see Table 3.1. In this chapter, the x-coordinate of the footpoint of the field line labeled by ψ is denoted by $x_o(\psi)$. As defined in Section 3.2, $\zeta(x_o)$ denotes the distance, over which the fluid element at $(x = x_o(\psi), y = 0)$ has moved in the z-direction from the initial position in the potential field. We define ζ_m to be $|\zeta(x_o = \pm 1)|$. The half distance in the z-direction between two conjugate footpoints is designated by $Z(x_o)$, which is half the differential toroidal flux at $\psi(x_o)$. In ideal MHD evolution $\zeta(x_o)$ is identical to $Z(x_o)$ whereas in resistive evolution these two are generally different. The symbol $\Sigma(\psi)$ represents the area surrounded by the x-axis and the field line labeled by ψ projected on the x-y plane. The differential flux volume (area in 2-D) is thus $|d\Sigma/d\psi|$.

In most cases, we apply resistivity to a sheared arcade obtained in Chapter 3 without any more motion at the bottom boundary. This separation of the resistive evolution from the ideal MHD evolution enables us to see the effect of resistivity clearly. Further, in the real solar corona, the resistivity is so small that the ideal MHD modelling is more adequate before the current layer becomes very thin or anomalous resistivity sets in.

The organization of this chapter is as follows. In Section 4.2, we examine the possibility of magnetic reconnection in a sheared arcade in z-invariant geometry and investigate the existence of a critical shear for reconnection. In Section 4.3, the effect of resistivity on an arcade-like magnetic field is considered especially regarding development of a current sheet. In Section 4.4, eruptive behaviors of a magnetic arcade are studied for different values of resistivity and for different resistivity patterns. Section 4.5 gives a brief summary.

4.2 When Is Magnetic Reconnection Possible in a Magnetic Arcade?

In this study, we have tried to minimize dynamical effects of footpoint motions on the initiation of magnetic reconnection. For this purpose, the shearing speed is ramped down to zero in $200\,t_0$ before resistivity is applied. To investigate the reconnection processes, a wide range of resistivity is tried from $\eta = 10^{-5}$ to 10^{-2}, which value is the inverse of the magnetic Reynolds number (Lundquist number) with repect to L_0 and v_0. The smallest usable value of resistivity is determined by the numerical resolution and the affordable resistive evolution time span, and in our case it is $\eta = 10^{-5}$.

A typical resistive evolution of a sheared arcade is shown in Figure 4.1. In this case, a spatially uniform resistivity of $\eta = 10^{-5}$ is applied to an arcade with $\zeta_m = 10.9$ from $t = 11000\,t_0$, and an X-line first appears at $t = 12086\,t_0$. It is shown that the magnetic island grows in size and rises as more flux is reconnected. Reserving further description of the resistive evolution for Section 4.4, we address the primary question whether there exists a critical value of shear below which magnetic reconnection is impossible for any resistivity. Although we only need to employ a certain large value of resistivity for this purpose, we tried three resistivity values: $\eta = 10^{-2}, 10^{-3}$ and 10^{-4}. The time duration between the outset of diffusion and the first appearance of an X-line is measured in arcades with different shears for different values of resistivity and plotted in Figure 4.2. The time required for reconnection with $\eta = 10^{-2}$ is found to be about one fourth of the time for $\eta = 10^{-3}$, which in turn is about one sixth of the time for $\eta = 10^{-4}$. The slope of each curve $d(\log_{10}\Delta t)/d\zeta_m$ is found asymptotically constant for a large shear. The increase of the slope in $\zeta_m > 24$ for $\eta = 10^{-2}$ is somewhat uncertain because the time required for reconnection in that part is so small as to be comparable to the time-step size which is the unit in our time measurement. The near parallelism of the three curves is suggestive of the tearing mode, the growth rate of which is proportional to a certain power of

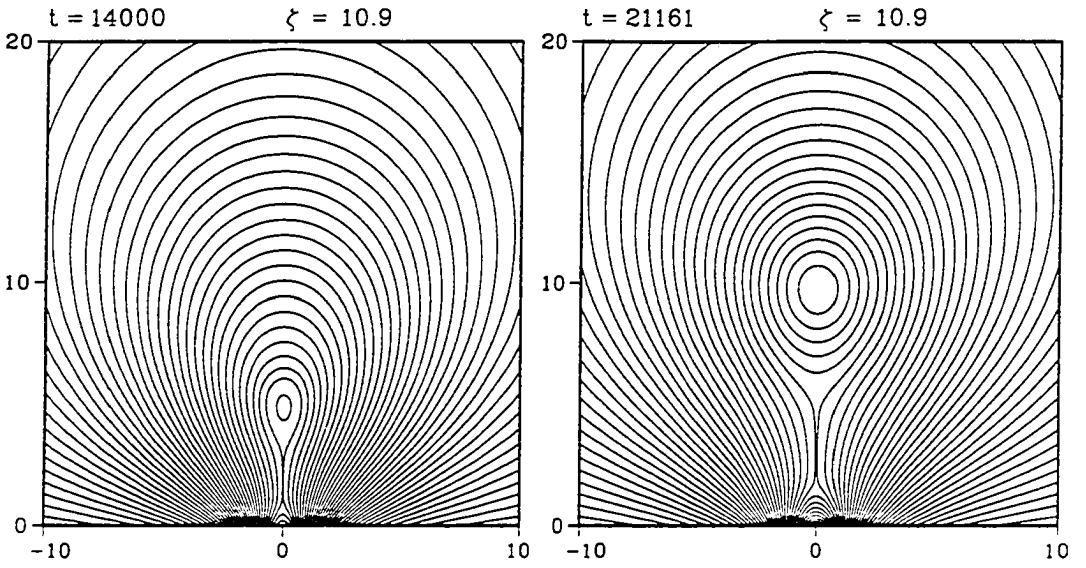

Figure 4.1 The resistive evolution of the magnetic arcade of $\zeta_m = 10.9$ (Case 4A). A uniform resistivity of $\eta = 10^{-5}$ is applied from $t = 11000\,t_0$.

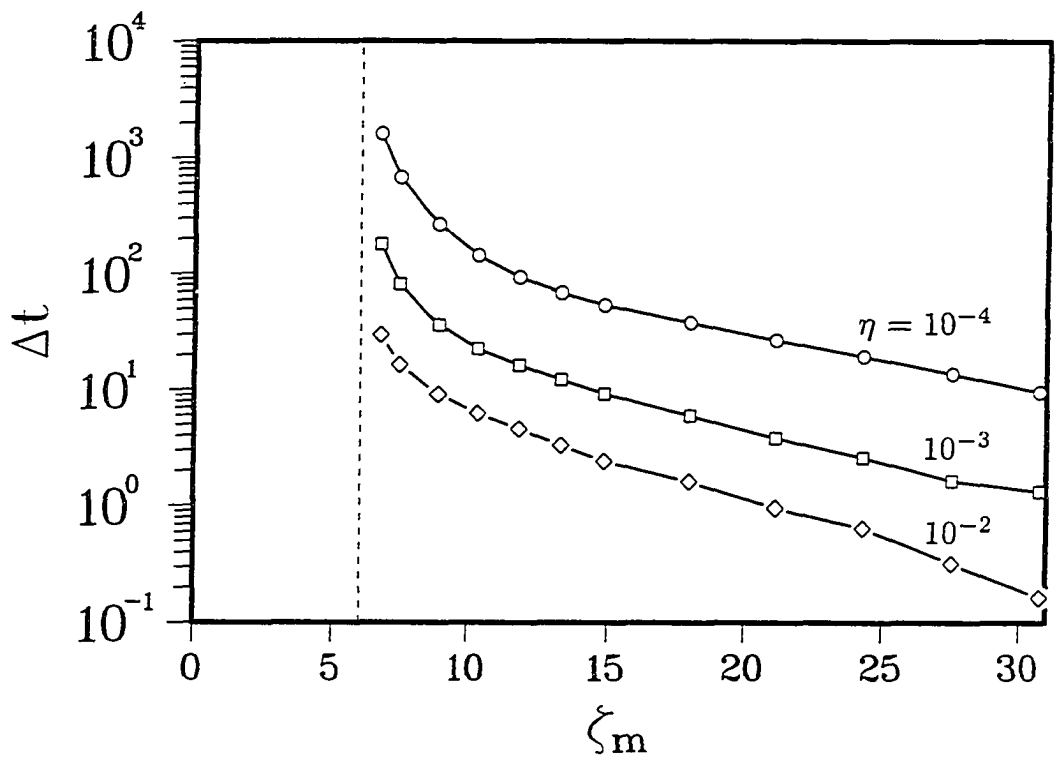

Figure 4.2 Time required for reconnection versus shear. The circles stand for $\eta = 10^{-4}$, the squares for $\eta = 10^{-3}$ and the diamonds for $\eta = 10^{-2}$.

the resistivity, i.e., $\omega \propto \eta^{\alpha}$, where $\alpha = 3/5$ for a fixed wavenumber and a fixed width of the current layer (Furth *et al.*, 1963). The value of α obtained from the two upper curves is 0.8 and that from the two lower curves is 0.6. This discrepancy is thought to be a nonlinear effect since the current layer evolves more rapidly under higher resistivity. As going to a smaller shear, the slopes of the curves increase and no reconnection is found for $\zeta_m = 6$ with whatever resistivity applied for as long as $\Delta t \approx 5 \times 10^4\, t_0$. It can be thus said that there exists a critical shear for magnetic reconnection in a magnetic arcade. For our flux and shear pattern, the critical value lies between $\zeta_m \approx 6$ and 6.7. The main difference between the resistive evolutions above and below the critical shear is that the current density increases in the former, but decreases in the latter. This property will be treated in the following section. It is also interesting that the critical shear approximately corresponds to the point where the third phase of the arcade evolution starts in ideal MHD as found in the previous chapter.

In relation to our results, it should be remarked that Aly (1990) asserted that there are more than one field configuration with different topologies if the shear exceeds a certain value. According to him, these states are all ideal MHD stable and can make transition to another state only by a pointwise reconnection during which the toroidal differential flux for every value of flux function is approximately conserved. The minimum energy state will have a topology containing magnetic islands. In numerical simulations with finite resolution, it is impossible to achieve such a pointwise reconnection, and the toroidal differential flux inevitably undergoes modification due to diffusion. Our results may not serve as a direct proof of Aly's assertion, but provide a convincing support for it.

The diffusion process does not change either the total poloidal flux or the total toroidal flux. The conservation of the poloidal flux is guaranteed if the maximum and minimum of ψ are

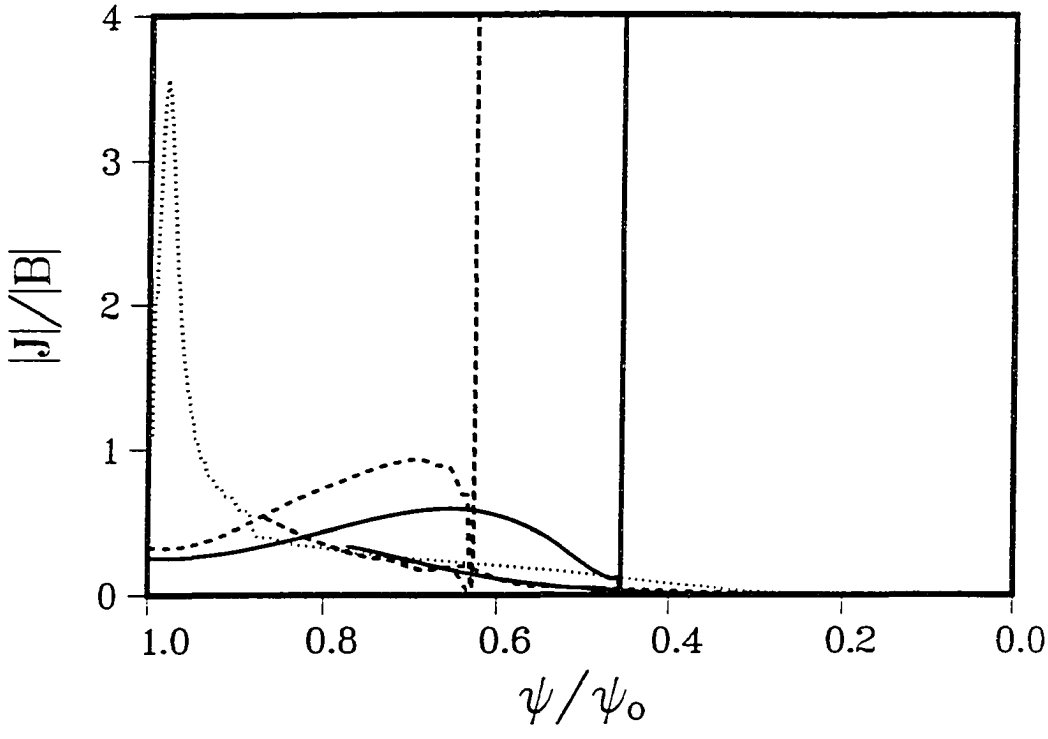

Figure 4.3 The ratio of current density to magnetic field $|\mathbf{J}|/|\mathbf{B}|$ in the y-axis versus the flux function ψ at three different times in the evolution of an arcade with $\zeta_m = 10.9$ under a uniform resistivity $\eta = 10^{-5}$. The dotted line is for $t = 11000\,t_0$, when the diffusion is about to start, the dashed line for $t = 31911\,t_0$ and the solid line for $t = 51714\,t_0$.

located on the boundary before the diffusion. The total toroidal flux

$$\Phi_z = \int_{y=0}^{\infty} \int_{x=-\infty}^{\infty} B_z dx dy = 2 \int_0^{\psi_o} \zeta(\psi) d\psi \tag{4.1}$$

is conserved if there is no diffusion of B_z across the boundary. The helicity of the whole system (see Appendix B for derivation)

$$K_w = 2 \int_{\psi_o}^{0} \psi \zeta(\psi) d\psi \tag{4.2}$$

is not necessarily conserved under diffusion. However, if the diffusion takes place in sufficiently small volumes, the total helicity is approximately conserved as Taylor conjectured (Taylor, 1974). If the total helicity is given as a constraint, the minimum energy state is a linear force-free field described as

$$\nabla \times \mathbf{B} = \alpha \mathbf{B}, \tag{4.3}$$

where α is constant over the whole domain (Woltijer, 1958). The state before diffusion is not necessarily a linear force-free field because imposing the shear $\zeta(\psi)$ in ideal MHD is equivalent to imposing the differential helicity

$$H(\psi) = -\frac{dK(\psi)}{d\psi} = -2\psi\zeta \tag{4.4}$$

on each flux surface. Here we investigate how close the reconnected field configurations are to linear force-free fields. The arcade evolution shown in Figure 4.1 is further followed and the ratio of current density to magnetic field $|\mathbf{J}|/|\mathbf{B}|$ is plotted along the y-axis as function of ψ at three different times (Figure 4.3). Just before the outset of diffusion at $t = 11000\, t_0$, the curve (dotted line) has a sharp peak around $\psi = 0.98\psi_o$ and the state is far from a linear force-free field. After magnetic reconnection is initiated at $t = 12086\, t_0$, each curve shows two turning points, one at the X-line and the other at the O-line. Except for the sharp peaks at the X-line,

the curves for the reconnected configurations are much flattened compared to the ideal MHD case. The curve for $t = 51714\,t_0$ (solid line) is more flattened with a smaller maximum than the curve for $t = 31911\,t_0$ (dashed line) if the neighborhood of the X-line is excluded. It can be thus said that the reconnection process drives the system asymptotically towards a linear force-free field. In this regard, Kusano *et al.* (1995) has shown that the linear force-free field solution bifurcates into two different states when the total helicity is increased. They further proposed that a solar flare is a transition between two different Woltijer-Tayler states. This study must be paralleled with Aly's study, for the former deals with the total helicity constraint while the latter is concerned with helicity constraints in each flux surface. Due to the huge magnetic Reynolds number in the solar atmosphere ($\sim 10^{14}$), the field configuration before the reconnection triggering is far from a linear force-free state. The state after the reconnection triggering is never a state conserving differential helicities either. Therefore, conditions for multiple solutions by Aly (1990) and Kusano *et al.* (1995) both need to be satisfied to trigger magnetic reconnection and create a plasmoid in a magnetic arcade system.

4.3 Effect of Resistivity in Arcade-like Field Geometry

To find the effect of resistivity, we examine the evolution of the maximum current density ($|J_z|_{max}$) within the computational domain in five different cases for two maximum shears $\zeta_m = 6.3$ and 10.9 (Figure 4.4). The first case is an ideal MHD evolution without resistivity (thin solid line), in which $|J_z|_{max}$ does not change after the shearing motion is stopped. The second case is a resistive evolution with $\eta = 10^{-5}$ (thick solid line). For $\zeta_m = 6.3$, the $|J_z|_{max}$ decreases and no reconnection takes place whereas for $\zeta_m = 10.9$, the $|J_z|_{max}$ increases and reconnection is observed. In the third case (dashed line), only the poloidal field is diffused with $\eta = 10^{-5}$ and the evolution is similar to the second case except that the increase ($\zeta_m = 10.9$)

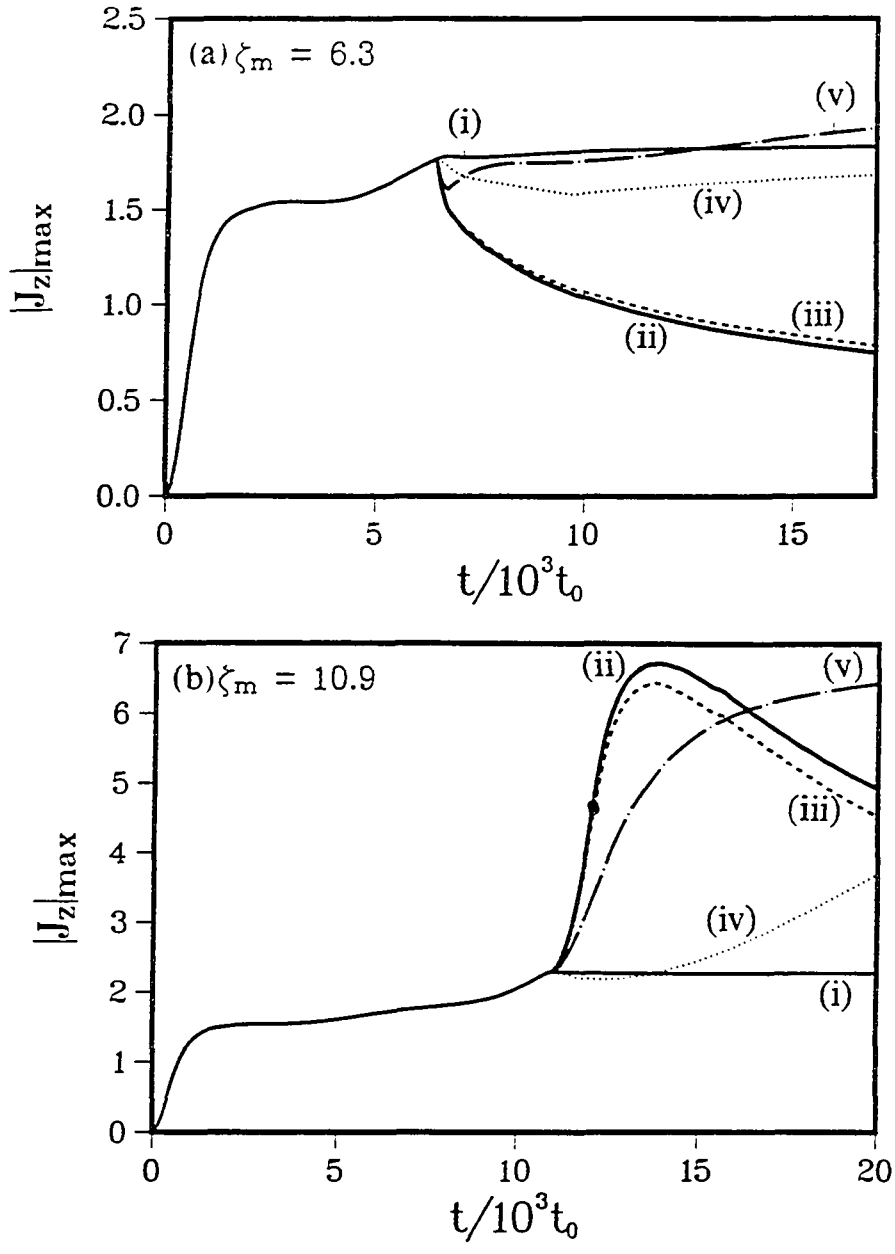

Figure 4.4 Evolution of $|J_z|_{max}$ with time for (a) $\zeta_m = 6.3$ and (b) $\zeta_m = 10.9$. (i) The thin solid line represents the ideal MHD evolution. (ii) The thick solid line is for the case with nonzero resistivity, (iii) the dashed line for the case with diffusion in the poloidal field only, (iv) the dotted line for the case with diffusion in the toroidal field only and (v) the chain-dotted line for the case with diffusion in the toroidal field only near the bottom boundary. The dots are the points where an X-line first appears.

or decrease ($\zeta_m = 6.3$) of $|J_z|_{max}$ is a little slower than in the second case. In the fourth case (dotted line), diffusion is applied only to the toroidal field with $\eta = 10^{-5}$ and the current density is found to decrease first slightly and then keep increasing for both shear values. While a uniform resistivity is applied in the second to the fourth case, the following nonuniform resistivity is imposed to the diffusion of the toroidal field in the fifth case (chain-dotted line):

$$\eta(y) = \begin{cases} \frac{1}{2}\eta_0\left[1 + \cos\left(\frac{\pi y}{y_0}\right)\right], & \text{if } 0 \le y \le y_0; \\ 0, & \text{if } y > y_0, \end{cases} \tag{4.5}$$

where $\eta_0 = 2 \times 10^{-4}$ and $y_0 = 1$ are adopted. This case is designed to simulate a diffusion only in the photosphere, where the resistivity is about six thousand times the coronal value, although the adopted value is about five orders of magnitude higher than the classical value. Since y_0 is also much larger than the thickness of the photosphere, diffusion of the poloidal field is excluded to investigate the evolution without reconnection. In this case, the current density continues to increase although there is a slight fall for $\zeta_m = 6.3$. It is interesting that the diffusion in the toroidal field always increases the current density in the end while the diffusion of the poloidal field either increases or decreases the current density depending on whether the shear exceeds the critical value.

The arcade evolution in the fifth case for $\zeta_m = 10.9$ is illustrated in Figure 4.5. As the B_z diffuses from the innermost part of the arcade towards the outer part, the central field lines fall down and the current layer becomes thinner. To examine the current sheet thinning more closely, the toroidal field B_z (thin lines) and the half z-distance between the conjugate footpoints Z (thick lines) are plotted as functions of the footpoint coordinate $x_o(\psi)$ at $y = 0$ before and after the toroidal field diffusion in Figure 4.6. As in Figure 4.5, the configuration before the diffusion is obtained at $t = 11000\,t_0$ (dashed lines) and that after the diffusion is at $t = 14000\,t_0$ (solid lines). As mentioned in Chapter 3, the shear profile prescribed by Equation (3.30) generates only negative J_z, and the B_z is a monotonically increasing function of ψ (decreasing function

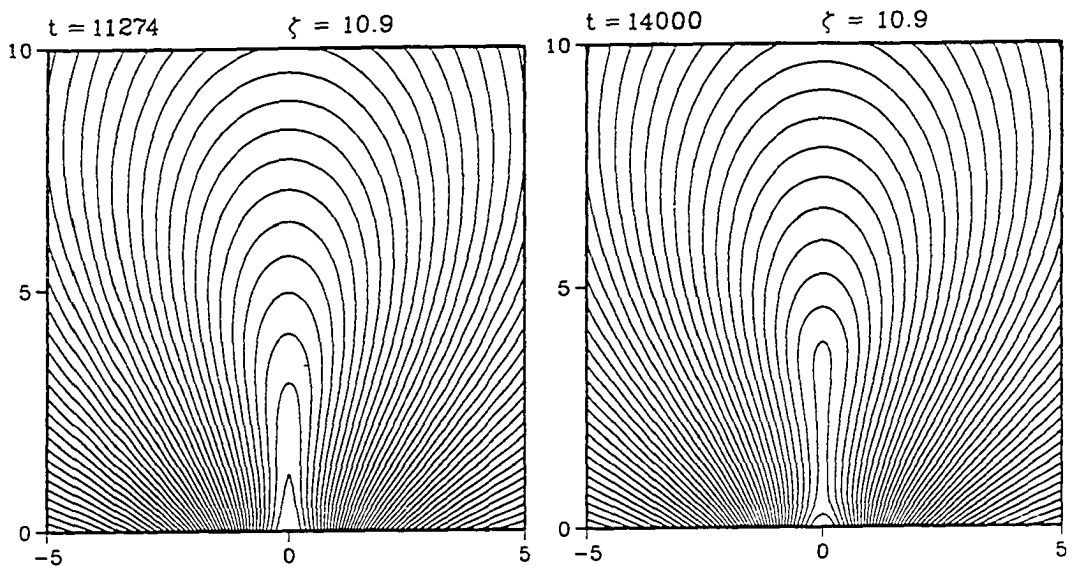

Figure 4.5 Evolution of the magnetic field when resistivity ($\eta_0 = 2 \times 10^{-4}$) is applied to the toroidal field only near the bottom boundary. The development of a current layer is to be noticed.

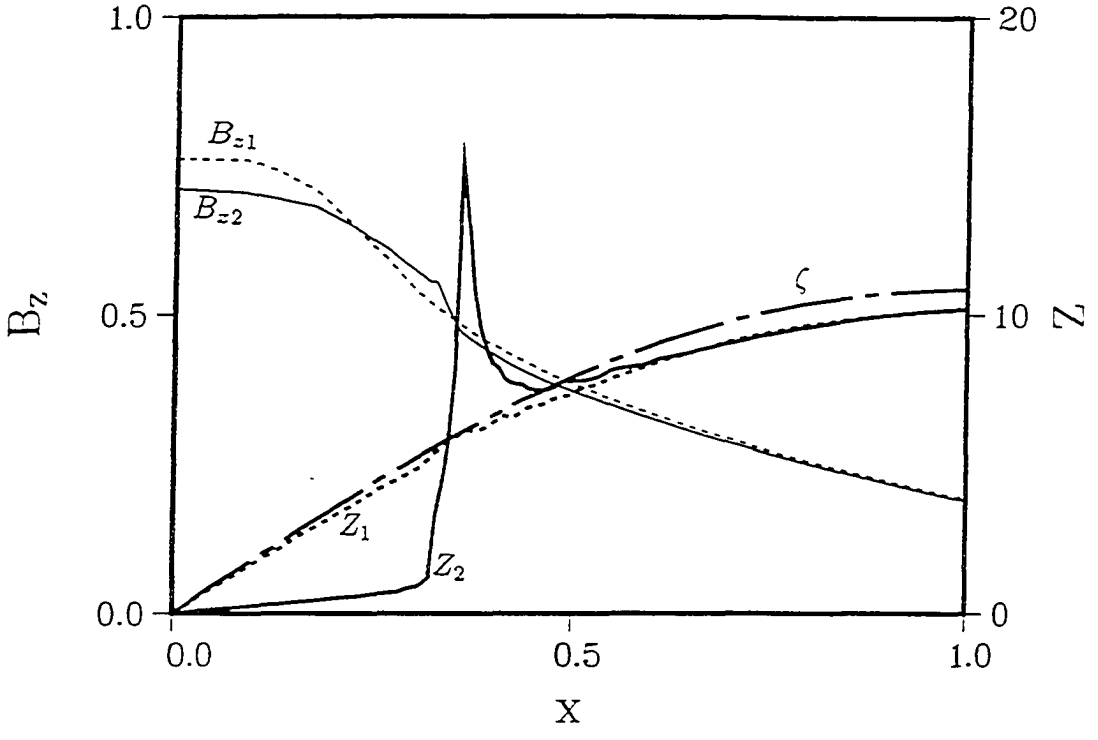

Figure 4.6 The toroidal field B_z and the half z-distance between the conjugate footpoints Z as function of the footpoint coordinate x at the bottom boundary. The thin lines represent B_z and the thick lines Z. The dashed lines and subscript 1 are for the configuration before the toroidal field diffusion ($t = 11000\, t_0$), and the solid lines and subscript 2 are for the configuration after the diffusion ($t = 14000\, t_0$). The thick chain-dashed line shows the prescribed shear at $\zeta_m = 10.9$.

of $|x_o|$). On the other hand, the shear $\zeta(\psi)$ is a decreasing function ψ (increasing function of $|x_o|$) in $|x_o| \leq 1$. When resistivity is applied to the toroidal field, the diffusion takes out B_z from the innermost part of the arcade ($|x_o| \lesssim 0.33$ in the shown case) and delivers it to the outer part ($|x_o| \gtrsim 0.33$) keeping the monotonicity of $B_z(\psi)$. Consequently, the differential toroidal flux is decreased in the innermost part, but increased in the outer part, which results in a sharp gradient region in the differential toroidal flux, $Z(\psi(x_o))$. It is known from the numerical study by Lee *et al.* (1995) that the sharper the gradient in $Z(\psi)$ is, the higher gradient is generated in $B_z(\psi)$. As shown in the figure, $\partial^2 B_z/\partial x_o^2$ is so small in $|x_o| \gtrsim 0.5$ that there is little diffusion and the outward transport of the toroidal flux is stagnant to cause a high peak in the $Z(x_o)$ curve. Since $Z(\psi) = B_z(\psi)V(\psi)$, where $V(\psi) \equiv d\Sigma/d\psi$, the high peak in Z means a large differential flux volume, i.e., a stretched current layer. Since the higher gradient in $B_z(\psi)$ leads to the higher gradient in $Z(\psi)$, this process of the current layer thinning is self-accelerated and can be considered as an instability.

In passing, it should be mentioned that the actual footpoint displacement before the diffusion (thick dashed line) shows a discrepancy with the prescribed shear (chain-dashed line) within 7 % due to the numerical slippage. The discrepancy generally appears as a deficit in shear in $|x| \lesssim 2$ and as a surplus in shear in $|x| \gtrsim 2$ and the total toroidal flux is very little different from the prescribed flux. We have not taken any measure to correct this discrepancy as Steinolfson (1991) did, but the relative error in shear is found not to exceed 8 % even for $\zeta_m \approx 100$.

Another numerical experiment is performed to illustrate the growth of a current layer by the toroidal field diffusion only near the bottom boundary. In this case, the resistivity given by Equation (4.5) is applied while the arcade is sheared from the initial potential field. As shown in Figure 4.7, the current layer evolves into a quasi-singular layer. In ideal MHD evolution seen in the previous chapter, all the field lines are lifted as the shearing motion continues. In the case of diffusion, the innermost field lines fall down whereas the next outer field lines are stretched out.

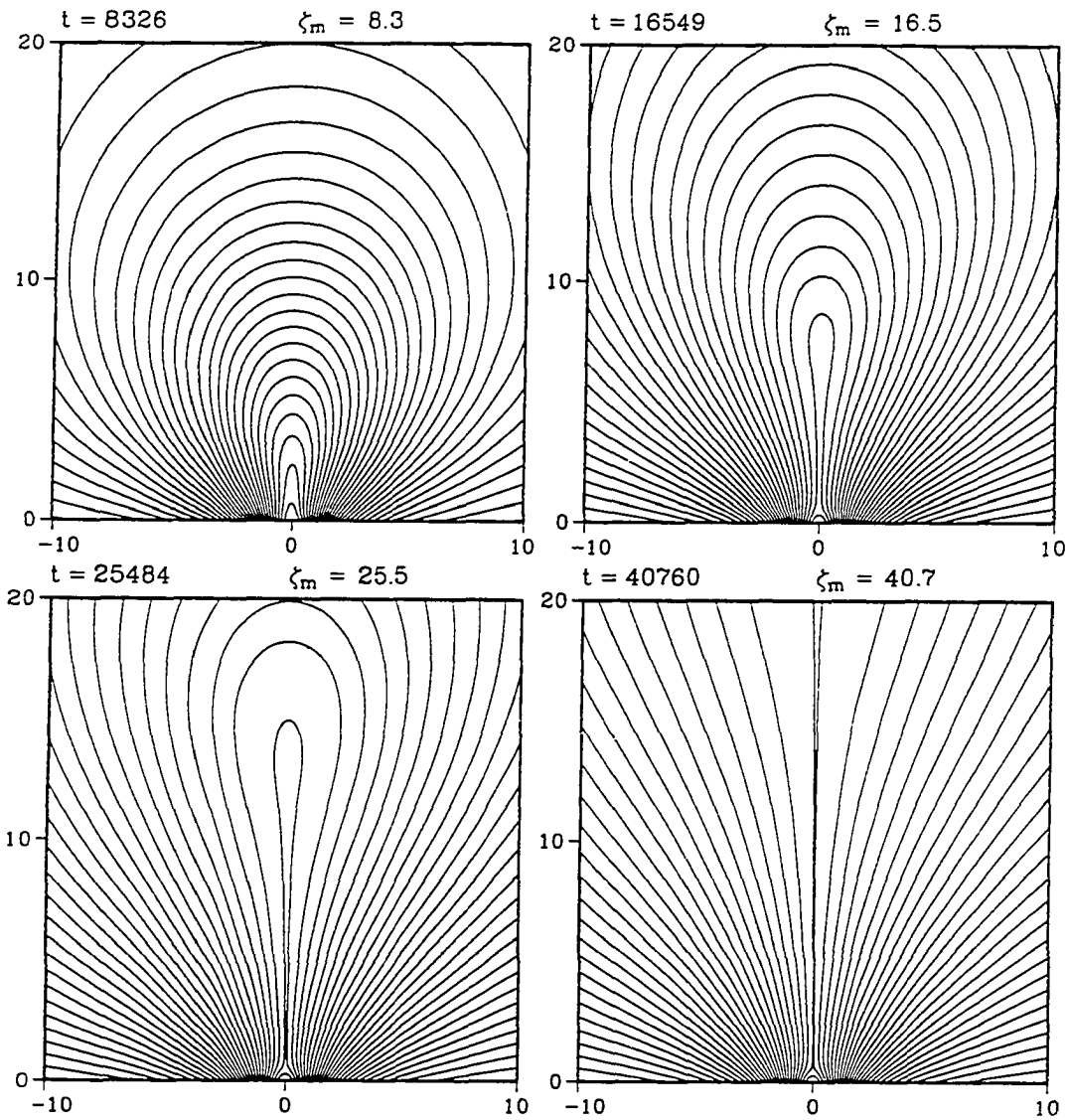

Figure 4.7 The evolution of a magnetic arcade being sheared with a thin resistive layer near the bottom boundary. To prevent magnetic reconnection only the toroidal field is diffused.

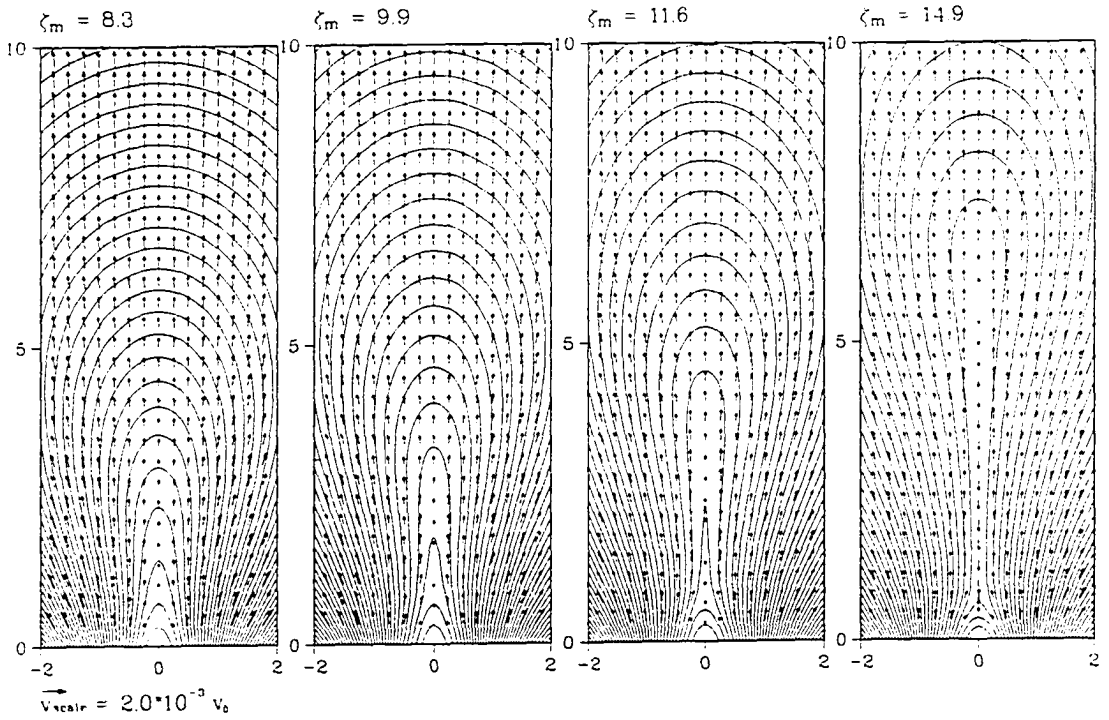

Figure 4.8 The formation of a thin current layer during the evolution shown in Figure 4.7. Magnetic field lines and velocity fields are shown. The outward transport of the toroidal flux leads to the collapse of the innermost field lines as well as the distension of the outer field lines.

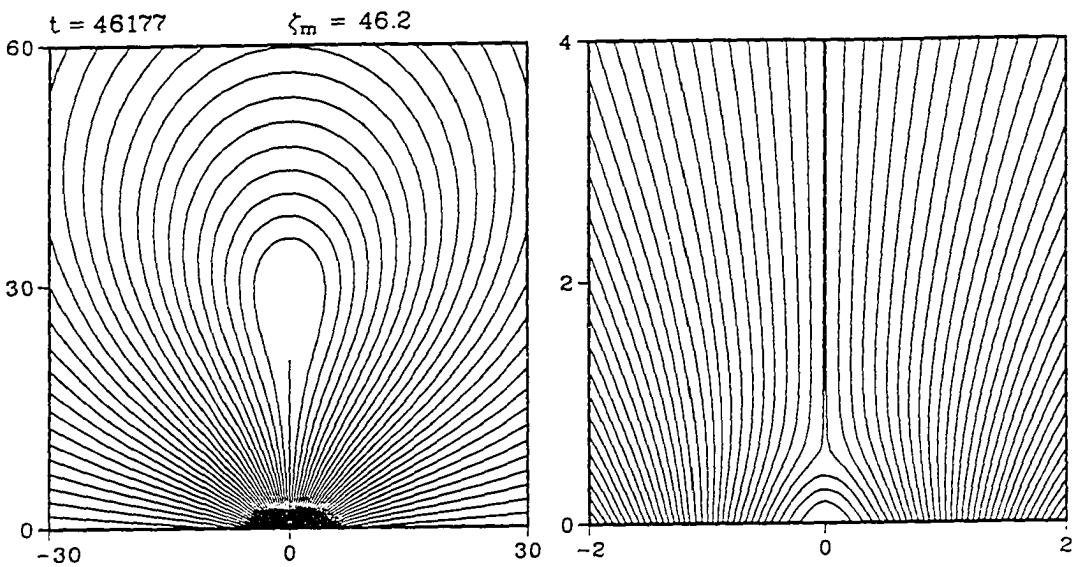

Figure 4.9 The field configuration at $t = 46177\,t_0$ in the evolution shown in Figure 4.7. Both large-scale and small-scale views show a quasi-singular nature of the current layer.

This process of "dipolarization" is shown in Figure 4.8. The transport of the toroidal flux causes the inner field lines to collapse down and the outer field lines to bulge out. The current layer is vertically elongated and laterally pinched and thus becomes resembling a singular current sheet. Figure 4.9 shows large-scale and small-scale views of the field configuration at $t = 46177\,t_0$. In the large-scale plot, an almost discontinuous jump in the differential flux volume is readily noticed across the current sheet field line. The dipole-like structure of innermost field lines owing to the toroidal flux depletion is well revealed in the small-scale plot. One may think that our nonuniform diffusion of the toroidal field is a pure numerical experiment far from the real situation. We have also tried to diffuse both poloidal and toroidal fields and inevitably found magnetic reconnection. If the higher resistivity is confined only up to a few hundred kilometers above the surface as in the real Sun, the coronal reconnection is not necessarily effected even with a poloidal field diffusion because the current layer possibly bifurcates above the resistive layer. In this case, a quasi-singular current layer is expected to develop without reconnection in a process similar to the one involved in our numerical example.

Now we examine the diffusion of poloidal fields. The diffusion of poloidal fields tend to make the poloidal field more potential-like. The presence of the toroidal flux, however, does not allow all the field lines to become potential-like. The diffusion in the innermost field lines effects the transport of toroidal flux to the outer field lines. Where toroidal flux is increased, field lines tend to bulge out while the poloidal diffusion tend to shrink the field lines. These two effects compete against each other. When the poloidal diffusion is more effective, the toroidal flux coming from the inner part can be readily transported to the far outer part without being accumulated. When the poloidal diffusion is less effective, the toroidal flux is accumulated in a certain region and the current layer grows leading to magnetic reconnection. To see these two different regimes, we have applied poloidal diffusion to two different sheared fields: one with $\zeta_m = 6.3$ and the other with $\zeta_m = 10.9$. The former never leads to magnetic reconnection

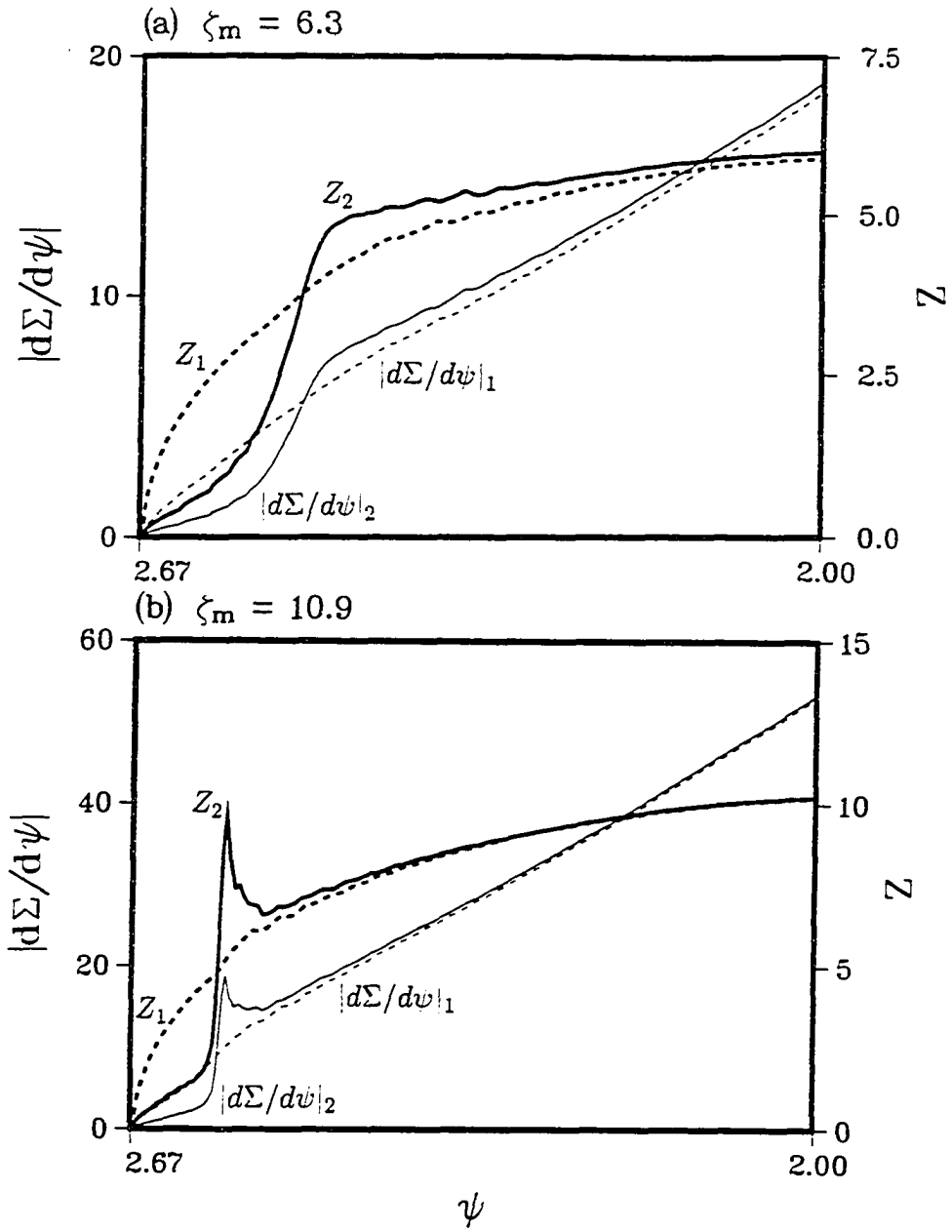

Figure 4.10 The differential flux volume $|d\Sigma/d\psi|$ and the half z-distance between the conjugate footpoints (or half the differential toroidal flux) Z as a function of the flux function ψ for (a) $\zeta_m = 6.3$ and (b) $\zeta_m = 10.9$. In terms of x-coordinate at the bottom boundary, $x_o(\psi = 8/3) = 0$ and $x_o(\psi = 2) = \pm 1$. The thin lines represent $d\Sigma/d\psi$ and the thick lines Z. The dashed lines and subscript 1 are for the configuration before the poloidal field diffusion ((a) $t = 6400\,t_0$; (b) $t = 11000\,t_0$), and the solid lines and subscript 2 are for the configuration after the diffusion ((a) $t = 11000\,t_0$; (b) $t = 12063\,t_0$).

while the latter undergoes reconnection $1113\,t_0$ after the diffusion is applied. In Figure 4.10, the differential flux volume ($|d\Sigma/d\psi|$ in thin lines) and the half z-distance between the conjugate footpoints, namely, half the differential toroidal flux (Z in thick lines) are plotted against the flux function ψ before (dashed lines) and after (solid lines) the poloidal diffusion is applied. In the case with $\zeta_m = 6.3$, a uniform resistivity of $\eta = 10^{-5}$ is applied to the poloidal field for $4600\,t_0$ after the footpoint shearing is ceased. As shown in the figure, the toroidal flux is transported from the inner part to the outer part and the differential flux volume in the inner part is reduced while that in the outer part is increased. Although the slope in the Z-ψ curve is a little bit increased there is no accumulation of toroidal flux, which indicates that the poloidal diffusion effectively transports the toroidal flux outward. In the case with $\zeta_m = 10.9$, the reported result is obtained $1063\,t_0$ after the uniform poloidal diffusion is applied, i.e., $50\,t_0$ before the reconnection is triggered. Here both the differential toroidal flux and the differential flux volume have a sharp peak, which means that the transport of toroidal flux is stagnant in the region of the current layer. It can be understood from the comparison of the above two cases that if the initial field is stretched beyond a certain extent the poloidal diffusion in the outer region cannot cope with the incoming toroidal flux. This is the reason why there is a critical shear for magnetic reconnection.

4.4 Arcade Evolution Depending on Resistivity Value and Pattern

4.4.1 Spatially Uniform Resistivity

The case shown in Figure 4.1, where a uniform resistivity of $\eta = 10^{-5}$ is applied to an arcade with $\zeta_m = 10.9$, is now named as Case 4A. The evolution in Case 4A is characterized by an elongated current layer around the X-line and a rather slow dynamics. The maximum

flow speed developed is of the order of $10^{-2}\, v_0$, which is little greater than the maximum flow speed in the ideal MHD evolution with $V_{z0} = 10^{-3}\, v_0$ described in Chapter 3. In reconnection theories (e.g., Lee and Fu, 1986), the magnetic reconnection rate is defined by

$$M_{e,i} \equiv \frac{v_x}{V_{Ap}}, \tag{4.6}$$

where the subscripts e (for external) and i (for internal) respectively indicate the locations far away from and close to the diffusion region and $V_{Ap} \equiv B_p/(4\pi\rho)^{1/2}$ is the poloidal Alfvén speed. The reconnection rate measured in Case 4A does not vary much within unit length from the current peak and is on average $\sim 5 \times 10^{-4}$. This value is about one fourth of the Sweet-Parker rate defined by $M_{i,SP} = R_{mi}^{-1/2} = (V_{Ai} l/\eta)^{-1/2}$ where l is the length of the diffusion region. (Sweet, 1958; Parker, 1963). The fact that the maximum flow speed is lower than the poloidal Alfvén speed upstream of the current layer $\sim 0.4\, v_0$ tells that the viscous diffusion overwhelms the evolution of the system. This case can thus be considered as a quasi-static evolution with a very small reconnection rate.

To study the dynamic evolution undergoing magnetic reconnection, we now apply four different resistivities to an arcade with $\zeta_m = 28.1$, which is far more sheared and contains a current layer with higher current density than that in Case 4A. Elevating the resistivity level, three cases are run with uniform resistivities $\eta = 10^{-5}$ (Case 4B), $\eta = 10^{-4}$ (Case 4C) and $\eta = 10^{-3}$ (Case 4D). Another case (Case 4E) is studied with a nonuniform resistivity depending on current density. Note that the application of resistivity starts from $t = 28200\, t_0$ in all these cases.

Figure 4.11 shows Case 4B, where a uniform resistivity of $\eta = 10^{-5}$ is applied to an arcade with the shear $\zeta_m = 28.1$. In this case, magnetic reconnection is initiated at $t = 28314\, t_0$ and the maximum flow speed is observed to be 0.2–0.3 v_0 in the narrow reconnection outflow region, which is of the order of the poloidal Alfvén speed upstream of the current layer. The average

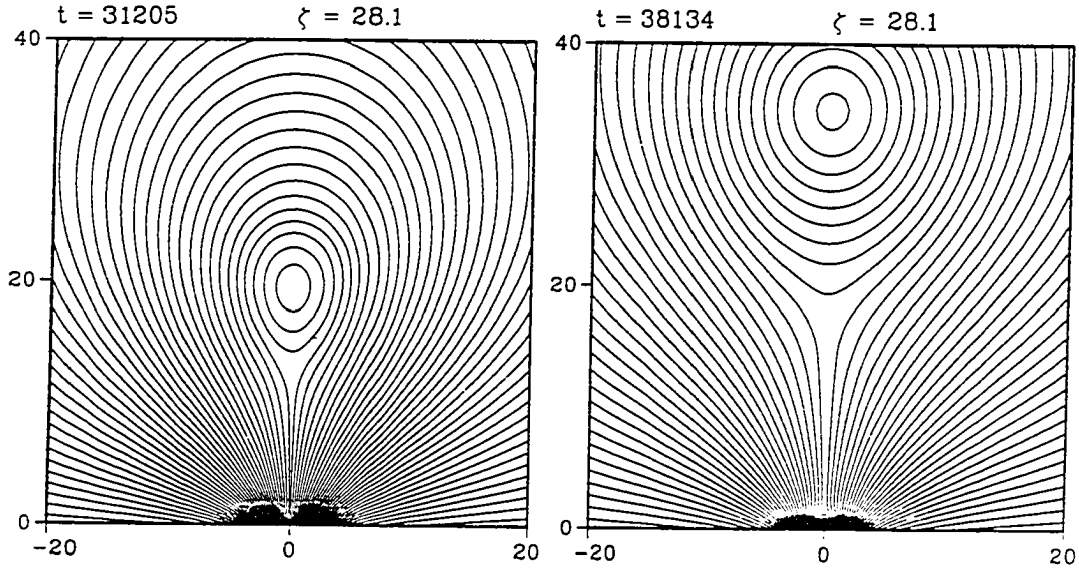

Figure 4.11 The evolution of the magnetic arcade of $\zeta_m = 28.1$ under the uniform resistivity $\eta = 10^{-5}$ applied from $t = 28200\, t_0$ (Case 4B).

reconnection rate near the current layer is $\sim 2 \times 10^{-3}$ and approximates the Sweet-Parker rate. As in Case 4A, the elongated current layer around the X-line and the slow evolution characterize this case.

In Case 4C, where $\eta = 10^{-4}$ is adopted, magnetic reconnection first takes place at $t = 28212\, t_0$ and the reconnection rate is about 5×10^{-3} near the current layer though more fluctuating in space and time than in the earlier cases. As shown in Figure 4.12, the plasmoid is expelled out of the computational domain during the simulation run and the O-line transits the upper boundary at $t \approx 36760\, t_0$ (see Figure 4.13a). Though in a small spot, the maximum flow speed is observed to reach $1.8\, v_0$, which is close to the poloidal Alfvén speed upstream of the current sheet. The rising speed of the magnetic island is much less, i.e., of the order of $0.02\, v_0$ as shown in Figure 4.13a. In this case also, the current layer around the X-line is rather long and the separatrices crossing at the X-line subtend a very acute angle.

In Case 4D, where $\eta = 10^{-3}$ is employed, magnetic reconnection is initiated at $t = 28202\, t_0$ and the O-line transits the upper boundary at $31500\, t_0$ (see Figures 4.14 and 4.13a), which is far earlier than the transit time in Case 4C. The rising speed of the magnetic island is on average $0.045\, v_0$ more than twice the rising speed in Case 4C (see Figure 4.13a). The maximum flow speed, however, is only around $0.3\, v_0$ far smaller than that in Case 4C, but of the order of the upstream poloidal Alfvén speed. This indicates that the magnetic field lines upstream of the current layer are not so dense as in Case 4C. The current layer is also wider and shorter compared to the earlier cases. The reconnection rate just outside the current layer ($x \lesssim 0.5$) is in the range of $M_i \approx 0.04$-0.05 and the rate at $x \approx 2$-3 is $M_e \approx 0.06$-0.07. Farther away from the diffusion region ($x \gtrsim 10$), the inflow speed is reduced for all the cases and even a negative speed is observed at times in some cases owing to the arcade expansion. In our geometry, dynamics far away from the diffusion region is mostly governed by the plasmoid expansion and the line-tying effect and little affected by the rarefaction wave launched by the reconnection process.

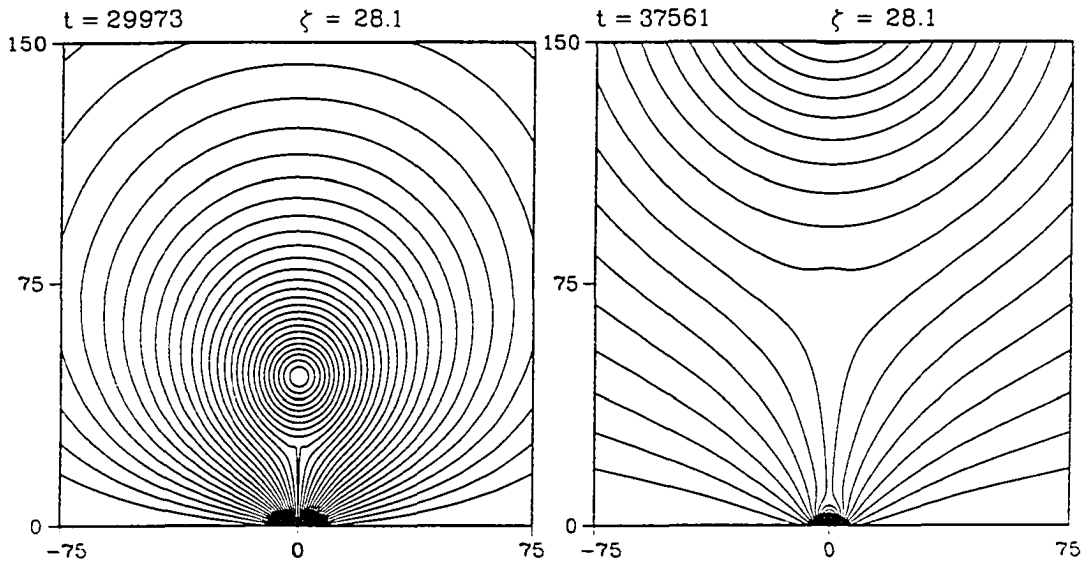

Figure 4.12 The evolution of the magnetic arcade of $\zeta_m = 28.1$ under the uniform resistivity $\eta = 10^{-4}$ applied from $t = 28200\, t_0$ (Case 4C).

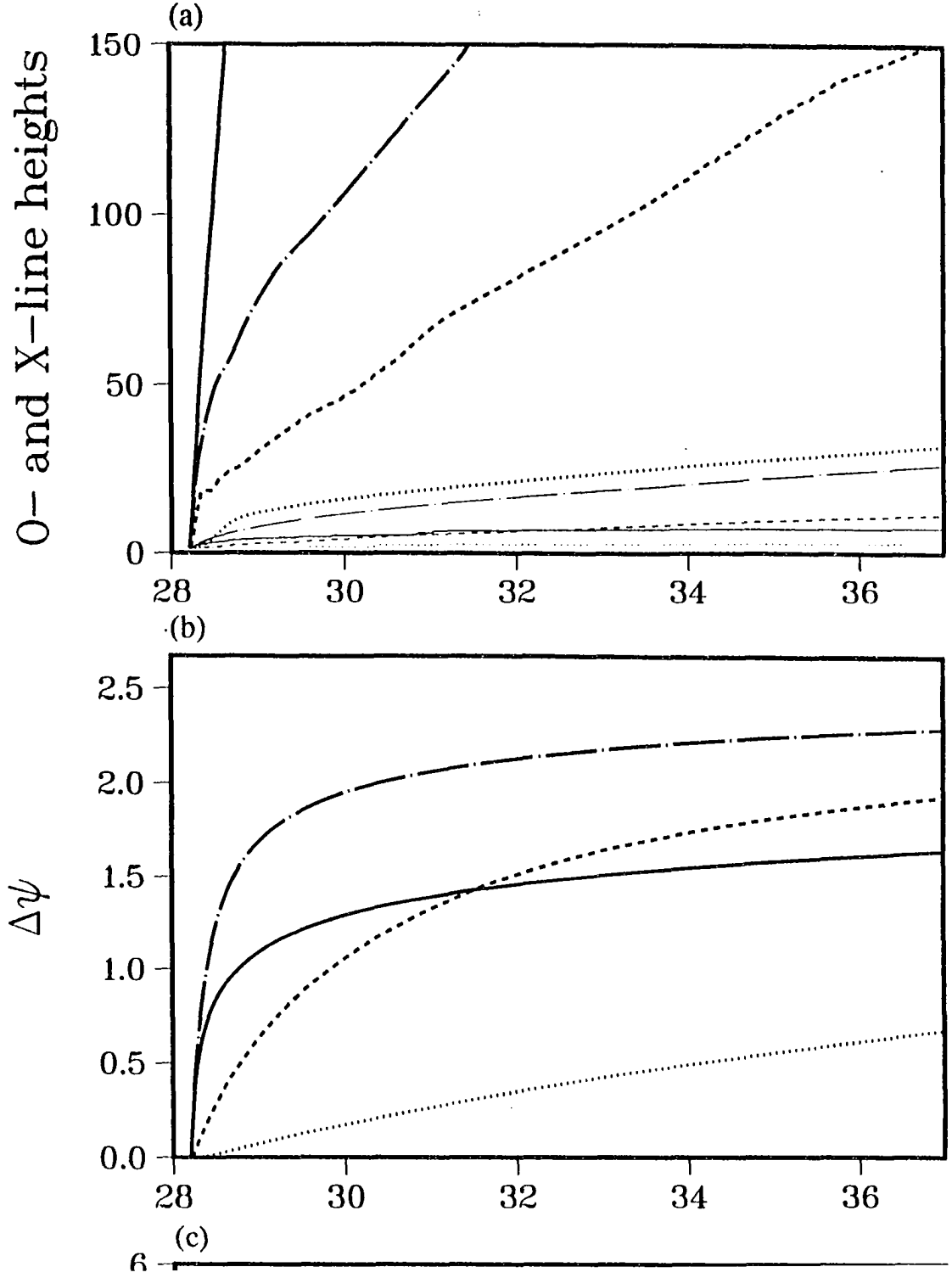

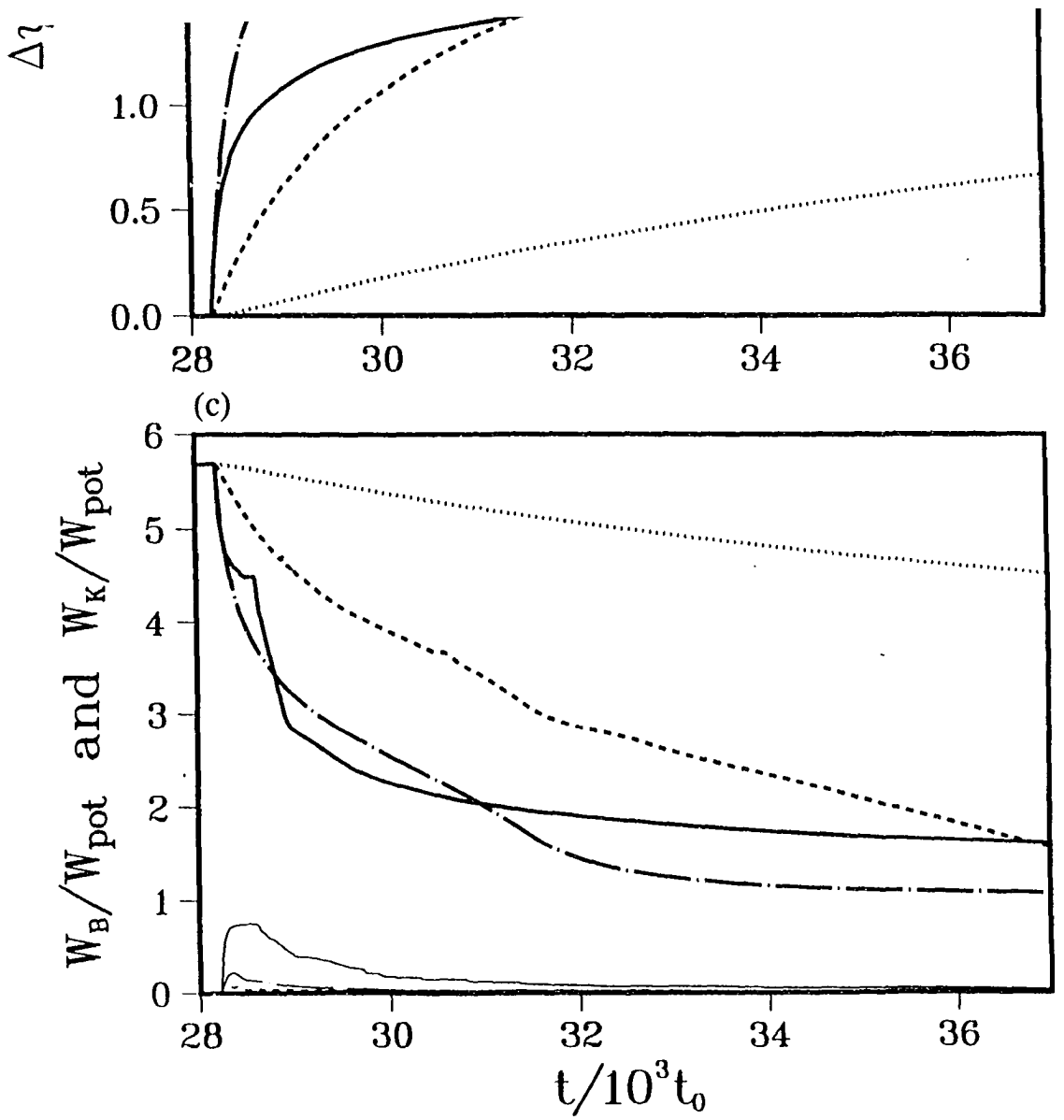

Figure 4.13 Time variation of some physical quantities in Cases 4B, 4C, 4D and 4E. (a) Heights of the O-lines (the upper X-line for Case 4E) shown in thick curves and heights of the X-lines (the lower X-line for Case 4E) shown in thin curves. (b) Reconnected fluxes. Note that the total poloidal flux of the system is 8/3. (c) Magnetic energies shown in thick curves and kinetic energies shown in thin curves. In every panel, the solid line stands for Case 4E, the chain-dotted line for Case 4D, the dashed line for Case 4C and the dotted line for Case 4B.

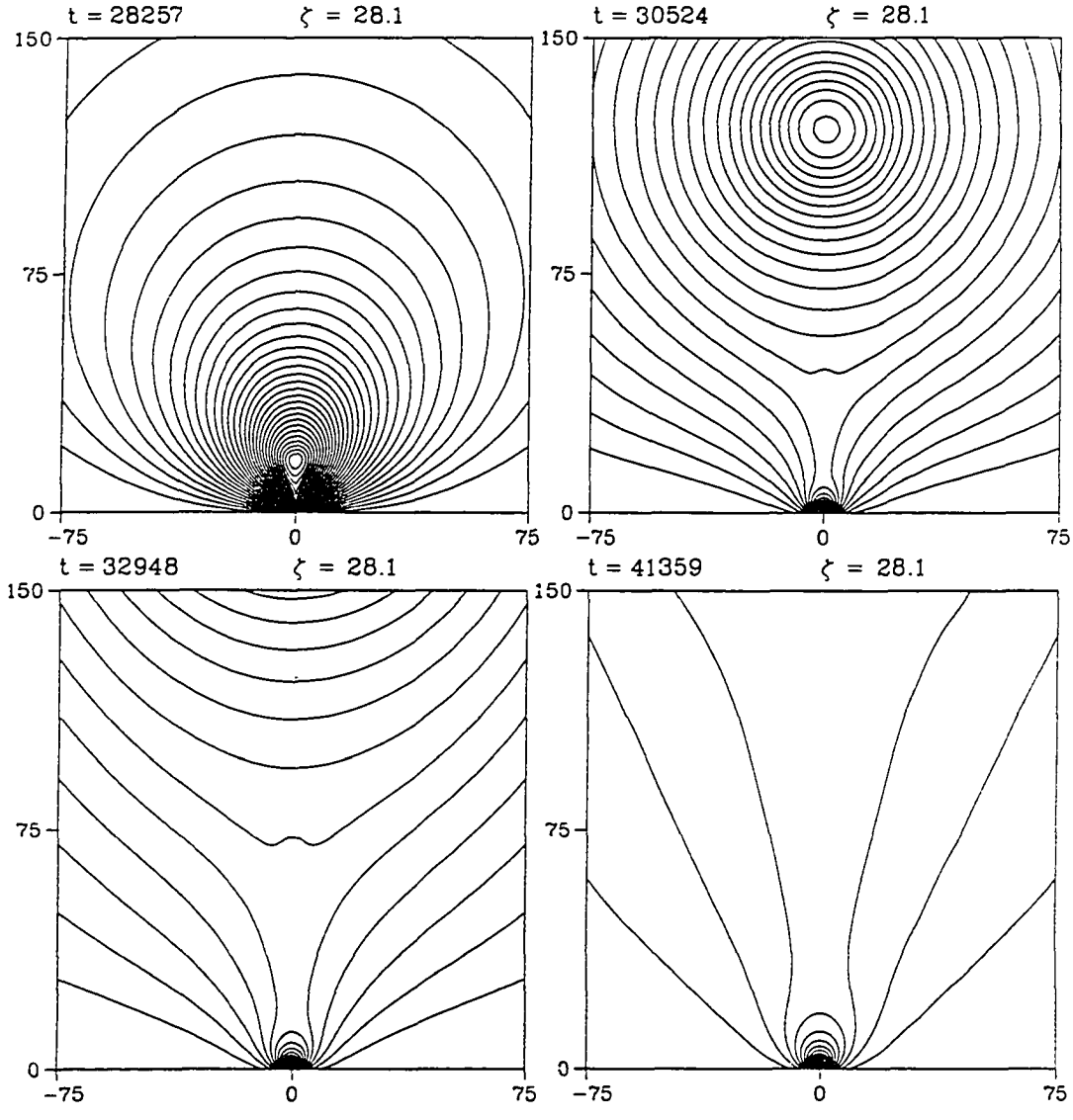

Figure 4.14 The evolution of the magnetic arcade of $\zeta_m = 28.1$ under the uniform resistivity $\eta = 10^{-3}$ applied from $t = 28200\,t_0$ (Case 4D).

This point differentiates our models from other driven reconnection models (e.g., Yan *et al.*, 1992) or spontaneous reconnection models with free boundaries (e.g., Scholer, 1989). The fast reconnection models pioneered by Petschek (1964) assume a small diffusion region compared to the whole reconnection system size. In our models, the extension of the reconnection system in the x-direction is limited to a fraction of the plasmoid size for the aforementioned reason, and the external reconnection rate has meaning only up to this distance. Thus there is not too much difference between the external and the internal reconnection rates. It should be noted that the internal reconnection rate is found to be approximately the Sweet-Parker rate for all the values of resistivity we tested. The Petschek type dependence of the reconnection rate on the magnetic Reynolds number given by

$$(M_e)_{max} = \frac{\pi}{8 \log R_{me}}, \tag{4.7}$$

where $R_{me} \equiv L_e V_{Ae}/\eta$ with the whole system size L_e, is not realized in our simulations. In Case 4D, however, the fast reconnection rate is achieved owing to the fact that the Sweet-Parker rate comes close to the Petschek rate due to the large value of resistivity. Interesting enough, the diffusion region in this case takes such a small length to manage to satisfy the geometric condition for the fast reconnection $l < L_e$.

When comparing our results with existing theories and numerical experiments, the presence of a plasmoid surrounded by line-tied field should be first considered. The plasmoid not only determines the reconnection system size as mentioned earlier, but also make the separatrices emerging from the X-line diverge. Our reconnection system thus comes under the category of nonuniform reconnection with large separatrix angles. It is confirmed from our results that the relative length of the diffusion region compared to the plasmoid height is an increasing function of R_m and the width of the diffusion region is a decreasing function of R_m. This scaling law has been given by the nonuniform theory of magnetic reconnection by Priest and Forbes (1992b)

and is consistent with simulation results by Yan *et al.* (1993). In the solar corona, the resistivity η is typically 10^{-14}, and our results predict that the diffusion region will take as large a length as possible and will be very narrow under uniform resistivity. The Sweet-Parker reconnection rate will then be around the order of 10^{-7}. To achieve fast magnetic reconnection, the diffusion region length must be somehow reduced to a scale much samller than the arcade size. If this can occur, the Sweet-Parker rate will also be increased although not comparable to the fast reconnection rate that will be about 0.01.

4.4.2 Spatially Confined Resistivity

In Case 4E, a nonuniform resistivity is employed, which is given by

$$\eta(J) = \begin{cases} C_\eta (J - J_c)^2 + \eta_B, & \text{if } J > J_c; \\ \eta_B, & \text{if } J \leq J_c, \end{cases} \tag{4.8}$$

where J is the magnitude of current density. The adopted values of parameters are $J_c = 0.1$, $C_\eta = 10^{-5}$, and $\eta_B = 10^{-6}$. It should be noted that the adoption of the above form is intended to confine the diffusion region spatially and not to support any specific anomalous resistivity model. As the maximum current density drops from 10.8 in normalization units in the beginning of the run to 3.3 around the exit of the plasmoid out of the domain and finally to 1.3 at the end of the run, the maximum resistivity is correspondingly reduced from 1.2×10^{-3} to 1.0×10^{-4} and to 1.7×10^{-5} going through all the resistivity levels of Cases 4D, 4C and 4B.

Figure 4.15 shows the field evolution in Case 4E. The most remarkable feature here is that the high speed reconnection flow collimated along the central current layer causes magnetic reconnection within the magnetic island to tear the island into two pieces. A flow channel is thus created from the lower X-line to the upper X-line and the reconnection flow is accelerated through this channel to transfer momentum and flux effectively to the upper X-line. In the

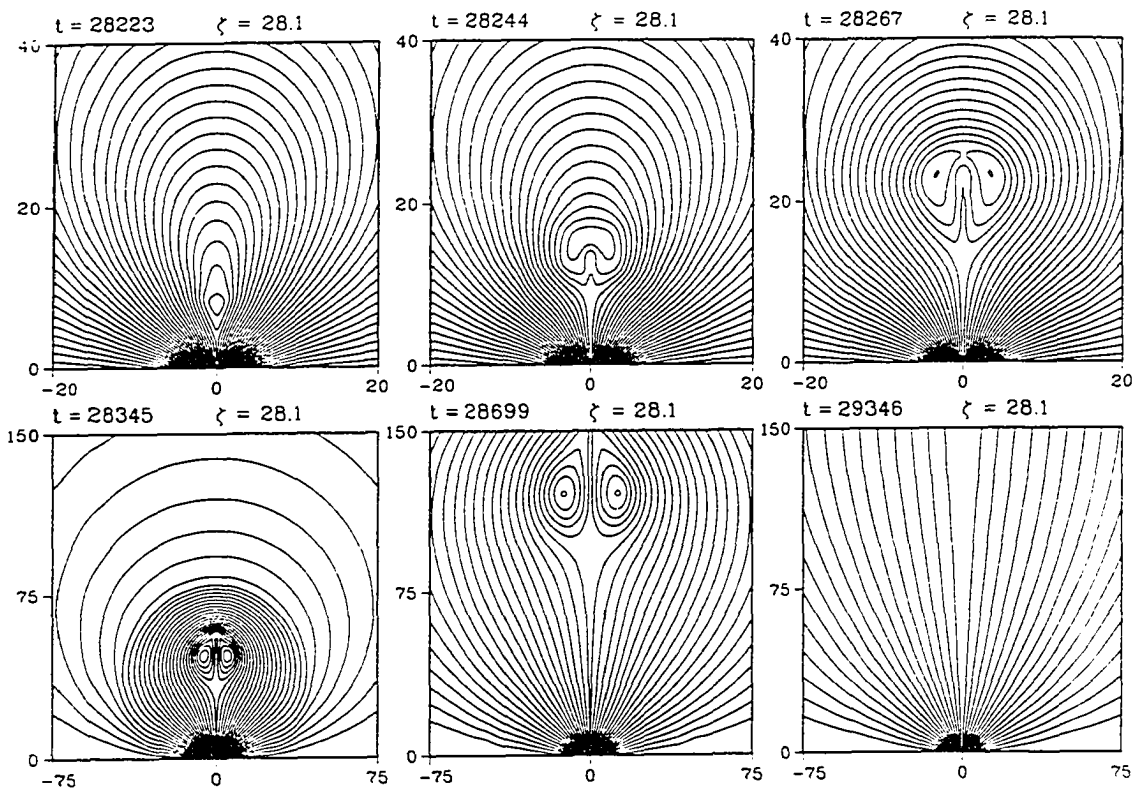

Figure 4.15 The evolution of the magnetic arcade of $\zeta_m = 28.1$ under the nonuniform resistivity given by Equation (4.8) applied from $t = 28200\,t_0$ (Case 4E).

fourth and fifth panel of Figure 4.15, little flux is shown to pile up between the two X-lines, which indicates that the upper reconnection progresses almost at the same pace as the lower reconnection. Since the upper X-line propagates with a higher speed, which is on average $0.33\,v_0$ (see Figure 4.13a), than the center of mass of the whole island system, whose average speed is $0.19\,v_0$, the field line just above the X-line takes a shape like an arrow-head. The propagation speed of the arrow tip is higher than the fast mode speed in the surrounding medium and a fast shock is formed in an arch-shape a distance away from the island system. In the fourth panel of Figure 4.15, the fast shock front is shown as a border between the dense and the tenuous field lines. The upper X-line transits the upper boundary at $t = 28660\,t_0$ and the island system exits from the computational domain around $t = 29050\,t_0$. As seen in the last panel of Figure 4.15, the field lines are partially open at least in the computational domain. In Cased 4D shown in Figure 4.14, most field lines are reconnected to expel the plasmoid system out of the domain and there are only a few field lines open after the plasmoid exit. In contrast to this, only 40 % of the total flux is reconnected to eject the plasmoid system in Case 4E. The rest of flux lifted by the propagating plasmoid forms a partially open configuration. Below we consider the interesting features in Case 4E one by one in more detail.

Usually in magnetic reconnection with large separatrix angles, the slow shock is not so strong and flows accelerated by this shock are occasionally deflected along the field lines (Biskamp, 1986; Yan *et al.*, 1993). The flows emerging from the diffusion region are also instantly decelerated. These features are well manifested in Case 4D (see Figure 4.16). On the contrary, the separatrices in Case 4E keep subtending a very acute angle all the way to near the upper X-line. Yan *et al.* (1992) showed that the magnetic tension force is the major motive for plasma acceleration in the outflow region. In Case 4E, the small separatrix angle maintains a high current density and the near absence of diffusion in the outflow region facilitates an efficient acceleration of plasma by the magnetic tension forces. The maximum flow speed

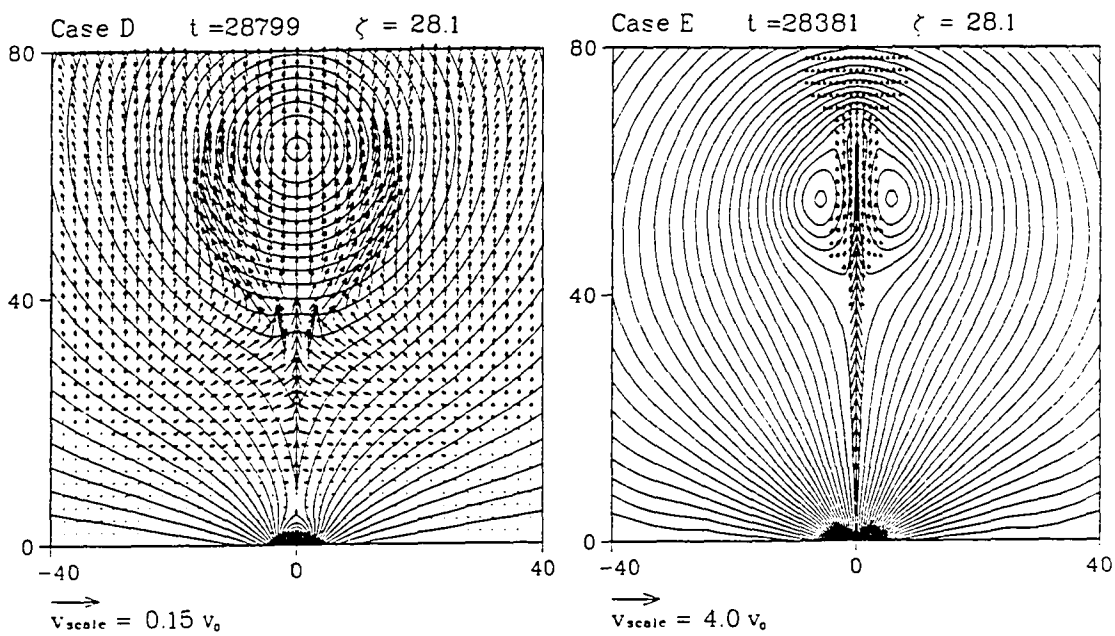

Figure 4.16 Velocity fields superimposed on field lines for Case 4D at $t = 28799\,t_0$ and Case 4E at $t = 28381\,t_0$.

achieved is around $4\,v_0$, which is nearly the upstream poloidal Alfvén speed. The reconnection rate varies from 0.025 to 0.01 while the maximum resistivity drops from 10^{-3} to 10^{-4}. Since the internal reconnection rate is approximately the tangent of the separatrix angle, we have such acute separatrix angles that the shock pair start to be resolved only at some distance above the X-line (see Figure 4.16). Even where the shock pair are not separated, plasma acceleration is not so dulled as would be in a long diffusion region.

Scholer (1989) and Yan *et al.* (1992) showed that the fast reconnection with a small separatrix angle is impossible under uniform resistivity as the diffusion region tends to grow to take the possible maximum length. It may be inferred that the fast reconnection requires a depleting mechanism in the outflow region, which may be either the shock acceleration or the divergence of separatrix angles. If the resistivity in the outflow region is equal to or greater than that near the X-line, the shock acceleration mechanism does not work properply causing flux to pile up upstream of the current layer. In the simulations mentioned above, the normal velocity at the outflow boundary is determined by some extrapolations from the inside. If a high enough outflow speed would be arbitrarily set at the downstream boundary so that plasma and field could be drawn out of the domain by an imaginary sink, a fast magnetic reconnection with small shock angles might be realized even under uniform resistivity. We call for attention of the reconnection researchers to this argument for future studies.

As shown in Figure 4.13b, the reconnected flux per unit time, which will be called reconnection flux rate hereafter, is almost the same in Case 4E as in Case 4D in the initial phase of reconnection, although the reconnection rate in the former is smaller than the latter. This is because the field strength and the Alfvén speed is higher upstream of the current layer in the former. The confinement of high resistivity in the x-direction makes more flux pile up upstream of the X-line and provides a smaller shock angle and a higher outflow speed than the uniform resistivity. In Figure 4.13b, the reconnection flux rates are reduced in all cases after the plasmoid

starts to exit from the domain. The boundary condition using extrapolation is considered to yield outflow speeds mostly slower than are supposed to be and more or less hamper the closing of open field lines after ejection of plasmoids.

In Figure 4.13c, magnetic and kinetic energies are shown for all the cases. In the initial stage, the variation of magnetic energy is almost the same in Cases 4D and 4E whereas the kinetic energy in Case 4E is about three times as much as that in Case 4D. The maximum kinetic energy in the former case reaches about 60 % of the magnetic energy variation. It has been pointed out by Yan *et al.* (1993) that the conversion rate of magnetic energy into kinetic energy is much higher in reconnection systems with small separatrix angles than in those with large separatrix angles. In Case 4E, the decline of magnetic energy is shown to slow down after the steep descent. It is during this phase that magnetic reconnection takes place in the upper X-line. This indicates that the pair of magnetic islands contain more magnetic energy than the original single island. Without the bombardment of high speed flows from the lower X-line, the two islands will coalesce quickly by reconnection (e.g., Biskamp and Welter, 1980). The breaking up of the island is thus a dynamo process and the plateau in the kinetic energy curve corroborates it. After the exit of the upper X-line, magnetic energy declines quickly with the island system being ejected. In this stage, the kinetic energy also decreases with the reconnection flux rate, which suggests that the upper reconnection process also acts as a sink of reconnection flows from below and thus facilitates the reconnection process in the lower part.

Figure 4.17 shows density profiles at $t = 28296\,t_0$ and $28420\,t_0$. The fast shock front propagates a bit ahead with a slightly higher speed than the island system. Across the shock fronts, the downstream-upstream density ratio is $2:1$ in the upper panel and $4:1$ in the lower panel. In the lower panel, three density peaks are evidently resolved; one at the leading edge of the island system and the others within the island pair. In typical observations of coronal mass ejections (CMEs), a closed loop surrounding the coronal cavity is ejected first and the

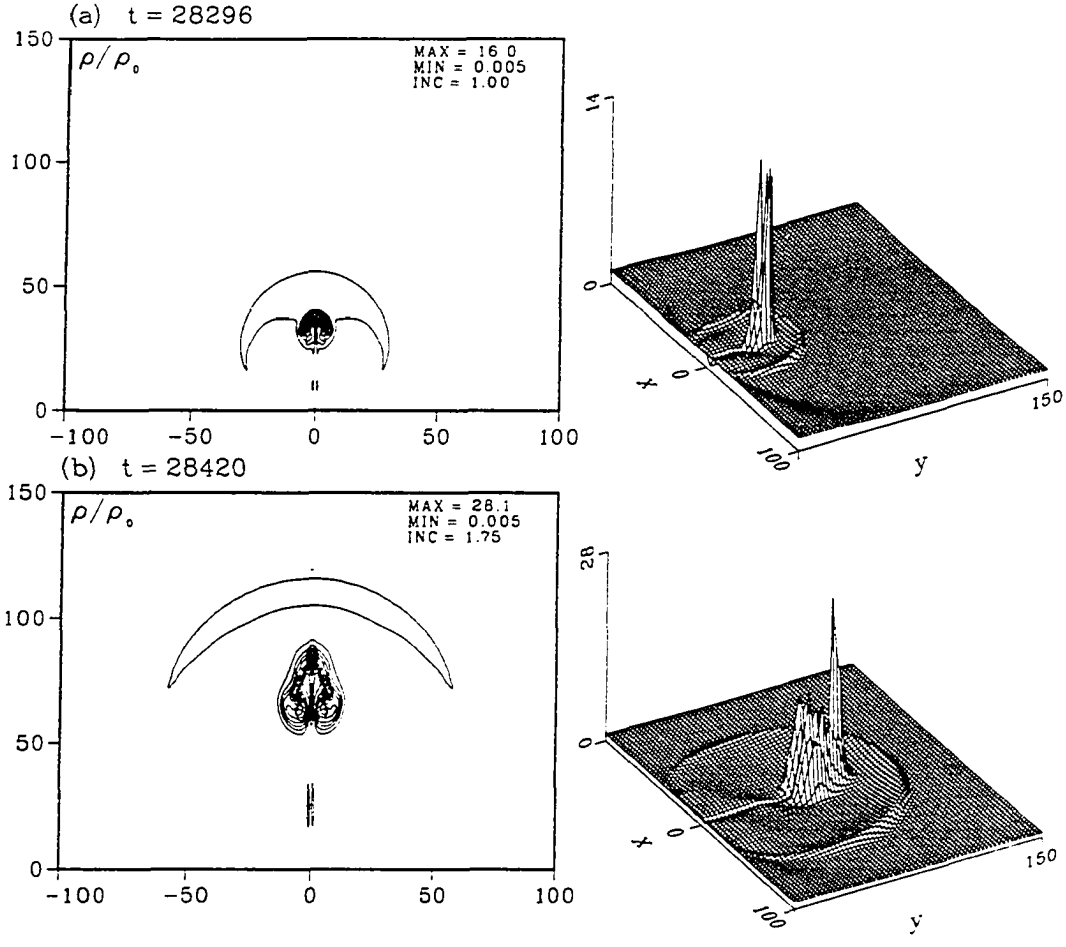

Figure 4.17 Contour and surface plots of the density divided by the density of the static atmosphere. (a) $t = 28296\,t_0$. (b)$t = 28420\,t_0$.

prominence within the cavity follows in a broken shape. After that, the field lines are stretched vertically looking open (for a comprehensive review see Hundhausen, 1995). In our simulation, we originally do not have a prominence in the magnetic arcade, but we can imagine what would happen with the prominence if there were one. If there was a Kippenhahn-Schlüter type prominence before the eruption, the prominence material would reside probably above the field lines which are to be reconnected. When the magnetic island created by the reconnection rises, the concave upward field configuration may be disturbed and the prominence material will little by little slide down sideways along field lines superposed to the rising motion. The prominence then extends from the tip of the island system to the solar surface as usually observed. If a Kuperus-Raadu type prominence has existed before the eruption, the prominence can be broken into two pieces as the reconnection flows tear the magnetic island. In three dimensions, the field lines in the island are possibly connected to the solar surface and the depletion of material along these field lines is expected. Except for these legs connected to the solar surface, the material distribution in this case would be quite similar to what is shown in Figure 4.17. If the X-line is located above the prominence, no prominence eruption will accompany the CME as some observations show (Hundhausen, 1995). In our simulation, the top of the island system propagates with a super-fast speed. However, the super-fast motion of the island system is not necessary for the generation of a fast shock because the fast mode wave generated by a source moving with any speed can be steepened to form a fast shock. In other cases we simulated, we indeed observe the fast wave fronts being steepened although the wave needs to travel a longer distance to form a shock for a slower motion of the island. In this regard, observations sometimes show cases in which the prominence motion is much slower than the frontal loop motion (Hundhausen, 1995). In our simulation, no open field lines are preassumed and only fast shocks are observed. If there are open field lines as in helmet streamers, intermediate and slow shocks can also be created (Steinolfson and Hundhausen, 1990a; 1990b; 1990c). However, even

in an initially partially open field structure, we cannot but think of a fast shock or a fast mode wave structure as long as the CME loop delineates closed field lines.

4.4.3 Other Properties in Arcade Reconnection

Now we look into the time variation of magnetic energies, the driving force of plasmoids and the plasma motion in the z-direction near the X-line.

Figure 4.18 shows the total and partial magnetic energies varying with time in Case 4B. This case is chosen to be shown because the smallest resistivity ($\eta = 10^{-5}$) results in the least redistribution of shear and the least dynamic effects among other cases with $\zeta_m = 28.1$. The decreases in partial energies after the triggering of reconnection are in the order $\Delta W_y > \Delta W_z > \Delta W_x$, where $W_y = \int (B_y^2/2) dV$ (dashed line), $W_x = \int (B_x^2/2) dV$ (dotted line), and $W_z = \int (B_z^2/2) dV$ (thin solid line). Also in all other cases, ΔW_y excels ΔW_x and ΔW_z. However, the above inequality between ΔW_z and ΔW_x is not always true and rather exceptional. When a larger resistivity is applied or when the reconnection has continued long enough, we usually have $\Delta W_x > \Delta W_z$. This trend is considered quite natural, for W_x has no bound while W_z has. In Figure 4.18, it can be seen that

$$W_y \approx W_x + W_z \tag{4.9}$$

as if the magnetic field is force-free. This indicates that the evolution is more or less quasi-static in this case. In Cases 4C and 4D, W_y and $W_x + W_z$ have a discrepancy of up to 10 % while in Case 4E, the equality is far from holding.

After magnetic reconnection is initiated, we can define the plasmoid volume as the volume surrounded by the separatrix with a unit depth in z, which starts and ends at the X-line closing

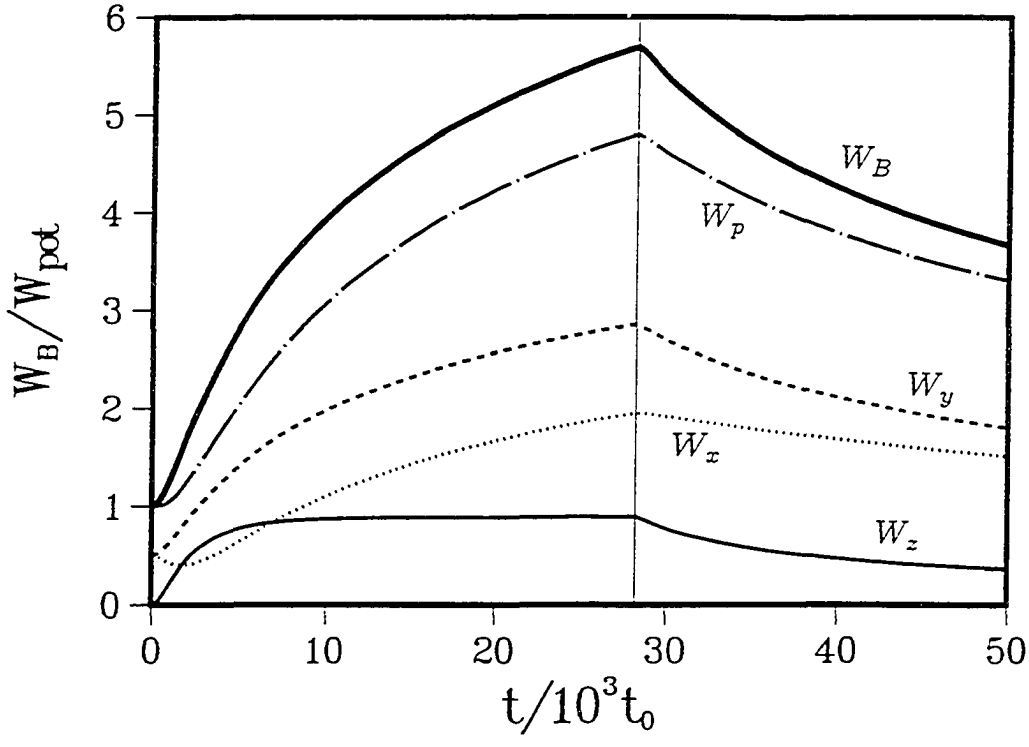

Figure 4.18 Magnetic energy varying with time for Case 4B. The thin solid line represents the toroidal magnetic energy, $W_z = \int (B_z^2/2) dV$, the dotted line $W_x = \int (B_x^2/2) dV$, the dashed line $W_y = \int (B_y^2/2) dV$, the chain-dotted line the poloidal magnetic energy, $W_p = W_x + W_y$, and the thick solid line the total magnetic energy, $W_B = W_p + W_z$. All the energies are normalized in units of the potential field energy. To the left of the vertical line is the same ideal MHD evolution with $V_{z0} = 10^{-3}\, v_0$ that is calculated in Chapter 3. To the right of the vertical line is the resistive evolution with $\eta = 10^{-5}$ and $V_{z0} = 0$.

itself. The force acting on the plasmoid is given by

$$\mathbf{F} = \int \nabla \cdot \mathbf{T}\, dV - \int \rho g \hat{\mathbf{y}}\, dV \tag{4.10}$$

where

$$\mathbf{T} = \mathbf{BB} - \left(\frac{B^2}{2} + p\right)\mathbf{I} \tag{4.11}$$

is the Maxwell stress tensor in a broad sense including plasma pressure. As our interest lies in the upward acceleration of plasmoids, we will concentrate on the magnetic and pressure forces only. Using the divergence theorem, the first term on the righthand side of Equation (4.10) can be written as

$$\begin{aligned} \mathbf{F}_\mathbf{M} &\equiv \int \nabla \cdot \mathbf{T}\, dV \\ &= \int \hat{\mathbf{n}} \cdot \mathbf{BB}\, dS - \int \hat{\mathbf{n}} \left(\frac{B^2}{2} + p\right) dS, \end{aligned} \tag{4.12}$$

where dS is a surface element and $\hat{\mathbf{n}}$ is the unit vector outward normal to the surface. Since the separatrix itself is a flux surface the first term in the second line in Equation (4.12) vanishes, which means that the magnetic tension exerts zero net force on the center of mass of the plasmoid. A little care must be taken in interpreting this statement. In a plasmoid, the largest force is exerted in the reconnection outflow region, where the magnetic tension force overwhelms other component forces. In the rest part of the plasmoid, the magnetic tension force is directed in such a way to offset the upward magnetic tension force in the lower part of the plasmoid. In that part, however, other component forces (mainly magnetic pressure force) are comparable to the magnetic tension force and the net local force is not so large as in the reconnection outflow region. Therefore, it is not too wrong to attribute the upward acceleration of the plasmoid to the magnetic tension force in the reconnection outflow region.

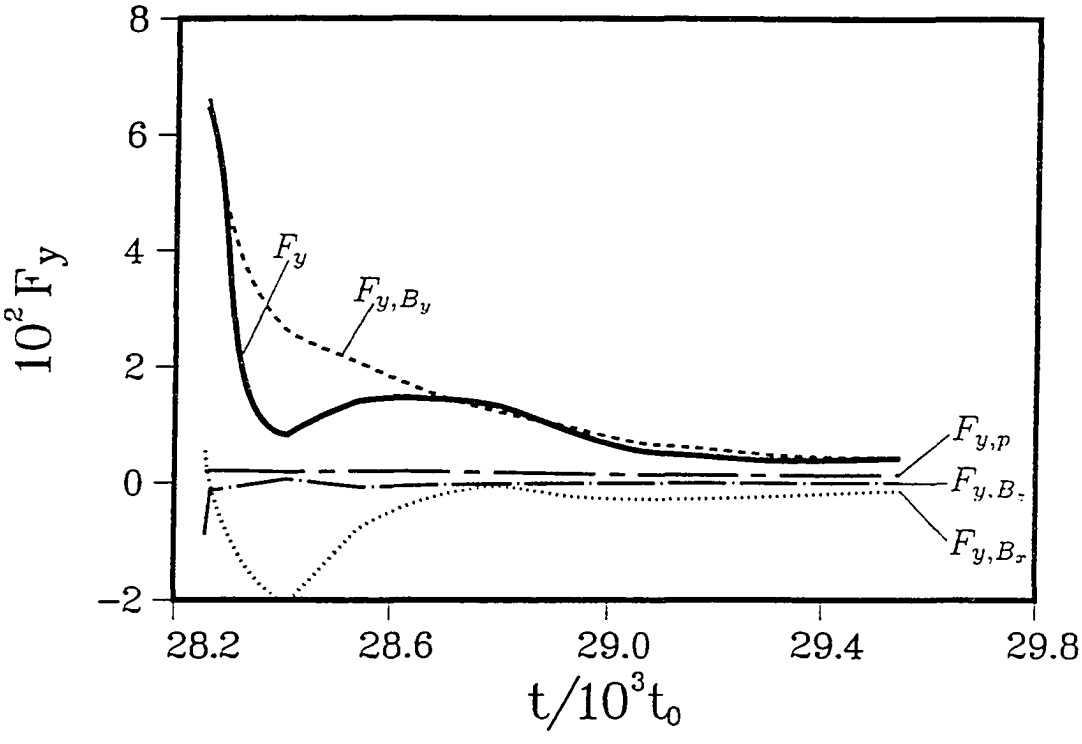

Figure 4.19 Integrated forces in the y-direction acting on the plasmoid slab of unit z-depth versus time. The dotted line denotes $F_{y,B_z} = \oint (B_x^2/2)\hat{\mathbf{x}} \cdot d\mathbf{l}$, the dashed line $F_{y,B_y} = \oint (B_y^2/2)\hat{\mathbf{x}} \cdot d\mathbf{l}$, the chain-dotted line $F_{y,B_z} = \oint (B_z^2/2)\hat{\mathbf{x}} \cdot d\mathbf{l}$, the chain-dashed line $F_{y,p} = \oint p\mathbf{x} \cdot d\mathbf{l}$, and the thick solid line the total force $F_y = F_{y,B_x} + F_{y,B_y} + F_{y,B_z} + F_{y,p}$. All the quantities are normalized to $F_0 \equiv \rho_0 L_0 v_0^2$.

The y-component of the magnetic and plasma pressure force acting on the plasmoid slab of unit z-depth is

$$\begin{aligned} F_y &= \oint \left(\frac{B^2}{2} + p \right) \hat{\mathbf{x}} \cdot d\mathbf{l} \\ &= \oint \frac{B_x^2}{2} dx + \oint \frac{B_y^2}{2} dx + \oint \frac{B_z^2}{2} dx + \oint p \, dx \\ &= F_{y,B_x} + F_{y,B_y} + F_{y,B_z} + F_{y,p} \end{aligned} \tag{4.13}$$

where the integration path is closed along the separatrix counterclockwise on the x-y plane. Each component force in Equation (4.13) is shown against time in Figure 4.19 along with the net force F_y. The curves extend from $t = 28257\,t_0$, which is $55\,t_0$ after the triggering of reconnection, to $t = 29554\,t_0$ shortly before the top of the plasmoid touches the upper boundary. The unit of the force per unit z-length is $F_0 \equiv \rho_0 L_0 v_0^2 = 6.0 \times 10^{11}\,\mathrm{dyne\,cm^{-1}}$. The major contribution to the upward force comes from F_{y,B_y}. This means that nearly vertical fields packed upon the lower tail of the plasmoid is the main motive for upward acceleration of the plasmoid. In a different point of view, the condition for a large F_{y,B_y} is also the condition for a small separatrix angle and a strong current layer, which can result in large magnetic tension force. Except for a very short time after the triggering of reconnection, F_{y,B_x} is negative because the magnetic field strength is generally a bit higher in the upper part of the plasmoid than in the lower part, not to speak of the reconnection outflow region. The force by the toroidal field pressure, F_{y,B_z}, is initially negative due to the depletion of the toroidal flux by the sudden start of reconnection, then rises to just above zero and keeps a negligible value of the order of $10^{-5}\,F_0$. This means that that B_z is roughly constant along the separatrix field line in this case. The plasma pressure force, $F_{y,p}$, is decreased from $2 \times 10^{-3}\,F_0$ to $1.3 \times 10^{-3}\,F_0$ at a constant rate. The gravitational force acting on the plasmoid is approximately matched by $F_{y,p}$ initially, but is doubled at the end of the time covered. Although the mass of the plasmoid is increased to seven times the initial value, the increase in height of the center of mass results in reduction of gravity to a third.

In the case shown, the magnetic field upstream of the X-line is reduced to about half and F_{y,B_y} is decreased correspondingly, but the reconnection rate remains almost unchanged. It can be thus said that keeping a high reconnection flux rate, not merely a high reconnection rate, with a small separatrix angle is most important in the energetic ejection of plasmoids.

In reconnection processes, the differential flux volume generally diverges in the X-line and yet the toroidal field B_z as well as mass density is finite in the X-line. In other words, the differential toroidal flux, which is nothing but the distance between the conjugate footpoints or the actual shear, is infinite in the X-line in our 2-D picture. The magnetic field lines entering the diffusion region is thus expected to be tilted to align themselves along the z-axis. To see this, we have plotted the field lines and the contours of v_z at $t = 28257\,t_0$ and $t = 29174\,t_0$ in Case 4D. The shearing motion we gave before the diffusion is in the negative z-direction for $x < 0$ and in the positive z-direction for $x > 0$ (see Equation (3.30)). In the neighborhood of the X-line shown in the figure, v_z is indeed directed in the same way as the original shearing pattern to increase magnetic shear. Interesting enough, this shearing velocity pattern is extended to the reconnection outflow region downstream of the slow shocks. The study on the reconnection layers by Lin and Lee (1994) has demonstrated the presence of a pair of rotational discontinuities, when $\eta = 0$, or intermediate shocks (IS), when $\eta \neq 0$, outside the slow shocks (SS). In our case, however, IS and SS are not resolved and we hereafter call this unresolved composite layer IS-SS. Across the IS-SS, the toroidal magnetic field and the plasma pressure increase while the poloidal field decreases. Downstream of the IS-SS, the z-velocity is directed parallel to the original shearing motion to increase B_z. Upstream of the IS-SS, a fast mode expansion structure is present and the toroidal field as well as the plasma pressure decreases approaching the current layer from farther outside. The z-velocity is thus antiparallel to the original shearing motion in this region. The IS-SS thus appears as a velocity-shear layer. The upper panels in Figure 4.20 represent the initial reconnection phase, where the shock angle does not diverge much and most part of the

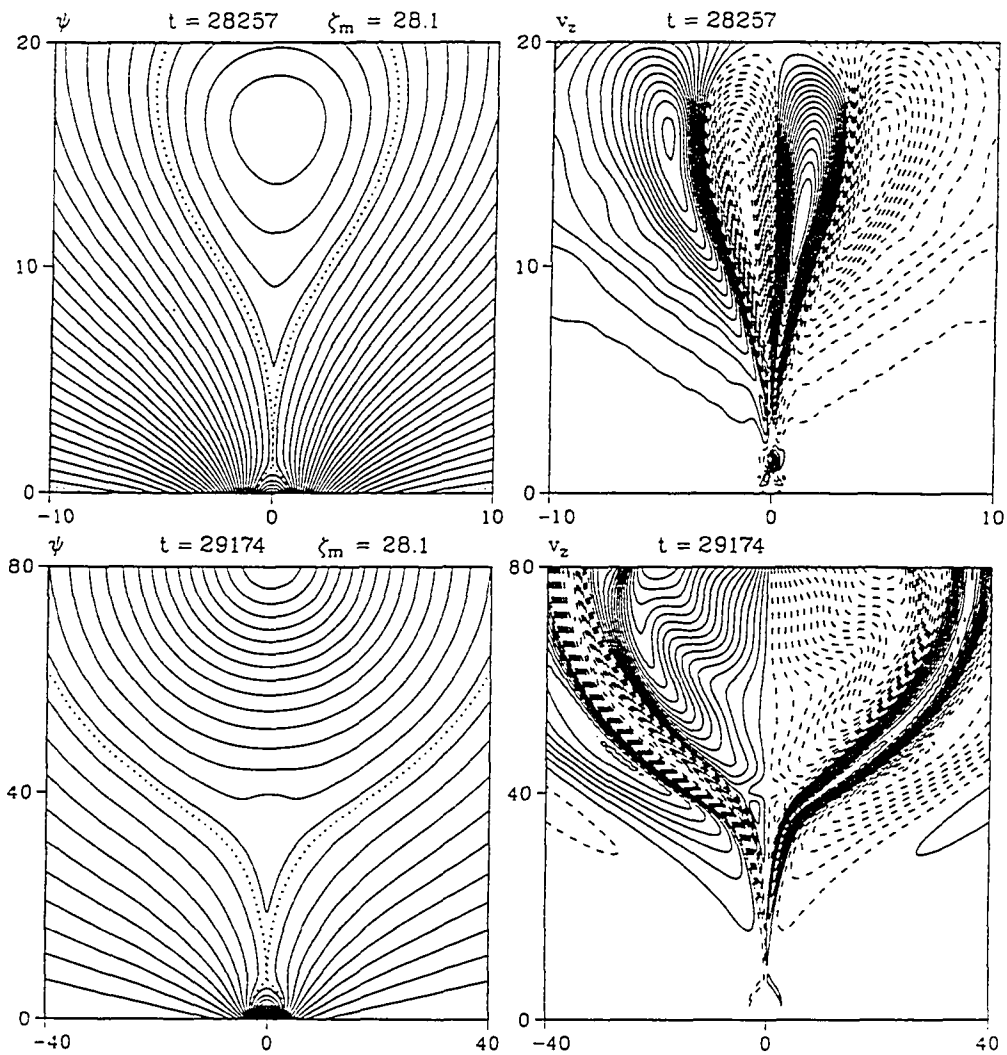

Figure 4.20 Magnetic field lines and contours of v_z at two different times in Case 4D. The dotted line in the field line plots is drawn along the separatrix. In the v_z contours, the dashed lines are for negative values and the solid lines are for positive values.

plasmoid is under acceleration. In the later stage shown in the lower panels, reconnection flows are diverted sideways along field lines and the plasmoid is under expansion. Just upstream of the IS-SS, the z-velocity is so directed as to increase B_z. Inside this envelope, the expansion of the plasmoid unshears the magnetic fields. The line-tied field system below the X-line in general is taken away the toroidal flux by a reconnection process which transports the toroidal flux to the magnetic island. Thus the magnetic shear in the photosphere is reduced except near the feet of separatrix field lines. Observations by Wang *et al.* (1994), however, show that photospheric magnetic shear was increased after some flares. It issues a great challenge to the reconnection paradigm of solar flares. To accommodate the observations to the reconnection picture of solar flares, we may speculate several possibilities. Sheared magnetic fields may somehow emerge from below the solar surface at the time of solar flares. This argument requires confirmation by observation. If the flux emerging is timed just before the flare onset, it can be considered as a cause of the flare, but if the emerging is timed simultaneously with or just after the flare onset, flare theories still need to answer the question how flares can pull out the subphotospheric fields. Without assuming such external changes as above, we can naively think that the reconnection X-line is located at or near the photosphere. This is, however, very unlikely since flare loops are observed in the corona. Another speculation is that the shock pair below the X-line may be extended down to the photosphere subtending a small angle. This is also unlikely to happen since the photosphere is a very rigid surface compared to the solar corona. This problem thus requires either another mechanism of solar flares such as dynamo theories (e.g., Kan *et al.*, 1983) or further investigation of reconnection processes in three dimensions (e.g., Priest and Forbes, 1992a).

4.5 Summary and Discussion

In this chapter, we have studied the resistive evolution of pre-sheared magnetic arcades in a 2-D Cartesian geometry. We find that there is a critical value of shear, beyond which magnetic reconnection can take place under resistivity and a magnetic island (or plasmoid) can be formed. Interestingly, this critical value of shear nearly coincides with the starting point of the third phase in the ideal MHD evolution discussed in Chapter 3. The reconnected field configuration is found to approach a linear force-free field asymptotically as reconnection continues.

In field configurations where $dB_z/d\psi > 0$, the diffusion of the toroidal magnetic field leads to steepening of the shear profile and thinning of the current layer. In contrast, the diffusion of the poloidal field can result in current layer thinning, only if the shear exceeds a certain critical value, which is related to the critical shear for magnetic reconnection. In the development of a current layer by diffusion, the transport of the toroidal flux across the field lines plays a key role. Where the toroidal flux flow is stagnant in ψ-space, a thin current layer develops. During this process, some inner field lines are shown to be dipolarized while outer field lines are stretched upwards.

In magnetic reconnection processes in an arcade-like geometry, the extension of the reconnection system is limited by the size of the magnetic island. There is thus no big difference in the external and internal reconnection rates unless the width of the diffusion region is very small compared to the plasmoid size. The internal reconnection rate is found to be scaled with the Sweet-Parker rate. To increase the reconnection rate, either resistivity needs to be raised or the length of the diffusion region must be reduced. Under uniform resistivity, the relative length of the diffusion region compared to the plasmoid height grows and the width of the diffusion region decreases with the increasing magnetic Reynolds number. In the case with a highest uniform resistivity ($\eta = 10^{-3}$) we tried (Case 4D), the Sweet-Parker rate is comparable to the Petschek

rate and the diffusion region length is relatively small. The presence of a large plasmoid, however, creates a large separatrix angle and diverts the flows along field lines. After the plasmoid is completely ejected out of the computational domain, not much flux remains unreconnected. We have also tried a current-dependent resistivity to confine the diffusion region. In this case (Case 4E), the reconnection rate is smaller, but the reconnection flux rate is almost the same as in the former case. The reconnection outflows are highly collimated to cause magnetic reconnection within the magnetic island. Owing to the flow channel thus created, the shock angle is kept small and a high conversion rate of magnetic energy into kinetic energy is achieved. The fast shock front generated by the super-fast motion of the plasmoid tip resembles the observed CME loops, which propagate ahead of a prominence of a broken shape. After the ejection of the plasmoid, a considerable portion of the flux still remains unreconnected forming a partially open configuration.

Our numerical model in Case 4E accommodates many outstanding features in CME observations. Recently Uchida (1995) has reported that soft X-ray images obtained by Yohkoh SXT reveal CME structures resembling a spine and ribs. The density distribution within the plasmoid system in our model has three peaks and a 3-D view of this structure would be similar to what is observed by Yohkoh SXT. With all this consistency, the reconnection model of CMEs still has to cope with a few fundamental problems brought up by observations. First of all, the launch time of CMEs inferred from coronal observations usually falls about 10 minutes before the flare onset characterized by hard X-ray bursts (Hundhausen, 1995). If the reconnection is triggered in a rather static corona as in our model, the launch of a CME and the onset of a hard X-ray flare must be simultaneous. For the reconnection model to survive that inconsistency, the magnetic field needs to rise a little before the magnetic reconnection. In this regard, Livi *et al.* (1989) have reported that flux cancellation is often observed before the flare onset. Flux cancellation might be explained as submergence of fluxes reconnected in the corona. However, any

coronal reconnection would reveal flare-like signatures, over which no observation is reported. Thus flux cancellation can be best described as emergence of an island-like structure which was dipped in the photosphere and pushed up by subphotospheric reconnection. It does not seem to be important whether flux cancellation results in a catastrophe in the filament equilibrium (Forbes, 1990a; 1991) or not. Without resistivity, even an unstable flux rope cannot rise much. Whether the rising is fast or slow, the current layer is stretched and becomes more vulnerable to reconnection than before the rising. The rest scenario would be just the same as our model. Another important problem is provided by Wang *et al.*'s (1994) observation of the magnetic shear increase after the flare onset. This observation challenges not only reconnection pictures but also the conventional view of field opening up because the toroidal field would propagate away to infinity along the open field lines. As mentioned earlier, a further investigation is needed on the geometry of the 3-D reconnection.

CHAPTER 5

Summary and Discussion

The present thesis has attempted to explain formation of solar prominences and solar eruptive processes, which encompass prominence eruption, coronal mass ejections and flares, as responses of the solar corona to photospheric motions. In the ideal MHD condition, which is valid in the most part of the solar atmosphere at most times, the coronal evolution is driven up to the critical point which generally involves thin current layers. It is believed that the dramatic manifestation of the above phenomena is caused by reconnection of magnetic field lines. Even without resistivity, an abrupt change in field configuration conserving the topology can result from an ideal MHD instability or nonequilibrium, but such a change generally results in a singular current sheet where magnetic reconnection will eventually take place.

Flaring active regions usually involve prominences. Throughout their life, prominences tend to ascend (Zirin, 1988) and finally erupt during CMEs and/or flares. One of the major photospheric conditions for prominence formation, which is also the condition for prominence eruption, CMEs and flares, is the increase of magnetic shear (Martin, 1990). It is thus thought that all the aforementioned solar phenomena lie in one evolutionary track of an active region which undergoes distortion of its magnetic fields. In this thesis, we could not cover the whole evolutionary sequence of an active region in one simulation because temporal and spatial scales to be resolved and to be encompassed are very different for each of the events to focus on. By employing similar boundary motions, we have implicitly shown that all the events created in our simulations are possibly located in one evolutionary sequence. On the other hand, by setting up a different environment within the computational domain for each simulation we have constructed a cause-effect relationship for individual events.

Throughout the present study, we implement "magnetic shear" by "velocity shear" at the photospheric boundary. If there is little flux transport between above and below the photosphere, the magnetic shear must come from shear-increasing motions, which include shearing motions parallel to the neutral line and converging motions towards the neutral line. However, shear-inducing photospheric motions are not so frequently observed as magnetic shear (Martin, 1990). As an alternative to shearing motions, we can also imagine that the emergence of a pre-sheared field results in an increase of magnetic shear. Whether magnetic nonequilibrium or resistive reconnection is concerned, the magnetic shear has much more significance than the shearing motion. The latter is merely a way to increase magnetic shear. This is also true in all our numerical models except Case 2A and our use of shearing motions as a method of increasing magnetic shear is thus justified.

In Chapter 2, three different mechanisms of prominence formation are discussed. In all three cases, only boundary motions are given as external perturbations and the emergence or submergence of flux is not addressed. Our study is distinguished from other numerical studies on prominence formation in that we do not assume artificial mass supply (Wu *et al.*, 1990) or isobaric perturbations of unknown origin (Drake *et al.*, 1993). Our models are regarded to have general validity in the Sun.

In Case 2A, the growth of the radiative cooling is preceded by the adiabatic cooling caused by the rapid expansion of the magnetic field. The onset of thermal instability in this case is restricted by the expansion speed and the original density. A high shearing speed ($\gtrsim 1\,\mathrm{km\,s^{-1}}$), however, is not a necessary condition for the formation of prominences of this type. Not only the field undergoing footpoint shearing but also the flux tube emerging from below the solar surface will expand into the corona. Newly emerging fluxes also can carry up high density material into the corona although they are like leaky buckets. In our 2-D model, the formation of dips on field lines is possible for a relatively high plasma β ($\gtrsim 0.1$). In 3-D, we are relieved from

this restriction since 3-D force-free fields can have concave upward curvature (Antiochos *et al.*, 1994). Therefore, the mechanism in Case 2A can work quite generally where a quick increase in magnetic shear arises no matter where it comes from.

In Case 2B, the thermal instability is caused by the high density plasma inside the magnetic island created by magnetic reconnection. Along the reconnection outflows, plasma undergoes compression and the temperature in the magnetic island is higher than in the upstream region. Once plasma is confined in the island, there is no more adiabatic heating and the temperature is decreased by the radiative cooling. In our model, magnetic reconnection is allowed to occur only above the bottom boundary, i.e., only in the corona, but the reconnection involved in the real process of prominence formation is likely to take place in or below the photosphere. If reconnection takes place above the photosphere, a flare-like phenomenon will be observed during the prominence formation, which, however, is never reported. The subphotospheric reconnection picture can solve other problems which can be raised by the coronal reconnection picture. Firstly, it can explain how some prominences have as large a mass as the whole corona. Secondly, too high a location of the prominence can be avoided. Thirdly, prominence formation is not restricted by the cooling time-scale, which is unreasonably long if density at the coronal base is $10^{-8}\,\mathrm{cm}^{-3}$ or lower. Since prominence formation is more difficult with coronal reconnection than with subphotospheric reconnection, our model gives a sufficient proof of the validity of the mechanism, in which the high density material trapped in the magnetic island effects thermal instability. For future studies, 3-D effects are of particular interest because the magnetic island would not be completely detached from the photosphere in 3-D. In that case, the field topology would not be different from that of Kippenhahn-Schlüter type prominences. The flows along the prominence field lines and their effects on prominence stability need to be studied further.

In Case 2C, two colliding bipolar arcades are modelled, between which a current layer is inevitably formed. The stagnation of reconnection outflows some distance above the X-line results in thermal instability and prominence formation. In this case also, subphotospheric reconnection is more favorable to formation of a prominence than coronal reconnection for the same reasons as mentioned above. It is most interesting that this model accommodates parallel and antiparallel transverse magnetic fields across the polarity inversion line. In terms of footpoint motions, the former can be created by antiparallel shearing motions and the latter by parallel shearing motions at feet of adjacent arcades. In the latter case, the magnetic field piercing the prominence can hardly have a toroidal component, which prevails over the poloidal component in reality, if most prominence material resides above the X-line. In our simulations, condensation first takes place above the X-line, but the neighborhood of the X-line is later permeated by condensed material. The observed prominences of the latter type are thus likely to be located next to the X-line. In this regard, Athay *et al.* (1985) deduced such an antiparallel prominence field structure from the dynamic behaviour in the transition region. The prominences modelled in Case 2C are topologically of Kippenhahn-Schlüter type, but observationally of inverse polarity. According to our unreported numerical experiment, the transition to the Kuperus-Raadu geometry is possible only when the dipped field lines are well held down by a large mass. Even if this can happen in reality, antiparallel fields are not acceptable in the Kuperus-Raadu geometry. Furthermore, the distinction between KS and KR geometries is of little meaning in 3-D as mentioned earlier.

In Chapter 3, we have studied quasi-static evolution of a magnetic arcade under footpoint shearing. Three distinct phases are found in the evolutionary sequence. In the first phase, the arcade expansion is mild and the toroidal field and the current density increase. In the second phase, the arcade expansion is more or less self-similar gaining greater speed, and the toroidal field strength starts to decrease, while the maximum current density changes little. In the third

phase, the arcade expansion is the fastest among all three phases and a current layer develops and grows conspicuously with increasing shear. The field configurations initially approximate linear force-free fields, but are far from linear force-free states in the later stage. We have also constructed force-free field solutions by the magneto-frictional method. The field lines in the force-free fields are generally more stretched outward than the low β quasi-static solutions for the same shear. Mikić and Linker (1994) also found no field-opening behaviour in the finite β time-dependent solutions while a partially open configuration is obtained in the zero-β case. This is attributed most of all to the fact that the plasma β is no lower in the outer part of the model coronae than in the outer part of the solar corona. It thus goes too far to explain the whole CME process with magnetic nonequilibrium only. The current density maximum in the current layer bifurcates into two branches a little bit above the bottom boundary. The footpoints of the current density maximum get closer as shear increases. It can be inductively inferred from the numerical results that the force-free field asymptotically approaches the fully open configuration as shear increases indefinitely in 2-D Cartesian geometry. In spherical geometry force-free fields open up partially for a finite shear as shown by Mikić and Linker (1994) and Roumeliotis *et al.* (1994), but we think that the fully open configuration is also an asymptotic state unless the shear profile is discontinuous at the polarity inversion line as in Lynden-Bell and Boily (1994). Since opening up of field lines is considered to be difficult in a finite β plasma regardless of the geometry, the results of our 2-D Cartesian simulations are regarded to have quite a general validity.

In Chapter 4, we have investigated the resistive evolution of a pre-sheared arcade in a 2-D Cartesian geometry. It is found that there is a critical amount of shear, over which the current density in the current layer is increased in the presence of resistivity and magnetic reconnection can be triggered. Since the reconnected field configuration contains a magnetic island, this critical value is related to the bifurcation points suggested by Aly (1990) and Kusano (1995).

As reconnection is continued, the toroidal flux is redistributed across flux surfaces and the field asymptotically approaches linear force-free states.

The transport of toroidal flux across field lines by diffusion and the responsive motion of field lines either enhance or decrease the current density in the current layer. Where the toroidal flux flow is stagnant in the flux function space, the current density is enhanced. Diffusion of the toroidal field is found to eventually contribute to enhancement in current density, whereas diffusion of the poloidal field is found to do so only above a critical value of shear. An interesting subject for further studies is the current sheet formation in the corona due to higher resistivity in the photosphere. Photospheric magnetic fields are rather concentrated in small-scale structures and the conjugate feet of the current layer are generally not located close to each other. Therefore diffusion in the thin photosphere does not necessarily mean magnetic reconnection, but can create a singular current sheet in the corona, where magnetic reconnection may be triggered.

In the solar corona, magnetic reconnection in a single flux system is a spontaneous process whereas reconnection between separate flux systems is rather a driven process. In an arcade-like geometry, fast magnetic reconnection does not seem to occur unless the diffusion region is confined to a very small region. Even though this condition is satisfied, it is doubtful if the fast magnetic reconnection rate can be sustained until all the flux is reconnected. This is because dynamics of the line-tied field lines surrounding the plasmoid are mostly governed by the global force balance, not so much by the reconnection process. In resistive evolution of a magnetic arcade under different resistivities, the internal reconnection rate is found to be scaled approximately with the Sweet-Parker rate. Reconnection can be fast only when the Sweet-Parker rate comes near the Petschek rate because the upstream range over which the reconnection process exercises its influence is not so long. In two cases, we have obtained a rather fast reconnection rate; one with the highest resistivity (Case 4D) and the other with a current-dependent resistivity (Case 4E). The reconnection rate is higher in Case 4D, whereas

the reconnection flux rate is almost the same in both cases. The latter case thus have a smaller shock angle and attains a higher conversion rate of magnetic energy into kinetic energy than the former case. The highly collimated flows in Case 4E tear the magnetic island and create a flow channel, which contributes to keeping a small shock angle. To expel the plasmoid out of the computational domain, almost the entire flux needs to be reconnected in Case 4D, while less than half the total flux is needed in Case 4E. In this case, a partially open configuration is realized at least in the computational domain. In Case 4E, all major features of CMEs are reproduced, i.e., the fast shock front resembling the CME frontal loop, three density peaks in the island system similar to a broken prominence and the partial opening of field lines.

In the numerical study by Mikić and Linker (1994), there was no opening up of field lines in the ideal MHD evolution of a finite β plasma as in our ideal MHD model in Chapter 3. The reconnection model by Mikić and Linker (1994) is rather close to our Case 4D. Our model in Case 4E provides an account for opening of field lines in a finite domain which corresponds to the field of observational instruments.

Since the conditions for prominence formation and eruption in our models are the magnetic shear in the same way, it naturally comes into question when one of the above event takes place, not the other. In our unreported studies, Kuperus-Raadu type prominences tend to rise more actively as more flux is transported to the magnetic island. Once an X-line is formed above the photosphere, the increase in shear in the unreconnected flux outside the island inevitably leads to further magnetic reconnection. If the X-line is below the photosphere, the increase in shear as well as the subphotospheric reconnection give impetus to rising of the magnetic island. In any case, when the magnetic island rises more vigorously, the current layer below the island becomes longer and thinner so that there are more chances of fast reconnection. In quiet regions, a slow reduction of the photospheric flux possibly due to subphotospheric reconnection, rather than further increase in magnetic shear, is thought to be responsible for an eruptive process.

In active regions, a rapid increase in magnetic shear as well as flux cancellation can excite an eruptive process. The life of prominences is thus shorter in active regions than in quiet regions.

Our simulation model suggests that CME, prominence eruption and a flare are different manifestations of a single global process and none of those phenomena can be either a cause or an effect of another. However, it must be clarified whether reconnection plays a key role in CMEs as in our model or it is just a result of the current sheet formed after the CME loop and the prominence are ejected. The latter picture was supported by Hundhausen (1994) referring to the observation that the inferred CME launch time is about 10 minutes ahead of the hard X-ray burst. During this time gap, however, the cavity top had moved only a small distance and then the reconnection was probably triggered. Such a rising of the arcade top can be explained in many ways. As seen in Chapter 3, even the quasi-static arcade expansion becomes faster as shear increases. If there is a subphotospheric reconnection as suggested by flux cancellation, the whole arcade system will rise up. If the subphotospheric reconnection causes a sudden loss of equilibrium as in Forbes (1990a) and Forbes and Isenberg (1991), the rising will be more violent, but will not last indefinitely under the frozen-in condition. Anyway, there can be diverse ways to account for the initial motion of the cavity top. Putting aside the flare, the CME only needs a lot of energy to expel mass against the solar gravity. The magnetic nonequilibrium, which is conventionally regarded to be responsible for the field opening, is not an energy-releasing process. Here the change of configuration from the closed field to the open field is effected by an infinitesimal increase of shear, which means an infinitesimal energy input. Without reconnection, the kinetic energy involved in CME can hardly be explained. In this regard, our model rather agrees with the catastrophe-reconnection hybrid scenario proposed by Forbes (1991).

In summary, we have studied prominence formation and solar eruptive processes using MHD simulation. Three different mechanisms of prominence formation are presented. The

quasi-static evolution of magnetic arcades is discussed with emphasis on development of a current layer. A reconnection model of solar eruptive processes is established, which explains principal signatures involved in CMEs.

APPENDIX A

Numerical Algorithm for the Simulation of Prominence Formation

The purpose of this appendix is to give a detailed explanation of the numerical scheme used in solving Equations (2.1)–(2.5) governing the process of prominence formation. The numerical methods employed in other chapters are slight modifications of the one described here. In different versions of the numerical codes, the momentum equations are formulated either in conservative forms or in non-conservative forms. The latter are used when the time-evolution is rather slow and smooth while the former are used when shocks and other discontinuous structures need to be resolved. For convenience's sake, only a description based on non-conservative forms is presented here.

Without the heat source terms (terms including H and C) and the thermal conduction term, the governing equations (2.1)–(2.5) would be the usual MHD equations constituting a hyperbolic system. These extra terms are comparable to or dominant over the magnetohydrodynamic parts in some regions of the simulation domain. The semi-implicit method developed by Harned and Schnack (1986) frees us from the time-step restriction only in the integration of the magnetohydrodynamic parts. Thus we apply the time-step splitting method to Equation (2.5) and integrate (A) the hydrodynamic parts, (B) the heat source terms and (C) the conduction term successively and separately with different methods. The time-step splitting method was adopted by Dahlburg *et al.* (1987) to solve the energy equation in their simulation of the thermal instability.

First, we solve the governing equations without the heat source and heat conduction terms by means of the semi-implicit method, which is a predictor-corrector type scheme. The predictor

step is given by

$$\rho^* = \rho^n - \alpha\,\Delta t\,\nabla\cdot(\rho\mathbf{v})^n, \tag{A1}$$

$$\mathbf{v}^* = \mathbf{v}^n - \alpha\,\Delta t\left(\mathbf{v}\cdot\nabla\mathbf{v} + \frac{1}{\rho}\nabla p - \frac{1}{\rho}\mathbf{J}\times\mathbf{B} - \mathbf{g}\right)^n, \tag{A2}$$

$$\psi^* = \psi^n - \alpha\,\Delta t\,(\mathbf{v}\cdot\nabla\psi)^n, \tag{A3}$$

$$B_z{}^* = B_z{}^n + \alpha\,\Delta t\left(\frac{\partial}{\partial x}(v_z B_x - v_x B_z) + \frac{\partial}{\partial y}(v_z B_y - v_y B_z)\right)^n, \tag{A4}$$

$$T^* = T^n - \alpha\,\Delta t\,(\mathbf{v}\cdot\nabla T + (\gamma-1)T\nabla\cdot\mathbf{v})^n, \tag{A5}$$

where the superscript n represents the values at the n-th time-step. The constant α should be in the range $0.5 < \alpha < 1$ for numerical stability and $\alpha = 0.52$ is taken in our simulation.

In the corrector step the momentum equation is treated semi-implicitly:

$$\begin{aligned}
&v_x^{n+1} - (\Delta t)^2\left[(C_y{}^2 + C_z{}^2 + C_s{}^2)\frac{\partial^2 v_x^{n+1}}{\partial x^2} + C_y{}^2\frac{\partial^2 v_x^{n+1}}{\partial y^2}\right] \\
&\quad - \Delta t\nu\left(\frac{\partial^2 v_x^{n+1}}{\partial x^2} + \frac{\partial^2 v_x^{n+1}}{\partial y^2}\right) \\
&\quad = v_x^n - \Delta t\left[v_x\frac{\partial v_x}{\partial x} + v_y\frac{\partial v_x}{\partial y} + \frac{1}{\rho}\frac{\partial p}{\partial x} - \frac{1}{\rho}(J_y B_z - J_z B_y)\right]^* \\
&\qquad - (\Delta t)^2\left[(C_y{}^2 + C_z{}^2 + C_s{}^2)\frac{\partial^2 v_x^n}{\partial x^2} + C_y{}^2\frac{\partial^2 v_x^n}{\partial y^2}\right],
\end{aligned} \tag{A6a}$$

$$\begin{aligned}
&v_y^{n+1} - (\Delta t)^2\left[C_x{}^2\frac{\partial^2 v_y^{n+1}}{\partial x^2} + (C_z{}^2 + C_x{}^2 + C_s{}^2)\frac{\partial^2 v_y^{n+1}}{\partial y^2}\right] \\
&\quad - \Delta t\nu\left(\frac{\partial^2 v_y^{n+1}}{\partial x^2} + \frac{\partial^2 v_y^{n+1}}{\partial y^2}\right) \\
&\quad = v_y^n - \Delta t\left[v_x\frac{\partial v_y}{\partial x} + v_y\frac{\partial v_y}{\partial y} + \frac{1}{\rho}\frac{\partial p}{\partial y} - \frac{1}{\rho}(J_z B_x - J_x B_z) + g\right]^* \\
&\qquad - (\Delta t)^2\left[C_x{}^2\frac{\partial^2 v_y^n}{\partial x^2} + (C_z{}^2 + C_x{}^2 + C_s{}^2)\frac{\partial^2 v_y^n}{\partial y^2}\right],
\end{aligned} \tag{A6b}$$

$$\begin{aligned}
&v_z^{n+1} - (\Delta t)^2\left[C_x{}^2\frac{\partial^2 v_z^{n+1}}{\partial x^2} + C_y{}^2\frac{\partial^2 v_z^{n+1}}{\partial y^2}\right] - \Delta t\nu\left(\frac{\partial^2 v_z^{n+1}}{\partial x^2} + \frac{\partial^2 v_z^{n+1}}{\partial y^2}\right) \\
&= v_z^n - \Delta t\left[v_x\frac{\partial v_z}{\partial x} + v_y\frac{\partial v_z}{\partial y} - \frac{1}{\rho}(J_x B_y - J_y B_x)\right]^*
\end{aligned}$$

$$- (\Delta t)^2 \left[{C_x}^2 \frac{\partial^2 v_z^n}{\partial x^2} + {C_y}^2 \frac{\partial^2 v_z^n}{\partial y^2} \right], \tag{A16c}$$

where the constants C_x, C_y, C_z and C_s are, respectively, taken as the maximum values of $B_x/\rho^{\frac{1}{2}}$, $B_y/\rho^{\frac{1}{2}}$, $B_z/\rho^{\frac{1}{2}}$ and the sound speed, $(\gamma p/\rho)^{\frac{1}{2}}$, over the whole domain at each time-step. The new velocity is used to time-advance the other variables:

$$\rho^{n+1} = \rho^n - \Delta t \nabla \cdot (\rho^* \bar{\mathbf{v}}), \tag{A17}$$

$$\psi^{**} = \psi^n - \Delta t \bar{\mathbf{v}} \cdot \nabla \psi^*, \tag{A18a}$$

$$\psi^{n+1} = \psi^{**} + \Delta t \eta \left(\frac{\partial^2 \psi^{**}}{\partial x^2} + \frac{\partial^2 \psi^{**}}{\partial y^2} \right), \tag{A18b}$$

$${B_z}^{**} = {B_z}^n + \Delta t \left(\frac{\partial}{\partial x}(\bar{v}_z B_x^* - \bar{v}_x B_z^*) + \frac{\partial}{\partial y}(\bar{v}_z B_y^* - \bar{v}_y B_z^*) \right), \tag{A19a}$$

$${B_z}^{n+1} = {B_z}^{**} + \Delta t \eta \left(\frac{\partial^2 B_z^{**}}{\partial x^2} + \frac{\partial^2 B_z^{**}}{\partial y^2} \right), \tag{A19b}$$

$$T_M^{n+1} = T^n - \Delta t (\bar{\mathbf{v}} \cdot \nabla T^* + (\gamma - 1) T^* \nabla \cdot \bar{\mathbf{v}}), \tag{A10}$$

where $\bar{\mathbf{v}} = (\mathbf{v}^n + \mathbf{v}^{n+1})/2$ is the half-step velocity. In the above the resistive diffusion of ψ and B_z is treated explicitly owing to the small resistivity η. The variable T_M^{n+1} stands for the temperature updated by the adiabatic magnetohydrodynamics.

Secondly, we integrate the heating and radiative cooling terms:

$$T_{HC}^{n+1} = T_M^{n+1} + \Delta t \frac{(\gamma - 1)}{\rho^{n+1}} (H(\rho^{n+1}) - C(\rho^{n+1}, T_M^{n+1})) \tag{A11}$$

where T_{HC}^{n+1} represents the temperature updated by heating and cooling.

Finally, we solve the anisotropic thermal conduction equation:

$$\begin{aligned} \frac{\partial T}{\partial t} &= (\gamma - 1) \frac{T}{p} \nabla \cdot \kappa_{\parallel}(T) \nabla_{\parallel} T \\ &= (\gamma - 1) \frac{T}{p} \nabla \cdot \left(k_0 T^{5/2} \frac{\mathbf{B}}{B^2} \mathbf{B} \cdot \nabla T \right) \\ &= a_{xx} \frac{\partial^2 T}{\partial x^2} + a_{yy} \frac{\partial^2 T}{\partial y^2} + a_{xy} \frac{\partial^2 T}{\partial x \partial y} + b_x \frac{\partial T}{\partial x} + b_y \frac{\partial T}{\partial y} \end{aligned} \tag{A12}$$

where

$$a_{xx} = \frac{(\gamma - 1)}{\rho} \kappa_{\parallel} \frac{B_x^2}{B^2}, \tag{A13a}$$

$$a_{yy} = \frac{(\gamma-1)}{\rho}\kappa_{\parallel}\frac{B_y^2}{B^2}, \tag{A13b}$$

$$a_{xy} = \frac{(\gamma-1)}{\rho}2\kappa_{\parallel}\frac{B_x B_y}{B^2}, \tag{A13c}$$

$$b_x = \frac{(\gamma-1)}{\rho}\left[\frac{\partial}{\partial x}\left(\kappa_{\parallel}\frac{B_x^2}{B^2}\right) + \frac{\partial}{\partial y}\left(\kappa_{\parallel}\frac{B_x B_y}{B^2}\right)\right], \tag{A13d}$$

$$b_y = \frac{(\gamma-1)}{\rho}\left[\frac{\partial}{\partial x}\left(\kappa_{\parallel}\frac{B_x B_y}{B^2}\right) + \frac{\partial}{\partial y}\left(\kappa_{\parallel}\frac{B_y^2}{B^2}\right)\right]. \tag{A13e}$$

This equation is nonlinear since $\kappa_{\parallel}$ depends on T. As in Sparks *et al.* (1990) we linearize this equation by replacing T by T_{HC}^{n+1} in all the coefficients and solve it by the alternating direction implicit method (Douglas, 1962). By defining the following finite difference operators:

$$\sigma_x \equiv \Delta t\left(a_{xx}\frac{\partial^2}{\partial x^2} + b_x\frac{\partial}{\partial x}\right), \tag{A14a}$$

$$\sigma_y \equiv \Delta t\left(a_{yy}\frac{\partial^2}{\partial y^2} + b_y\frac{\partial}{\partial y}\right), \tag{A14b}$$

$$\sigma_{xy} \equiv \Delta t\left(a_{xy}\frac{\partial^2}{\partial x \partial y}\right), \tag{A14c}$$

we may write the algorithm as

$$(1-\theta\sigma_x)\tilde{T}^{n+1} = (1+(1-\theta)\sigma_x + \sigma_y + \sigma_{xy})T_{HC}^{n+1}, \tag{A15a}$$

$$(1-\theta\sigma_y)T^{n+1} = \tilde{T}^{n+1} - \theta\sigma_y T_{HC}^{n+1} \tag{A15b}$$

where T^{n+1} is the finally updated value of temperature. With $0.5 \leq \theta \leq 1$ the above scheme is unconditionally stable; the adopted value in our simulation is $\theta = 0.51$. Note that the mixed derivative term associated with σ_{xy} is treated explicitly and this treatment does not affect the numerical stability (Beam and Warming, 1980).

APPENDIX B

Helicity of a Magnetic Arcade in a 2-D Cartesian Geometry

In this appendix, we derive the helicity of a magnetic arcade in z-invariant geometry. The first part of the derivation is due to Lifschitz (1989).

The magnetic helicity is generally defined by

$$K_V = \int_V \mathbf{A} \cdot \mathbf{B}\, dV. \tag{B1}$$

In a 2-D potential field described by $\mathbf{A} = A_z\hat{\mathbf{z}}$ and $\mathbf{B} = \nabla \times \mathbf{A} = B_x\hat{\mathbf{x}} + B_y\hat{\mathbf{y}}$, the helicity is zero for any volume. Now we consider the volume surrounded by a flux surface and another surface where the normal magnetic field is constant in time. This volume, of course, changes its shape when plasma motion is present. The time-derivative of the helicity in this volume is

$$\begin{aligned}\frac{dK_V}{dt} &= \int_V \left(\frac{\partial \mathbf{A}}{\partial t} \cdot \mathbf{B} + \mathbf{A} \cdot \frac{\partial \mathbf{B}}{\partial t} + \nabla \cdot (\mathbf{A} \cdot \mathbf{B}\mathbf{v}) \right) dV \\ &= \int_V \left(-2\mathbf{E} \cdot \mathbf{B} + \nabla \cdot (\mathbf{A} \times \mathbf{E} + \mathbf{A} \cdot \mathbf{B}\mathbf{v}) \right) dV \\ &= \int_S \left(\mathbf{A} \times (\mathbf{E} + \mathbf{v} \times \mathbf{B}) + \mathbf{A} \cdot \mathbf{v}\mathbf{B} \right) \cdot \hat{\mathbf{n}}\, dS.\end{aligned} \tag{B2}$$

In ideal MHD, $\mathbf{E} + \mathbf{v} \times \mathbf{B} = 0$ and the above equation becomes

$$\frac{dK_V}{dt} = \int_S (\mathbf{A} \cdot \mathbf{v})(\mathbf{B} \cdot \hat{\mathbf{n}})\, dS. \tag{B3}$$

If $\mathbf{v} = 0$ or $\hat{\mathbf{n}} \cdot \mathbf{B} = 0$ on the boundary, the helicity is conserved. This is, however, not the case for 2-D magnetic arcades under footpoint shearing. In this case, we are concerned with a volume surrounded by a flux surface labeled by A_z, the photospheric boundary and two planes

perpendicular to the z axis separated by unit length. Then the helicity change comes from the photospheric boundary only and

$$\begin{aligned}\frac{dK(A_z)}{dt} &= \int_{x^-(A_z)}^{x^+(A_z)} A_z v_z(-B_y)\,dx \\ &= \int_{A_{zo}}^{A_z} A'_z\left(v_z^+ - v_z^-\right) dA'_z\,,\end{aligned} \tag{B4}$$

where the integration is performed along the x-axis. Here, A_{zo} is the value of A_z on the polarity inversion line, and the superscript '+' denotes the righthand side of the polarity inversion line and the superscript '−' the lefthand side. The helicity at a certain time is obtained by integrating Equation (B4) over time so that

$$K(A_z) = \int_{A_{zo}}^{A_z} A'_z \tilde{Z}(A'_z)\,dA'_z\,, \tag{B5}$$

where $\tilde{Z}(A'_z)$ is the z-distance between two conjugate footpoints labeled by A'_z. It can be seen in the above equation that the helicity is positive when the field line advances just as the righthand-screw does. When we use the notation defined in Chapter 3,

$$K(\psi) = 2\int_{\psi_o}^{\psi} \psi'\zeta(\psi')\,d\psi', \tag{B6}$$

where the factor 2 comes from our definition of $\zeta(\psi')$ as half the z-distance between conjugate footpoints. The differential helicity can be defined to be the helicity contained in the tube volume of unit poloidal flux:

$$H(\psi) \equiv -\frac{dK(\psi)}{d\psi} = -2\psi\zeta\,, \tag{B7}$$

in which the minus sign is included to conform to the righthand-screw rule.

REFERENCES

Aly, J. J., On the properties of force-free magnetic fields in infinite regions of space, *Astrophys. J., 283*, 349, 1984.

Aly, J. J., Quasi-static evolution of sheared force-free fields and the solar flare problem, *Astron. Astrophys., 143*, 19, 1985.

Aly, J. J., Quasi-static evolution of a force-free magnetic field, *Comp. Phys. Comm., 59*, 13, 1990.

Aly, J. J., How much energy can be stored in a three-dimensional force-free magnetic field?, *Astrophys. J., 375*, L61, 1991.

Aly, J. J., Eruptive processes in the solar corona, in *Cosmical Magnetism, Contributed Papers of the NATO Advanced Research Workshop*, edited by D. Lynden-Bell, pp. 7–15, Institute of Astronomy, Cambridge, 1994a.

Aly, J. J., Asymptotic formation of a current sheet in an indefinitely sheared force-free field: an analytical example, *Astron. Astrophys., 288*, 1012, 1994b.

Aly, J. J., Nonequilibrium in sheared axisymmetric force-free magnetic fields, *Astrophys. J., 439*, L63, 1995.

An, C.-H., Formation of prominences by condensation modes in magnetized cylindrical plasma, *Astrophys. J., 298*, 409, 1985.

An, C.-H., Condensation modes in sheared magnetic fields, *Astrophys. J., 304*, 532, 1986.

An, C.-H., S. T. Suess, E. Tandberg-Hanssen, and R. S. Steinolfson, On the formation of coronal cavities, *Solar Phys., 102*, 165, 1985.

Antiochos, S. K., R. B. Dahlburg, and J. A. Klimchuk, The magnetic field of solar prominences, *Astrophys. J., 420*, L41, 1994.

Anzer, U., Structure and equilibrium of prominences, in *Dynamics and Structure of Quiescent Solar Prominences*, edited by E. R. Priest, pp. 143–166, Kluwer Academic Publishers, Dordrecht, Holland, 1989.

Athay, R. G., C. W. Querfeld, R. N. Smartt, E. Landi degl'Innocenti, and V. Bommier, Vector magnetic fields in prominences, III: HeI D_3 Stokes profile analysis for quiescent and eruptive prominences, *Solar Phys., 89*, 3, 1983.

Athay, R. G., H. Jones, and H. Zirin, Magnetic shear. I. Hale region 16918, *Astrophys. J., 288*, 363, 1985.

Babcock, H. W., and H. D. Babcock, The Sun's magnetic field, 1952–1954, *Astrophys. J., 121*, 349, 1955.

Barnes, C. W., and P. A. Sturrock, Force-free magnetic field structures and their role in solar activity, *Astrophys. J., 174*, 659, 1972.

Beam, R. M., and R. F. Warming, Alternating direction implicit methods for parabolic equations with a mixed derivative, *SIAM. J. Sci. Stat. Comput., 1*, 131, 1980.

Bessey, R. J., and D. H. Liebenberg, Coronal temperature measurements near a helmet structure base at the 1973 solar eclipse, *Solar Phys., 94*, 239, 1984.

Billings, D. E., and C. Kober, Distribution of prominence heights, *Astron. J., 62*, 242, 1957.

Biskamp, D., Magnetic reconnection via current sheets, *Phys. Fluids, 29*, 1520, 1986.

Biskamp, D., and H. Welter, Coalescence of magnetic islands, *Phys. Rev. Lett., 44*, 1069, 1980.

Biskamp, D., and H. Welter, Magnetic arcade evolution and instability, *Solar Phys., 120*, 49, 1989.

Browning, P. K., Magnetohydrodynamics in solar coronal and laboratory plasmas: a comparative study, *Physics Reports, 169*, 329, 1988.

Bruzek, A., *Landolt-Börnstein: Zahlenwerte und Funktionen aus Naturwissenschaften und Technik*, edited by K. Schaifers and H. H. Voigt, Neue Serie Gruppe VI Band 2 Teilband a, p. 120, Springer-Verlag, Berlin, 1981.

Chiuderi, C., and G. Van Hoven, The dynamics of filament formation: the thermal instability in a sheared magnetic field, *Astrophys. J., 232*, L69, 1979.

Chodura, R., and A. Schlüter, A 3D code for MHD equilibrium and stability, *J. Comput. Phys., 41*, 68, 1981.

Choe, G. S., and L. C. Lee, Formation of solar prominences by photospheric shearing motions, *Solar Phys., 138*, 291, 1992.

Choe, G. S., and L. C. Lee, Formation of Solar Prominences with Normal and Inverse Polarities, in *The Magnetic and Velocity Fields of Solar Active Regions, Proceedings of the IAU Colloquium 141, Beijing, China*, edited by H. Zirin, G. Ai and H. Wang, pp. 138-142, Astronomical Society of the Pacific, San Fransisco, 1993.

Cox, D. P., and W. H. Tucker, Ionization equilibrium and radiative cooling of a low density plasma, *Astrophys. J., 157*, 1157, 1969.

Dahlburg, R. B., C. R. DeVore, J. M. Picone, J. T. Mariska, and J. T. Karpen, Nonlinear evolution of radiation-driven thermally unstable fluids, *Astrophys. J., 315*, 385, 1987.

Démoulin, P., Solar prominences, in *Advances in Solar System Magnetohydrodynamics*, edited by E. R. Priest and A. W. Hood, pp. 281–305, Cambridge University Press, Cambridge, 1991.

Douglas, J., Jr., Alternating direction methods for three space variables, *Numer. Math., 4*, 41, 1962.

Drake, J. F., Y. Mok, and G. Van Hoven, Formation, levitation, and stability of prominences in the magnetized solar atmosphere, *Astrophys. J., 413*, 416, 1993.

Dryer, M., Coronal transient phenomena, *Space Sci. Rev., 33*, 233, 1982.

Engvold, O., The fine structure of prominences. I.: Observations – H_α filtergrams, *Solar Phys., 49*, 283, 1976.

Engvold, O., The fine structure of prominences. IV.: Spectral observations, *Solar Phys., 56*, 87, 1978.

Engvold, O., Prominence environment, in *Dynamics and Structure of Quiescent Solar Prominences*, edited by E. R. Priest, pp. 47–76, Kluwer Academic Publishers, Dordrecht, Holland, 1989.

Field, G. B., Thermal instability, *Astrophys. J., 142*, 531, 1965.

Finn, J. M., and J. Chen, Equilibrium of solar coronal arcades, *Astrophys. J., 349*, 345, 1990.

Forbes, T. G., Numerical simulation of a catastrophe model for coronal mass ejections, *J. Geophys. Res., 95*, 11919, 1990a.

Forbes, T. G., Basic properties and models of solar prominences, in *Physics of Magnetic Flux Ropes*, edited by C. T. Russell, E. R. Priest and L. C. Lee, pp. 295–306, American Geophysical Union, Washington, DC, 1990b.

Forbes, T. G., Magnetic reconnection in solar flares, *Geophys. Astrophys. Fluid Dynamics, 62*, 15, 1991.

Forbes, T. G., Field Opening and Reconnection, in *Eruptive Solar Flares, Proceedings of the No. 133 Colloquium of the IAU, Iguazú, Argentina*, edited by Z. Švestka, B. V. Jackson and M. E. Machado, *Lecture Notes in Physics, 399*, pp. 79–88, Springer Verlag, Berlin, 1992.

Forbes, T. G., and E. R. Priest, A comparison of analytical and numerical models for steadily driven magnetic reconnection, *Rev. Geophys., 25*, 1583, 1987.

Forbes, T. G., and Isenberg, P. A., A catastrophe mechanism for coronal mass ejections, *Astrophys. J., 373*, 294, 1991.

Forbes, T. G., and J. M. Malherbe, A numerical simulation of magnetic reconnection and radiative cooling in line-tied current sheets, *Solar Phys., 135*, 361, 1991.

Furth, H. P., J. Killeen, and M. N. Rosenbluth, Finite resistivity instabilities of a sheet pinch, *Phys. Fluids, 6*, 459, 1963.

Giovanelli, R. G., Magnetic and electric phenomena in the Sun's atmosphere associated with sunspots, *Mon. Not. R. Astron. Soc., 107*, 338, 1947.

Gold, T., and F. Hoyle, On the origin of solar flares, *Mon. Not. R. Astron. Soc., 120*, 89, 1960.

Hagyard, M. J., V. Gaizauskas, G. A. Chapman, A. C. de Loach, G. A. Gary, H. P. Jones, J. T. Karpen, M.-J. Martres, J. G. Porter, B. Schmieder, J. B. Smith, Jr., and J. Toomre, Preflare magnetic and velocity fields, in *Energetic Phenomena on the Sun*, edited by M. Kundu and B. Woodgate, NASA CP-2439, pp. 1-16–48, 1986.

Harned, D. S., and D. D. Schnack, Semi-implicit method for long time scale magnetohydrodynamic computations in three dimensions, *J. Comput. Phys., 65*, 57, 1986.

Heyvaerts, J., E. R. Priest, and D. M. Rust, An emerging flux model for the solar flare phenomenon, *Astrophys. J., 216*, 123, 1977.

Hildner, E., The formation of solar quiescent prominences by condensations, *Solar Phys., 35*, 123, 1974.

Hirayama, T., Modern observations of solar prominences, *Solar Phys.,100*, 415, 1985.

Hood, A. W., MHD of solar flares, in *Advances in Solar System Magnetohydrodynamics*, edited by E. R. Priest and A. W. Hood, pp. 307–326, Cambridge University Press, Cambridge, 1991.

Hu, W.-R., The dynamical process of a coronal transient associated with an eruptive prominence. I. Basic mechanism, *Astrophys. Space Sci.*, *92*, 373, 1983a.

Hu, W.-R., The dynamical process of a coronal transient associated with an eruptive prominence. II. Analytic solutions in finite regions, *Astrophys. Space Sci.*, *92*, 395, 1983b.

Hundhausen, A. J., The origin and propagation of coronal mass ejections, in *Proceedings of the Sixth International Solar Wind Conference*, edited by V. J. Pizzo, T. E. Holzer and D. G. Sime, pp. 181–214, NCAR Technical Note 306, Boulder, 1988.

Hundhausen, A. J., Coronal mass ejections: a summary of SMM observations, in *The Many Faces of the Sun*, edited by K. Strong, J. Saba and B. Haisch, in press, 1995.

Hyder, C. L., A phenomenological model for disparitions brusques followed by flare-like chromospheric brightenings I: The model, its consequences, and observations in quiet solar regions, *Solar Phys.*, *2*, 49, 1967.

Inhester, B., J. Birn, and M. Hesse, The evolution of line-tied coronal arcades including a converging footpoint motion, *Solar Phys.*, *138*, 257, 1992.

Kan. J. R., S.-I. Akasofu, and L. C. Lee, A dynamo theory of solar flares, *Solar Phys.*, *84*, 153, 1983.

Karpen, J. T., S. K. Antiochos, and C. R. DeVore, On the formation of current sheets in the solar corona, *Astrophys. J.*, *356*, L67, 1990.

Kim, I. S., S. Koutchmy, G. Stellmacher, and A. I. Stepanov, in *Role of Fine-Scale Magnetic Fields on the Structure of the Solar Atmosphere*, edited by E. Schröter, M. Vazquez and A. Wyller, p. 289, Cambridge University Press, Cambridge, 1988.

Kippenhahn, R., and A. Schlüter, Eine Theorie der solaren Filamente, *Z. Astrophys.*, *43*, 36, 1957.

Klimchuk, J. A., Shear-induced inflation of coronal magnetic fields, *Astrophys. J.*, *354*, 745, 1990.

Klimchuk, J. A., and P. A. Sturrock, Force-free magnetic fields: Is there a "loss of equilibrium"?, *Astrophys. J., 345*, 1034, 1989.

Klimchuk, J. A., P. A. Sturrock, and W. H. Yang, Coronal magnetic fields produced by photospheric shear, *Astrophys. J., 335*, 456, 1988.

Kopp, R. A., and G. W. Pneuman, Magnetic reconnection in the corona and the loop prominence phenomenon, *Solar Phys., 50*, 85, 1976.

Kuperus, M., and M. A. Raadu, The support of prominences formed in neutral sheets, *Astron. Astrophys., 31*, 185, 1974.

Kusano, K., Y. Suzuki, and K. Nishikawa, A solar flare triggering mechanism based on the Woltjer-Taylor minimum energy principle, *Astrophys. J., 441*, 942, 1995.

Lee, L. C., a presentation given in the Workshop on Solar Flares and Magnetospheric Substorms, Hawaii, 1990 (unpublished).

Lee, L. C., and Z. F. Fu, Multiple X line reconnection, 1. A criterion for the transition from a single X line to a multiple X line reconnection, *J. Geophys. Res., 91*, 6807, 1986.

Lee, L. C., L. Zhang, G. S. Choe, and H. J. Cai, Formation of a very thin current sheet in the near-earth magnetotail and explosive growth phase of substorms, *Geophys. Res. Lett., 22*, 1137, 1995.

Leroy, J. L., Observation of prominence magnetic fields, in *Dynamics and Structure of Quiescent Solar Prominences*, edited by E. R. Priest, pp. 77–114, Kluwer Academic Publishers, Dordrecht, Holland, 1989.

Leroy, J. L., V. Bommier, and S. Sahal-Bréchot, The magnetic field in prominences of the polar crown, *Solar phys., 83*, 135, 1983.

Leroy, J. L., V. Bommier, and S. Sahal-Bréchot, New data on the magnetic structure of quiescent prominences, *Astron. Astrophys., 131*, 33, 1984.

Lifschitz, A. E., *Magnetohydrodynamics and Spectral Theory*, Kluwer Academic Publishers, Dordrecht, Holland, 1989.

Ligget, M., and H. Zirin, Rotation in prominences, *Solar Phys., 91*, 259, 1984

Lin, Y., and L. C. Lee, Structure of reconnection layers in the magnetosphere, *Space Sci. Rev., 65* , 59, 1994.

Linker, J. A., and Z. Mikić, Disruption of a helmet streamer by photospheric shear, *Astrophys. J., 438*, L45, 1995.

Livi, S. B., S. Martin, H. Wang, and G. Ai, The association of flares to cancelling magnetic features on the sun, *Solar Phys., 121*, 197, 1989.

Low, B. C., Evolving force-free magnetic fields, IV. A variational formulation of the problem, *Astrophys. J., 224*, 668, 1978.

Low, B. C., The field and plasma configuration of a filament overlying a solar bipolar region, *Astrophys. J., 246*, 538, 1981.

Low, B. C., Blowup of force-free magnetic fields in the infinite region of space, *Astrophys. J., 307*, 205, 1986.

Low, B. C., On the spontaneous formation of electric current sheets above a flexible solar photosphere, *Astrophys. J., 381*, 295, 1991.

Low, B. C., Formation of electric-current sheets in the magnetostatic atmosphere, *Astron. Astrophys., 253*, 311, 1992.

Low, B. C., and R. Wolfson, Spontaneous formation of electric current sheets and the origin of solar flares, *Astrophys. J., 324*, 574, 1988.

Lynden-Bell, D., and C. Boily, Self-similar solutions up to flashpoint in highly wound magnetostatics, *Mon. Not. R. Aston. Soc., 267*, 146, 1994.

McWhirter, R. W. P., P. C. Thonemann, and R. Wilson, The heating of the solar corona. II. A model based on energy balance, *Astron. Astrophys., 40*, 63, 1975.

Malherbe, J. M., B. Schmieder, E. Ribes, and P. Mein, Dynamics of solar filaments, II. Mass motions in an active region filament from H_α center to limb observations, *Astron. Astrophys., 119*, 197, 1983.

Martin, S. F., The evolution of prominences and their relationship to active centers, *Solar Phys., 31*, 3, 1973.

Martin, S. F., Conditions for the formation of prominences as inferred from optical observations, in *Dynamics of Quiescent Prominences, Proceedings of the No. 117 Colloquium of the IAU, Hvar, Yugoslavia*, edited by V. Ruždjak and E. Tandberg-Hanssen, *Lecture Notes in Physics, 363*, pp. 1–48, Springer Verlag, Berlin, 1990.

Mikić, Z., and J. A. Linker, Disruption of coronal magnetic arcades, *Astrophys. J., 430*, 898, 1994.

Mikić, Z., D. C. Barnes, and D. D. Schnack, Dynamical evolution of a solar coronal magnetic field arcade, *Astrophys. J., 328*, 830, 1988.

Parker, E. N., The solar-flare phenomenon and the theory of reconnection and annihilation of magnetic fields, *Astrophys. J. Suppl. Ser., 8*, 177, 1963.

Parker, E. N., *Cosmical Magnetic Fields*, Clarendon Press, Oxford, 1979.

Peres, G., R. Rosner, S. Serio, and G. S. Vaiana, Coronal closed structures. IV. Hydrodynamical stability and response to heating perturbations, *Astrophys. J., 252*, 791, 1982.

Petschek, H. E., Magnetic field annihilation, in *AAS-NASA Symposium on the Physics of Solar Flares*, edited by W. N. Hess, NASA SP-50, pp. 425–439, 1964.

Priest, E. R., *Solar Flare Magnetohydrodynamics*, Gordon and Breach, London, 1981.

Priest, E. R., *Solar Magnetohydrodynamics*, D. Reidel, Dordrecht, Holland, 1982.

Priest, E. R., *Dynamics and Structures of Quiescent Solar Prominences*, Kluwer Academic Publishers, Dordrecht, Holland, 1989.

Priest, E. R., and T. G. Forbes, Magnetic flipping: reconnection in three dimensions without null points, *J. Geophys. Res., 97*, 1521, 1992a.

Priest, E. R., and T. G. Forbes, Does fast magnetic reconnection exist?, *J. Geophys. Res., 97*, 16757, 1992b.

Raymond, J. C., and B. W. Smith, Soft X-ray spectrum of a hot plasma, *Astrophys. J. Suppl., 35*, 419, 1977.

Rompolt, B., and T. Bogdan, On the formation of active region prominences (H_α filaments), in *Coronal and Prominence Plasmas*, edited by A. Poland, pp. 81–87, NASA Conference Publication 2442, Washington, DC, 1986.

Rosner, R., W. H. Tucker, and G. S. Vaiana, Dynamics of the quiescent solar corona, *Astrophys. J., 220*, 643, 1978.

Roumeliotis, G., P. A. Sturrock, and S. K. Antiochos, A numerical study of the sudden eruption of sheared magnetic fields, *Astrophys. J., 423*, 847, 1994.

Rust, D. M., Flares and changing magnetic fields, *Solar Phys., 25*, 141, 1972.

Saito, K., and E. Tandberg-Hanssen, The arch systems, cavities and prominences in the helmet streamer observed at the solar eclipse, November 12, 1966, *Solar Phys., 31*, 105, 1973.

Schmieder, B., Overall properties and steady flows, in *Dynamics and Structure of Quiescent Solar Prominences*, edited by E. R. Priest, pp. 15–46, Kluwer Academic Publishers, Dordrecht, Holland, 1989.

Scholer, M., Undriven magnetic reconnection in an isolated current sheet, *J. Geophys. Res., 94*, 8805, 1989.

Serio, S., G. S. Vaiana, G. Godoli, S. Motta, V. Pirronello, and R. A. Zappala, Configuration and gradual dynamics of prominence-related X-ray coronal cavities, *Solar Phys., 59*, 65, 1978.

Shibata, K, Y. Ishido, L. W. Acton, K. T. Strong, T. Hirayama, Y. Uchida, A. H. McAllister, R. Matsumoto, S. Tsuneta, T. Shimizu, H. Hara, T. Sakurai, K. Ichimoto, Y. Nishino, and Y. Ogawara, Observations of X-ray jets with the Yohkoh Soft X-ray Telescope, *Publ. Astron. Soc. Japan, 44*, L173, 1992.

Sparks, L., G. Van Hoven, and D. D. Schnack, The nonlinear evolution of magnetized solar filaments, *Astrophys. J., 353*, 297, 1990.

Spitzer, L., *Physics of Fully Ionized Gases*, Interscience, New York, 1962.

Steinolfson, R. S., Coronal evolution due to shear motion, *Astrophys. J., 382*, 677, 1991.

Steinolfson, R. S., and A. J. Hundhausen, MHD intermediate shocks in coronal mass ejections, *J. Geophys. Res., 95*, 6839, 1990a.

Steinolfson, R. S., and A. J. Hundhausen, Concave-outward slow shocks in coronal mass mass ejections, *J. Geophys. Res., 95*, 15251, 1990b.

Steinolfson, R. S., and A. J. Hundhausen, Coronal mass ejection shock fronts containing the two types of intermediate shocks, *J. Geophys. Res., 95*, 20693, 1990c.

Steinolfson, R. S., and G. Van Hoven, Radiative tearing: magnetic reconnection on a fast thermal-instability time scale, *Astrophys. J., 276*, 391, 1984.

Sturrock, P. A., Maximum energy of semi-infinite magnetic field configurations, *Astrophys. J., 380*, 655, 1991.

Sweet, P. A., The neutral point theory of solar flares, in *Electromagnetic Phenomena in Cosmic Physics*, edited by B. Lehnert, p. 135, 1958.

Tandberg-Hanssen, E., Solar prominences, D. Reidel, Dordrecht, Holland, 1974.

Tang, F., Quiescent prominences — Where are they formed?, *Solar Phys., 107*, 233, 1987.

Taylor, J. B., Relaxation of toroidal plasma and generation of reverse magnetic fields, *Phys. Rev. Lett., 33*, 1139, 1974.

Tucker, W. H., and M. Koren, Radiation from a high temperature, low-density plasma: the X-ray spectrum of the solar corona, *Astrophys. J., 168*, 283, 1971.

Uchida, Y., Problems for arcade and loop flare models revealed by Yohkoh, to be published in *Magnetodynamic Phenomena in the Solar Atmosphere, Proceedings of the No. 153 Colloquium of the IAU, Makuhari, Japan*, edited by Y. Uchida, T. Kosugi and H. S. Hudson, Kluwer Academic Publishers, Dordrecht, Holland, 1995.

van Ballegooijen, A. A., and P. C. H. Martens, Formation and eruption of solar prominences, *Astrophys. J., 343*, 971, 1989.

Van Hoven, G., and Y. Mok, The thermal instability in a sheared magnetic field: filament condensation with anisotropic heat conduction, *Astrophys. J., 282*, 267, 1984.

Van Hoven, G., L. Sparks, and T. Tachi, Ideal condensations due to perpendicular thermal conduction in a sheared magnetic field, *Astrophys. J., 300*, 249, 1986.

Van Tend, W., and M. Kuperus, The development of coronal electric current systems in active regions and their relation to filaments and flares, *Solar Phys., 59*, 115, 1978.

Vasyliunas, V. M., Theoretical models of magnetic field line merging, 1., *Rev. Geophys., 13*, 303, 1975.

Vekstein, G. E., and E. R. Priest, Magnetohydrodynamic equilibria and cusp formation at an X-type neutral line by footpoint shearing, *Astrophys. J., 384*, 333, 1992.

Waldmeier, M., The structure of monochromatic corona in the surroundings of prominences, *Solar Phys., 15*, 167, 1970.

Wang, H., M. W. Ewell, Jr., H. Zirin, and G. Ai, Vector magnetic field changes associated with X-class flares, *Astrophys. J., 424*, 436, 1994.

Wolfson, R., and B. C. Low, Energy buildup in sheared force-free magnetic fields, *Astrophys. J., 391*, 353, 1992.

Woltjer, L., A theorem on force-free magnetic fields, *Proc. Nat. Acad. Sci., 44*, 489, 1958.

Wu, S. T., J. J. Bao, C. H. An, and E. Tandberg-Hanssen, The role of condensation and heat conduction in the formation of prominences: an MHD simulation, *Solar Phys., 125*, 277, 1990.

Yan, M., L. C. Lee, and E. R. Priest, Fast magnetic reconnection with small shock angles, *J. Geophys. Res., 97*, 8277, 1992.

Yan, M., L. C. Lee, and E. R. Priest, Magnetic reconnection with large separatrix angles, *J. Geophys. Res., 98*, 7593, 1993.

Yang, W. H., P. A. Sturrock, and S. K. Antiochos, Force-free magnetic fields: the magneto-frictional method, *Astrophys. J., 309*, 383, 1986.

Yokoyama, T., Magnetohydrodynamic simulation of solar coronal X-ray jets based on magnetic reconnection model, Ph.D. Thesis, National Astronomical Observatory, Mitaka, Japan, 1995.

Yokoyama, T., and K. Shibata, What is the condition for fast magnetic reconnection?, *Astrophys. J., 436*, L197, 1994.

Zirin, H., *Astrophysics of the Sun*, Cambridge University Press, Cambridge, 1988.

Zwingmann, W., Theoretical study of onset conditions for solar eruptive processes, *Solar phys., 111*, 309, 1987.